



FEDERAL UNIVERSITY OF ESPÍRITO SANTO
TECHNOLOGICAL CENTER
GRADUATE PROGRAM IN ELECTRICAL ENGINEERING

LUÍS CICERO BEZERRA DA SILVA

DOCTORAL THESIS

Signal processing and computational modeling for
optical fiber sensor devices

Vitória, 2021

FEDERAL UNIVERSITY OF ESPÍRITO SANTO

Doctoral Thesis

Signal processing and computational modeling for
optical fiber sensor devices

Author:

Luís Cicero Bezerra da Silva

Advisors:

Maria José Pontes

Marcelo Eduardo Vieira Segatto

Thesis submitted for the degree of Doctor in Electrical Engineering

Electrical Engineering Department

November, 2021

Ficha catalográfica disponibilizada pelo Sistema Integrado de
Bibliotecas - SIBI/UFES e elaborada pelo autor

S586s Silva, Luís Cicero Bezerra da, 1992-
Signal processing and computational modeling for optical
fiber sensor devices / Luís Cicero Bezerra da Silva. - 2021.
118 f. : il.

Orientadora: Maria José Pontes.
Coorientador: Marcelo Eduardo Vieira Segatto.
Tese (Doutorado em Engenharia Elétrica) - Universidade
Federal do Espírito Santo, Centro Tecnológico.

1. Óptica. 2. Processamento de sinais. 3. Fibras ópticas. 4.
Detectores ópticos. 5. Sensoriamento remoto. I. Pontes, Maria
José. II. Segatto, Marcelo Eduardo Vieira. III. Universidade
Federal do Espírito Santo. Centro Tecnológico. IV. Título.

CDU: 621.3

LUÍS CICERO BEZERRA DA SILVA

Signal processing and computational modeling for optical fiber sensor devices

Thesis submitted to the Graduate Program in Electrical Engineering of the Federal University of Espírito Santo, as partial requirement for the degree of Doctor in Electrical Engineering.

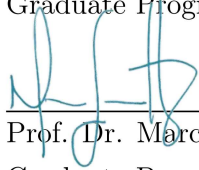
Approved on November 26, 2021

Examiners:



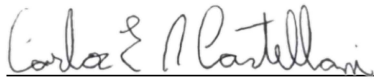
Prof. Dr.^a Maria José Pontes - Advisor.

Graduate Program in Electrical Engineering, Federal University of Espírito Santo, Brazil



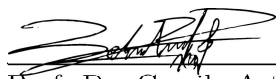
Prof. Dr. Marcelo Eduardo Vieira Segatto - Co-Advisor

Graduate Program in Electrical Engineering, Federal University of Espírito Santo, Brazil



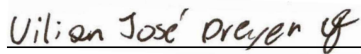
Prof. Dr. Carlos Eduardo Schmidt Castellani

Graduate Program in Electrical Engineering, Federal University of Espírito Santo, Brazil



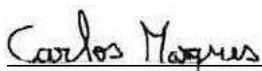
Prof. Dr. Camilo Arturo Rodríguez Díaz

Graduate Program in Electrical Engineering, Federal University of Espírito Santo, Brazil



Prof. Dr. Uilian José Dreyer

Graduate Program in Energy Systems, Federal University of Technology of Paraná, Brazil



Dr. Carlos Alberto Ferreira Marques

Department of Physics & I3N and Institute of Telecommunications, University of Aveiro,
Portugal

Statement of Originality

All the work reported in this thesis is the result of my own work realized during my Ph.D. unless stated otherwise in which case the appropriate references are made.

“I believe that one form of happiness is the reading.”

Jorge Luis Borges
(Translated from Portuguese)

Abstract

In the last four decades, special interest has been taken in exploring the characteristics of the optical environment for sensing, giving rise to what would now be one of the largest applications of well-known optical fibers, generally employed to transmit data at high rates. Sensing temperature, pressure, liquid level, deformation among other physical parameters employing optical fibers has become not only a growing branch of research but also a business competing with well-established electrical sensors in the industry. Optical fiber sensors have all the inherent characteristics of a fiber optic cable, such as electromagnetic immunity, small size and weight, multiplexing, and so on. These exclusive features have made fiber sensors so versatile as to become a transformative technology by enabling several industrial processes to be carried out with a higher degree of security. Nowadays, there are several types of optical sensors, these include fiber Bragg grating sensors, Fabry-Perot sensors, interferometric sensors, distributed sensors, polarimetric sensors, polymer fiber sensors, and several others. This immense diversity allows these sensors to be applied in biomedicine, military defense systems, structural health monitoring of bridges, oil wells downhole, pipelines, power transmission lines, and so on. However, to operate properly, these sensors require adequate processing so that the information measured by them is extracted in the best possible way. In this perspective, this thesis describes a set of signal processing techniques developed for these sensors. The contributions described here cover two classes of optical sensors: Raman distributed temperature sensors and interferometric sensors. For the former one, a method to detect and measure small temperature events on a scale of a few centimeters, as well as a theoretical analysis of the receiver these sensors to improve its sensitivity through hardware modifications are presented. Furthermore, for the latter, a linearization technique is developed to improve its linearity and operation range.

Keywords: Optics, signal processing, computational modeling, optical fiber sensors, Raman distributed temperature sensors, spontaneous Raman scattering, interferometric fiber sensors.

Resumo

Nas últimas quatro décadas, especial interesse tem sido dado à exploração das características do ambiente óptico para sensoriamento, dando origem ao que hoje seria uma das maiores aplicações das bem conhecidas fibras ópticas, geralmente empregadas para transmitir dados à altas taxas. O sensoriamento de temperatura, pressão, nível de líquido, deformação, entre outros parâmetros físicos que empregam fibras ópticas, tornou-se não apenas um ramo crescente de pesquisa, mas também uma atividade comercial concorrente com sensores elétricos bem estabelecidos na indústria. Os sensores de fibra óptica têm todas as características inerentes de um cabo de fibra óptica, como imunidade eletromagnética, tamanho e peso reduzidos, multiplexação, etc. Estas características exclusivas fizeram os sensores em fibra tão versáteis que se tornaram uma tecnologia transformadora possibilitando que diversos processos industriais sejam executados com maior grau de segurança. Hoje em dia, existem vários tipos de sensores ópticos, estes incluem sensores de rede de Bragg em fibra, Fabry-Perot, interferométricos, distribuídos, polarimétricos, de fibra de polímero, e vários outros. Essa imensa diversidade permite que esses sensores sejam aplicados em biomedicina, sistemas de defesa militar, monitoramento da integridade estrutural de pontes, poços de petróleo, oleodutos, linhas de transmissão de energia e assim por diante. Entretanto, para operar adequadamente, tais sensores requerem processamento adequado para que as informações por eles medidas sejam extraídas da melhor maneira possível. Nessa perspectiva, esta tese descreve um conjunto de técnicas de processamento de sinais desenvolvidas para esses sensores. As contribuições descritas aqui cobrem duas classes de sensores ópticos: sensores distribuídos de temperatura baseados em Raman e sensores interferométricos. Para o primeiro, é apresentado um método para detectar e medir pequenos eventos de temperatura em uma escala de poucos centímetros, bem como uma análise teórica do receptor desses sensores para melhorar sua sensibilidade por meio de modificações a nível de hardware. Além disso, para este último, uma técnica de linearização é desenvolvida para melhorar sua linearidade e faixa de operação.

Palavras-chave: Óptica, processamento de sinais, modelagem computacional, sensores em fibras ópticas, sensores distribuídos de temperatura baseados em Raman, espalhamento Raman espontâneo, sensores interferométricos em fibra.

Acknowledgements

First of all, I need to recognize that this work is not only the result of my efforts but also of all the people around me that directly and indirectly contributed to the realization of this doctoral thesis. I would like to express my immeasurable gratitude to my supervisors Professor Maria José Pontes and Professor Marcelo Eduardo Vieira Segatto for their orientation, patience, friendship, and encouragement throughout the development of this work. I am very honored for the opportunity to work with them and for all the valuable lessons I have received.

On this journey, I met Professor Jorge Leonid Aching Samatelo, who introduced me to the signal processing area and who contributed expressively to this work. My sincere thanks to Professor Jorge Samatelo. I cannot forget to mention the immense support provided by Professor Carlos Eduardo Schmidt Castellani. It was many hours discussing physical issues, mathematical formulations, and examining computational simulations that words are insufficient to thank for such generosity. I would like to express my gratitude to Professor Carlos Castellani, not only for all the scientific contributions to this thesis but also for being a great friend giving me the best advice at the right moments.

Part of this research was carried out in the Laboratory of Engineering of Optoelectronic Systems (LabESO) of the Federal University of Technology of Paraná (UTFPR), under the supervision of Professor Jean Carlos Cardozo da Silva. The entire period at LabESO was one of constant learning and interaction with the professionals who work there. That made it possible to make many friendships. I am thankful to Professor Jean Silva for the supervision at this stage of my research and to the entire LabESO team of professors and students who provided impeccable support for an excellent job to be done.

I would also like to thank Carlos Alberto Ferreira Marques for the opportunity to expand my field of study, developing works parallel to the theme of this thesis. This opportunity made it possible to make new research partnerships and brought me a lot of learning during this doctoral journey, that strengthened my understanding of signal/data processing applied to the monitoring of facilities through sensing. Equally important, I thank Mariana Arpini Vieira and Professor Jair Carlos Checon de Freitas from the Laboratory of Carbon and Ceramic Materials of the Physics department at the Federal University of Espírito Santo (UFES), and Yuli Andrea Álvarez Pizarro who contributed to the parallel research with graphite oxide as a saturable absorber for the generation of pulsed fiber lasers. Furthermore, I also

wish to thank my parents and family for all the support and understanding during my Ph.D. I extend my thanks to the friends, colleagues, professors and academic staff members of the Laboratory of Telecommunications (LabTel) of the Federal University of Espírito Santo for the fellowship, and the Fundação de Amparo à Pesquisa e Inovação do Espírito Santo - FAPES (projects 66/2017, 031/2021) for the financial support granted through the scholarship.

Contents

Abstract	iii
Acknowledgements	v
List of figures	xii
List of acronyms	xiii
List of symbols	xiv
1 Introduction	1
1.1 Overview	1
1.2 Optical fiber waveguides	2
1.3 Optical fiber sensors	4
1.4 Motivation	8
1.5 Organization of the thesis	8
1.6 Publications	9
1.6.1 Journal articles	9
1.6.2 Conference papers	11
1.7 Main achievements	12
2 Detection of small distributed temperature events	14
2.1 Overview	14
2.2 Theoretical background	14
2.2.1 Spontaneous scattering in optical fibers	14
2.2.2 Spontaneous Raman scattering	17
2.2.3 Raman-based distributed temperature sensors	18
2.3 Developed model	24
2.3.1 1D to 2D data reconstruction	24
2.3.2 Thresholding-based image segmentation	25
2.3.3 Measured temperature correction	26
2.4 Temperature data acquisition	29

2.5	Results and discussion	30
2.5.1	Scenario one	30
2.5.2	Scenario two	32
3	Analytical investigation for RDTS receivers	36
3.1	Overview	36
3.2	Introduction	36
3.3	Theoretical background	38
3.3.1	Basic concepts of optical receivers	38
3.3.2	Avalanche photodiodes	40
3.4	Analytical model and simulation analysis	43
3.4.1	Receiver structure	43
3.4.2	Characterization of the signal	44
3.4.3	Minimum allowed signal to noise ratio level	45
3.4.4	Amplification gain	46
3.4.5	Feedback resistance	50
3.4.6	Optimal values for a long-range sensing application	52
4	Linearization technique for interferometric fiber sensors	54
4.1	Overview	54
4.2	Theoretical background	55
4.2.1	Interferometric fiber sensors	55
4.3	2D denoising linearization	58
4.4	Experimental data acquisition	60
4.4.1	Working principle based on interferometry	60
4.4.2	Interrogation technique	61
4.4.3	Angle sensor setup	65
4.4.4	Liquid level sensor setup	66
4.5	Results and discussion	67
4.5.1	Angle sensor	67
4.5.2	Liquid level sensor	70
5	Conclusions, future works and new avenues	73
5.1	Distributed temperature sensing	73
5.2	Interferometric fiber sensors	74
5.3	New avenues	75

Bibliography**76**

List of Figures

1.1	Optical fiber waveguide showing the core of refractive index n_1 , surrounded by the cladding of slightly lower refractive index n_2 . (a) Cross-section. (b) Longitudinal section illustrating the transmission of a light ray in a perfect optical fiber.	2
1.2	Illustration of optical fiber sensors (a) Intrinsic sensors. (b) Extrinsic sensors.	6
2.1	Spectral features of Raman, Brillouin and Rayleigh scattering.	16
2.2	Raman distributed temperature sensor scheme.	19
2.3	Definition of spatial resolution for Raman distributed temperature sensors.	22
2.4	The response of an RDTS to square hot spots of varying width. From left to right the hot spots are 1 m, 50 cm, 30 cm, 15 cm, 10 cm, and 5 cm long. The blue horizontal line is the reference temperature. . . .	27
2.5	Temperature measurement error of the RDTS equipment as a function of the hot spot size for temperatures of the 80°C, 60°C and 40°C. All polynomial fittings were degree 2.	27
2.6	Calculation of the hot spot size by thresholding-based image segmentation for an RDTS experimental response to square hot spots of varying width.	28
2.7	Experimental setup for temperature data acquisition.	29
2.8	Unfolded fiber arrangement inside and outside the thermal bath. . . .	29
2.9	Two-dimensional temperature raw map formed from top view of the measured temperature profiles as a function of time and distance. . .	31
2.10	Two-dimensional temperature processed map formed from top view of the measured temperature profiles as a function of time and distance. .	32
2.11	Temporal evolution of temperature over the 50 cm hot spot located at position 126 m on the sensing fiber.	33
2.12	Two-dimensional temperature raw map formed from top view of the measured temperature profiles as a function of time and distance. . .	33

2.13	Two-dimensional temperature processed map formed from top view of the measured temperature profiles as a function of time and distance.	34
2.14	Temporal evolution of temperature over the 50 cm hot spot located at position 126 m on the sensing fiber.	34
2.15	Spatial evolution of temperature trace at a specific time of acquisition. The reference temperature at the hot spots tops was 60°C.	35
3.1	Illustration of a semiconductor slab used as a photodetector.	39
3.2	Illustration of an APD together with the electric-field distribution inside several layers under reverse bias.	41
3.3	Structure for the front end of the optical fiber receiver under analysis. The photodiode is modeled as a current source.	43
3.4	Sensitivity of anti-Stokes signal to temperature.	45
3.5	Minimum value of signal to noise ratio as a function of accuracy for different room temperatures (T_r) of 300 K, 350 K, and 400 K.	46
3.6	Gain of multiplication of the APD as a function of sensor accuracy considering the values of SNR_{min}	48
3.7	SNR versus APD gain for different sensor lengths.	48
3.8	To the left: Optimum APD gain as a function of sensor length. On the right: Maximum SNR obtained for a given gain as a function of the sensor length.	49
3.9	To the left: Optimum sensor range as a function of receiver bandwidth for a given optimum gain value. On the right: Optimum APD gain.	49
3.10	Signal to noise ratio as a function of the feedback resistance.	51
3.11	Optimal values for a long-range sensing application versus the maximum SNR.	52
4.1	Fiber arrangement using an off-setted fiber with reduced core to generate cladding modes. Three different types of optical fibers (SMF, RCF, and MMF) were employed to build the proposed sensors.	61
4.2	Illustrative scheme of the simulations of the changes in the interference pattern when optical losses occur in the cladding of the sensing fiber.	62
4.3	Interference pattern as a function of wavelength for the electric field amplitudes in the sensor cladding corresponding to 100%, 50%, 25% and 12.5% of its initial value.	63

4.4	Measurement of the intensity variability of the interference pattern (for a single level value) calculated from the difference between peak and dip values.	64
4.5	Experimental setup of the optical fiber angle sensor. (a) 3D view. (b) Top view.	65
4.6	Schematic diagram of the experimental setup for the liquid level measurement, where the sensing fiber is placed inside a pipette in which liquids can be readily inserted or removed.	66
4.7	Image formed from top view of the measured spectra as a function of angle. (a) Raw image. (b) Denoised image.	68
4.8	Three-dimensional map of the measured raw spectra as a function of angle.	68
4.9	Three-dimensional map of the measured denoised spectra as a function of angle.	69
4.10	Non-linearized sensor characterization curve for angle measurements (after Ref.[195]).	69
4.11	Linearized sensor characterization curve for angle measurements. . . .	70
4.12	Non-linearized linearity map for angle measurement.	70
4.13	Linearized linearity map for angle measurement.	71
4.14	Non-linearized sensor characterization curve for liquid level measurements.	71
4.15	Linearized sensor characterization curve for liquid level measurements. .	72

List of Acronyms

APD	Avalanche PhotoDiode
CMRR	Common-Mode Rejection Ratio
FPGA	Field Programmable Gate Array
IFS	Interferometric Fiber Sensor
MSE	Mean Square Error
MMF	Multi-Mode Fiber
NEP	Noise Equivalent Power
NLM	Non-Local Means
OSA	Optical Spectrum Analyser
RDTS	Raman Distributed Temperature Sensor
RCF	Reduced Core Fiber
SNR	Signal to Noise Ratio
SMF	Single Mode Fiber
3D	Three-Dimensional Space
2D	Two-Dimensional Space

List of Symbols

P_{abs}	Absorbed power
α	Absorption coefficient
φ	Acceptance angle of an optical fiber
δT	Accuracy of the Raman distributed temperature sensor
A_1	Amplitude of the electric field E_1
A_2	Amplitude of the electric field E_2
α_{AS}	Attenuation of the anti-Stokes signal
α_S	Attenuation of the Stokes signal
E_g	Bandgap
B_w	Bandwidth of the receiver
$B_{w_{op}}$	Bandwidth optimum value of the receiver
S	Binary image resulting from segmentation
k_B	Boltzmann's constant
Γ_{AS}	Capture coefficient of the anti-Stokes signal
a_0, \dots, a_{n-1}, a_n	Coefficients of a polynomial function
θ_c	Critical angle
j	Designates an interference spectrum curve (Chapter 2)
i	Designates an interference spectrum region (Chapter 2)
R^2	Determination coefficient
n_{AS}	Distribution of Bose-Einstein of the anti-Stokes signal
z_k	Each position along with the sensing fiber
$n_{eff,m}^{cl}$	Effective refractive index of the fiber cladding modes
n_{eff}^{co}	Effective refractive index of the fiber core mode
E_r	Electric field reaching the end of the fiber
E_2	Electric field that propagate in the fiber cladding
E_1	Electric field that propagate in the fiber core
q	Electron charge
I	Entire domain of the image
$\triangle E$	Energy difference between two photons
F	Excess noise factor

R_F	Feedback resistance
b	Fiber optic cladding radius
a	Fiber optic core radius
f	Frequency of a photon of the incident light
G	Gain of the pre-amplifier
GeO_2	Germanium dioxide
n_{gr}	Group refractive index of the fiber core
D	Hot spot size
θ	Incidence angle at the core-cladding boundaries
P_{in}	Incident optical power
E_i	Initial electric field that comes from the optical source
I_{MZI}	Intensity of interference pattern
I_{AS}	Intensity of the anti-Stokes signal
I_S	Intensity of the Stokes signal
$R(z)$	Intensity ratio of the anti-Stokes and Stokes signals
I_{du}	Leakage current
z	Length of the waveguide (Chapter 4)
ω	Light beam angular frequency
$I_{cl,m}$	Light intensity of the fiber cladding modes
I_{co}	Light intensity of the fiber core mode
SNR_{max}	Maximum signal to noise ratio
$\overline{\Delta I_j}$	Mean value of $\Delta I_{i,j}$
SNR_{min}	Minimum signal to noise ratio
p	Monitored physical parameter
M	Multiplication gain factor of the photodiode
M_{opt}	Multiplication gain factor optimum value of the photodiode
i_n^2	Noise current spectral density
n	Non-negative integer (Chapter 2)
$Z(i)$	Normalization factor
$norm$	Normalization operation between 0 and 1
N^2	Number of pixels of the image
N	Number of subdivisions of the interference spectrum
V	Parameter that determines the propagating modes number in a fiber
I_{dm}	Part of the dark current of the photodiode
$f(i)$	Pixel i value

$f(j)$	Pixel j value
h	Planck's constant
$z_{k=r}$	Position of the smallest hot spot in the fiber of size d
z	Position vector along the sensing fiber (Chapter 2)
$I_{AS,r}$	Power of the anti-Stokes signal reaching the photodiode
P_{tr}	Power transmitted
I_p	Primary photocurrent generated in the photodiode
η	Quantum efficiency of a photodetector
ν_R	Raman shift
T_{ref}	Reference temperature (either stabilized or monitored)
n_2	Refractive index of the fiber optic cladding
n_1	Refractive index of the fiber optic core
ϕ_m	Relative phase between the core and the cladding modes
\Re_{APD}	Responsivity of an avalanche photodiode
\Re	Responsivity of the detector
T_r	Room temperature
Q	Search window size
ε_{AS}	Sensitivity of the anti-Stokes signal
j	Set of all pixels in an image (Chapter 2)
k	Set of spectral regions i of an interference spectrum
η_i	Similarity neighborhoods of pixels i
η_j	Similarity neighborhoods of pixels j
P	Similarity window size
d	Size of the smallest hot spot in the sensing fiber
β	Smoothing control parameter
δz	Spatial resolution of the RDTS
i	Specific pixel of an image (Chapter 2)
k	Specific position along the sensing fiber (Chapter 2)
c	Speed of light in vacuum
$T(z)$	Temperature along the sensing fiber
e_T	Temperature error of the RDTS
T_k	Temperature in position k on the sensing fiber
z_{ref}	The end of the reference coil
ϵ	Threshold value
τ_{RC}	Time constant

C_T	Total capacitance
L	Total fiber length (sensor length or laser cavity size)
$f(\eta_i)$	Total value of similarity neighborhoods of pixels i
$f(\eta_j)$	Total value of similarity neighborhoods of pixels j
τ_{tr}	Transit time
$f(x, y)$	Two-variable function
$D_{i,j}$	Value of a dip in the interference pattern
$P_{i,j}$	Value of a peak in the interference pattern
ΔI_{AS}	Variation in the intensity of the anti-Stokes signal
$\Delta I_{i,j}$	Variation in the intensity of the interference pattern
λ_0	Wavelength in vacuum (Chapter 4)
λ_0	Wavelength of incident light (Chapter 2)
λ_{AS}	Wavelength of the anti-Stokes component
λ	Wavelength
λ_2	Wavelength of the refractive indice of the fiber cladding
λ_1	Wavelength of the refractive indice of the fiber core
λ_S	Wavelength of the Stokes component
κ	Wavenumber
ν_R	Wavenumber referring to Raman scattering
$w(i, j)$	Weighting factors of pixels i and j
W	Width of a slab used as a photodetector
τ	Width of the laser pulse
x	x-axis
y	y-axis

For my father Luiz and my mother Maria.

Chapter 1

Introduction

1.1 Overview

Optical fibers are recognized among the top innovations of the twentieth century, and Sir Charles Kao, a visionary enthusiast who championed their use as a medium for communication operations, received the 2009 Nobel Prize in Physics [1]. Optical fiber communications have become a vital backbone of today's digital world and internet infrastructure, making it possible to transmit large volumes of data over long distances with high integrity [2–4]. In effect, most of the world's data stream nowadays is as light photons in a global network of optical fiber cables. As the optical fiber industry turned fifty in 2016, the field might be middle-aged, but much more progress and societal benefits are expected of it. What has made optical fibers and fiber-based telecommunications so effective and pervasive in contemporary society?

It is its intrinsic characteristics and abilities that make it so versatile and very powerful as an enabling and transformative technology. Among their features, we have their electromagnetic immunity, low attenuation, intrinsic safety, small size, and weight, capability to perform multi-point and multi-parameter sensing remotely, and so on [5, 6]. Optical fiber sensors hold these same qualities. Initially, optical sensor devices were just laboratory investigations and simplified proof-of-concept demonstrations [7]. Nowadays, however, optical fiber sensors are providing a massive impact and economic transformations in industrial sensing, biomedical applications, as well as in military and defense operations, and have spanned applications as diverse as oil well downhole pressure sensors to intra-aortic catheters [8–14]. Particularly, this doctoral thesis will present a set of investigations based on signal processing and computational modeling to improve the performance of two classes of optical fiber sensors: Raman-based distributed temperature sensors (RDTSS) and interferometric fiber sensors (IFSs).

1.2 Optical fiber waveguides

Optical fibers are dielectric waveguides with a cylindrical structure constituted of a central core with radius a and refractive index n_1 surrounded by an outer cladding with radius b and refractive index n_2 lower than n_1 as illustrated in Figure 1.1. Since the fiber core has a higher refractive index than the surrounding fiber cladding, the light ray is confined and guided into the fiber core through the total internal reflection principle, in which the incidence angle θ at the core-cladding boundaries is large than the critical angle [6]:

$$\theta_c = \sin^{-1} \left(\frac{n_2}{n_1} \right). \quad (1.1)$$

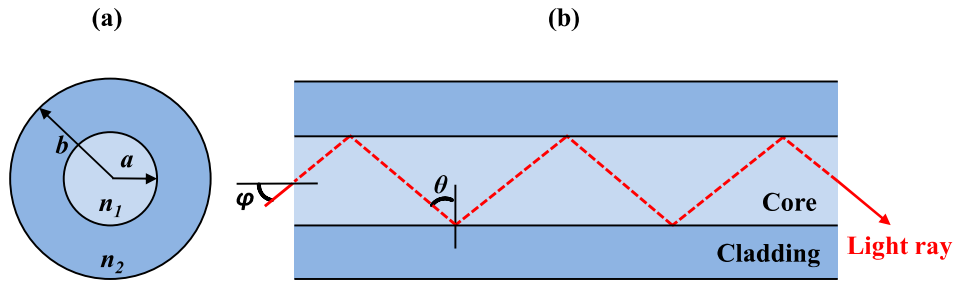


Figure 1.1: Optical fiber waveguide showing the core of refractive index n_1 , surrounded by the cladding of slightly lower refractive index n_2 . (a) Cross-section. (b) Longitudinal section illustrating the transmission of a light ray in a perfect optical fiber.

The light ray exhibited in Figure 1.1(b) is a simplified representation generally used to illustrate the fundamental transmission properties of optical fibers. It must also be noted that the light transmission illustrated in Figure 1.1(b) considers a perfect optical fiber and that any discontinuities or imperfections at the core-cladding interface would probably result in refraction rather than total internal reflection, with the subsequent loss of the light ray into the cladding. In principle, the light wave travels in both the core and the cladding allowing that part of associated energy to decay to a negligible value at the cladding-air interface [6].

Also, it may be observed in Figure 1.1(b) that the light ray enters the fiber core at an angle φ to the fiber axis. In general terms, any rays which are incident into the fiber core at an angle greater than φ will be transmitted to the core-cladding interface at an angle less than θ_c , and will not be totally internally reflected. Moreover, if an incident ray at an angle greater than φ , it will be refracted into the cladding and

eventually lost by radiation. Hence φ is the maximum angle to the axis at which light may enter the fiber in order to be propagated, and is often referred to as the acceptance angle for the optical fibers.

Another relevant concept concerning light propagation in an optical fiber is the number of modes that are allowed to propagate in it. Maxwell's equations applied to the propagation of light waves in an optical fiber reveal that only a restricted number of transverse electromagnetic field patterns are allowed to propagate in it. A fiber that guides just the fundamental mode is denominated single-mode fiber (SMF), while if it supports also other high-order modes then the fiber is designated multi-mode fiber (MMF) [6]. The parameter that determines the number of guided modes propagating in optical fiber for each given wavelength λ is the denominated V parameter, described by [6]:

$$V = \frac{2\pi a}{\lambda} \sqrt{n_1^2 - n_2^2}. \quad (1.2)$$

For an optical fiber to be single-mode it is required to fabricate it with a V value lower than 2.405. However, it is important to notice that the number of modes in fiber is wavelength-dependent, and for a given fiber, the wavelength at which high-order modes cease to propagate is denominated the cut-off wavelength [5, 6].

In terms of the manufacture of optical fibers, it can be highlighted here that low-loss optical fibers are currently made from high-silica glasses, i.e. a mixture of glasses consisting essentially of fused silica, to which other materials are added to raise or lower the refractive index. Germania, phosphorus pentoxide, and (less commonly used) alumina raises the refractive index, whereas fluorine reduces it. These additives also modify other properties of silica, such as its softening temperature, expansion coefficient, dispersion, stress-optical effect, attenuation, and susceptibility [15–19].

Although silica was well known for its low attenuation, the breakthrough in fiber fabrication emerged with vapor deposition processes, such as chemical vapor deposition [20], flame hydrolysis [21], and plasma deposition [22], which all allowed the glasses to be synthesized directly into a starter rod (known as a preform) that could be drawn straight into a fiber with minimal intermediate manipulation. The fiber glasses are produced by oxidizing starting halide materials that are liquid and can be purified to a high degree through bulk chemical processing. The vapor deposition methods enable the extreme purity of the starting materials and of the oxygen used in the chemical process to be preserved in the glass that is produced.

Employing the modified chemical vapor deposition process technique, an optical fiber with a loss as low as 0.2 dB/km at 1550 nm was produced in 1979 [23]. However, even this fiber had an impurity level sufficient to cause an absorption peak of approximately 10 dB/km at 1380-1390 nm. In the following years, improved purity in the manufacturing process and changes in fiber design led to commercially available fibers guaranteed to provide a loss of 0.15 dB/km [24], with typical peaks at 1380-1390 nm just a few tenths of 1 dB/km. Some commercially available fibers exhibit essentially no discernible absorption at 1380–1390 nm. These optical fibers are now widely used in the development of several optical devices with applications in communications and sensing operations.

1.3 Optical fiber sensors

Optical fiber sensors are devices that use light to convey the information which they sense. A typical optical fiber sensor system consists of the sensor itself that is probed by an input light which it modifies in accordance with the value of the measured physical parameter. The system also comprises an optical fiber within a transit cable that carries the input light to the sensor and send the modulated light from the sensor to the interrogator through a patch panel that houses the connectors or splices. The interrogator is the optoelectronic equipment that releases an input light and converts the returned light into an electrical signal which is processed to produce the output of the sensor device. This sensor is designed to respond only to the expected parameter of interest and ideally not at all to any other external influence. Besides, the transit cable, that carries the input light and the returning optical signal, should protect the fibers from external influence and from damage caused by the environment [7].

In the early 1970s, significant advancements were made in optical fiber technology for the telecommunications field, including low loss fibers [25], stable laser diodes working at room temperature [26], and a better understanding of the design of the signal transmission. This progress directed to pioneering ideas concerning using this same technology for physical [27–30] and chemical [31] sensing. Several approaches were proposed by the scientific community at the time, demonstrating that optical fibers could be also employed as sensor devices for a broad diversity of physical and chemical parameters. The continuity of this research also revealed that many attributes of the light traveling inside an optical fiber cable could be used

in the sensing assignment, including its intensity [32], polarization [33], phase [34], propagation time [30], optical spectrum [35] and coherence [36].

Consequently, a promising sensing optical fiber technology emerged, capable to provide compact, lightweight sensors that could be developed to match a wide variety of operating areas, power, and environmental restrictions. In particular, the ability of optical sensors to carry the information in the optical domain from hostile conditions to the interrogating electronics positioned in a more favorable location allowed the evolution of sensors operating in high-temperature circumstances, for instance, in borehole industrial installations [37].

Moreover, the electrically inactive optical fibers enabled sensors to be installed inside high-voltage transformers and power energy cables and consequently allowed low-cost monitoring of these expensive structures [38, 39]. On this scale, optical fiber sensors are frequently relatively expensive as individual elements but are cost-effective when all features of the sensor device are considered. Optical fiber sensors can be also built to be insensitive to electromagnetic interference, and still, sob different configurations, they are used as current [40, 41] or voltage [42, 43] sensors.

Optic fiber sensors can be either intrinsic Figure 1.2(a) or extrinsic Figure 1.2(b). In intrinsic sensors, the light stays inside the optical fiber throughout the sensor device and is modulated within the fiber, for example, by induced loss, changes to its spectrum or polarization, and so on. On the other hand, in extrinsic sensors, the sensor is a bulk-optic device, such as an electro-optic crystal, or a strain-birefringent element located between crossed polarisers; in another example, it might be a fluorescent element that absorbs input light from the fiber and re-emits fluorescent light at a distinct wavelength that is collected by the transit fiber and taken to the interrogator component [7, 44–47].

As more approaches and applications for optical fiber sensors began to emerge on a larger scale, the issue of their cost has become even more concerned. Using these sensors in applications that required a high installation cost, such as monitoring hostile environments, was one of the strategies adopted at the beginning of the development of this technology in order to obtain a better understanding of how to make progress with this sensor technology. However, in most applications, the optical sensors were extremely expensive so they proved to be unattractive and not competitive compared to cheaper and more well-established technologies that are already available in the industry. This led to new investigations that proposed multiplexing several optical sensors in a single fiber cable [48–51] and sharing the

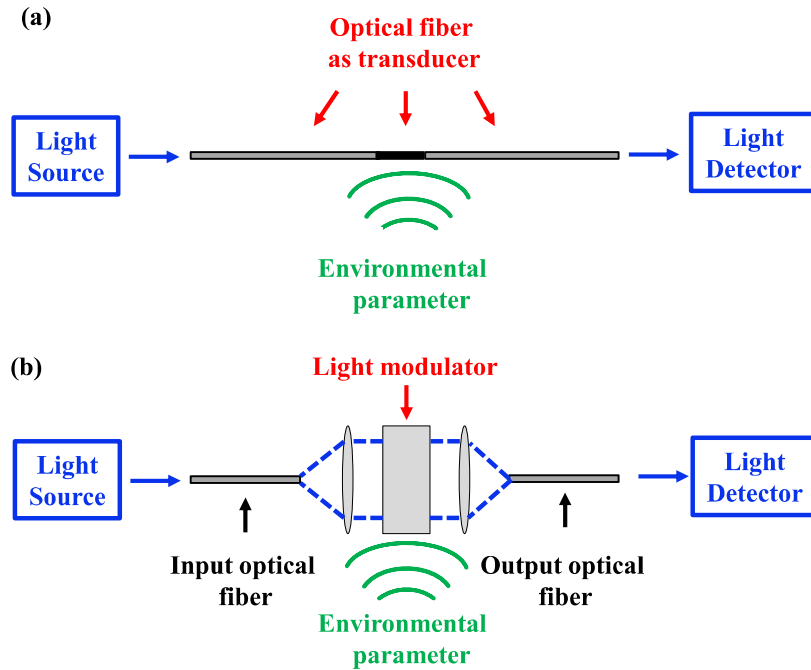


Figure 1.2: Illustration of optical fiber sensors (a) Intrinsic sensors. (b) Extrinsic sensors.

interrogator among many sensing points, thus reducing the cost per point of the sensor equipment. In addition, the possibility of installing control room wiring for optical sensors has made it possible to significantly reduce their cost and now place them at a competitive level, and even attractive in many cases.

Multiplexed fiber sensors acquired acceptance in applications where an array of sensors in well-defined positions were required, such as hydrophone arrays for naval sonar operations: these devices demand repeated measurement points at specified locations, normally on a linear array or two-dimensional grid [7]. Nevertheless, in the multiplexed sensing approach, mapping the entire spatial profile of a physical parameter, without any a priori information of the form of the distribution requires an unreasonable number of sensing points, principally where the spatial frequency of the information could be very high. For example, the current-carrying capacity of the buried energy cable is determined by the temperature of its hottest point. If the width of the hot spot is as short as 1 to 2 meters depending on the dimensions of the conductors, it will be necessary to correctly detect these short hot spots for a long-buried cable of length, e.g. 10 km, about 10000 sensing points. However, this monitoring can be accomplished with a spatial resolution of the order of 1 meter if a distributed optical fiber sensor is employed [52].

Last but not least, the main aspects of the performance of optical fiber sensors are described by [7]:

- The physical parameter resolution. It is the ability of the sensor to distinguish small changes in the value of the quantity that is measured. In general, the physical parameter resolution is a function of location because the signal measured by the sensor is increasingly attenuated with increasing the distance along the sensing fiber.
- The spatial resolution. In the case of a distributed sensor, the spatial resolution is the ability to distinguish the value of the measured parameter at closely spaced locations, calculated by as the distance over which the sensor output corresponding to transition estimated between 10% and 90% of the signal. However, it is important to emphasize here that there is another way to define this parameter, taking into account the pulse width of the laser source used. In general, if the spatial features of the physical parameter resolution are finer than the spatial resolution of the sensor equipment, crucial details of the signal measured by the sensor will be completely lost.
- The range. It is the maximum length of sensing fiber that can be measured. The range parameter is associated with the cumulative loss to the most remote point to be sensed and a system specification can be based on a maximum fiber length with a defined maximum loss per unit length.
- The measurement time. It is the time taken by the sensor device to acquire the readings for all points in the sensing fiber to achieve the stated measurement resolution. In long fiber sensors, the weaker signals from the remote end will be below the noise level, and it is common to apply considerable averaging to improve the signal-to-noise ratio (SNR). In this context, signal averaging means making repeated measurements of the backscatter signal and summing the results point-by-point along the fiber. Assuming that the noise is uncorrelated between successive acquisitions, the SNR improves in proportion to the square root of the number of accumulated waveforms. However, this action considerably increases the measurement time.

1.4 Motivation

Several industrial applications require precise, robust, and highly reliable sensors. Many accidents even with fatal victims could have been avoided if an adequate monitoring system was employed. Particularly in Brazil, two of the biggest industrial disasters have occurred a few years ago. The first one was the Fundão dam failure in the subdistrict of Bento Rodrigues, 35 km from the municipality of Mariana in Minas Gerais State on November 5, 2015 [53]. The failure of this dam is considered the industrial disaster that caused the greatest environmental impact in Brazilian history and the largest in the world involving tailings dams. Also, more than 40 million m³ of tailings reached one of the main hydrographic basins covering several municipalities, many of which supply their population with this water. The other accident was the collapse of the dam in Brumadinho, Minas Gerais on January 25, 2019, which is considered the biggest work accident in Brazil in terms of loss of human life [54]. Several other accidents around the world in tunnels [55], pipelines [56], oil platforms [57], and mines [58] could also be mentioned. In this perspective, the need to develop better monitoring technologies is an indispensable issue. To concentrate attention on this problem, this doctoral research had the main purpose to develop solutions based on signal processing for optical fiber sensors making them more precise and with more possibilities of application.

1.5 Organization of the thesis

The contributions of this doctoral research cover two classes of fiber sensors: RDTs and IFSs. In this way, for the presentation of this thesis, a text composed of five chapters was elaborated. Initially, this chapter 1 is dedicated to presenting the basic concepts of optical fiber sensor devices, the motivation for carrying out this research work, the structure of this thesis, the publications generated, and the main achievements.

Subsequently, the chapters 2 and 3 gathers all investigations carried out with the RDTs. A proposal for the high precision detection of small temperature events on the scale of a few centimeters is presented in chapter 2. For this end, not only a 2D reconstruction of the temperature profiles measured by the sensor equipment is performed, but also an empirical model is developed that allows correcting the sensor response with an accuracy of 98.22%. Furthermore, a theoretical analysis of the

receiver of these sensors to improve its sensitivity through hardware modifications is presented in chapter 3.

Besides, chapter 4 introduces a linearization technique for IFSs. Experimental validations are presented for angle and liquid level measurement IFSs. The results show that our linearization technique is capable to improve not only the linearity, but also the operating range of existing IFSs. Finally, the final considerations of the thesis and perspectives for future works are discussed in chapter 5.

1.6 Publications

In the time frame of the thesis, 16 journal papers, and 6 conference papers were published. These publications include those related to the thesis theme and the other ones from collaborations and parallel researches.

1.6.1 Journal articles

[1] Luís C. B. Silva, Jorge L. A. Samatelo, Marcelo E. V. Segatto, João P. Bazzo, Jean C. C. Silva, Cicero Martelli, and Maria J. Pontes, "NARX neural network model for strong resolution improvement in a distributed temperature sensor," *Applied Optics*, vol. 57, no. 20, pp. 5859–5864, July, 2018.

[2] Luís C. B. Silva, Yuli A. A. Pizarro, Mariana A. Vieira, Jair C. C. Freitas, Marcelo E. V. Segatto, Maria J. Pontes, and Carlos E. S. Castellani, "All-Fiber Erbium-Doped Q-Switched Laser With Recycled Graphite Oxide," *IEEE Photonics Technology Letters*, vol. 31, pp. 1713-1716, September, 2019.

[3] Luís C. B. Silva, Yuli A. A. Pizarro, Mariana A. Vieira, Jair C. C. Freitas, Marcelo E. V. Segatto, Maria J. Pontes, and Carlos E. S. Castellani, "Stable dark pulses produced by a graphite oxide saturable absorber in a fiber laser cavity," *Applied Optics*, vol. 58, pp. 9297-9304, November, 2019.

[4] Luís C. B. Silva, Lorenzo B. Scandian, Marcelo E. V. Segatto, and Carlos E. S. Castellani, "Optical spectral intensity-based interrogation technique for liquid-level interferometric fiber sensors," *Applied Optics*, vol. 58, pp. 9712-9717, December,

2019.

[5] Luís C. B. Silva, Rodolpho L. Silva, and Carlos E. S. Castellani, "2D denoising technique for the linearization of interferometric fiber sensors," *Applied Optics*, vol. 59, pp. 3038-3042, April, 2020.

[6] Luís C. B. Silva, Eduarda P. Silva, Felipe R. Audibert, and Carlos E. S. Castellani, "Simulation solution for single and cascaded multi-wavelength Brillouin fiber lasers based on an analytical model," *Optical Fiber Technology*, vol. 59, p. 102317, October, 2020.

[7] Luís C. B. Silva, Bruna D. M. Lopes, Maria J. Pontes, Isidro M. Blanquet, Marcelo E. V. Segatto, Carlos A. F. Marques, "Fast decision-making tool for monitoring recirculation aquaculture systems based on a multivariate statistical analysis," *Aquaculture*, vol. 530, p. 735931, January, 2021.

[8] Luís C. B. Silva, Patrick M. Ciarelli, Jean C. C. Silva, Igor B. V. Costa, Marcelo E. V. Segatto, Maria J. Pontes, and Carlos E. S. Castellani, "Detection of multiple small temperature events simultaneously on a distributed temperature map," *IEEE Sensors Journal*, vol. 21, no. 4, pp. 4582-4589, February, 2021.

[9] Bruna D. M. Lopes, Luís C. B. Silva, Isidro M. Blanquet, Pétia Georgieva, and Carlos A. F. Marques. "Prediction of fish mortality based on a probabilistic anomaly detection approach for recirculating aquaculture system facilities," *Review of Scientific Instruments*, v. 92, n. 2, p. 025119, February, 2021.

[10] Luís C. B. Silva, Carlos A. F. Marques, Marcelo E. V. Segatto, and Maria J. Pontes. "Stable self-pulsing regime in a Brillouin ring fiber laser cavity," *Laser Physics*, v. 31, p. 102484, April, 2021.

[11] Luís C. B. Silva, and Carlos E. S. Castellani. "Numerical analysis of the pump's spectral linewidth impact on single and multi-wavelength Brillouin fiber lasers," *Laser Physics*, v. 31, p. 055104, April, 2021.

- [12] Luís C. B. Silva, Carlos E. S. Castellani, Marcelo E. V. Segatto, and Maria J. Pontes. "Analytical investigation of the receiver for Raman-based distributed temperature sensors," *Optical Fiber Technology*, v. 63, p. 102484, May, 2021.
- [13] Luís C. B. Silva; Bruna D. M. Lopes, Isidro M. Blanquet, and Carlos A. F. Marques. "Gaussian Distribution Model for Detecting Dangerous Operating Conditions in Industrial Fish Farming". *Applied Sciences*, v. 11, p. 5875, June, 2021.
- [14] Luís C. B. Silva; Carlos E. S. Castellani. "Recent progress in optical dark pulses generation based on saturable absorber materials". *Optical Fiber Technology*, v. 64, p. 102560, July, 2021.
- [15] Luís C. B. Silva; Caio M. Santos; Marcelo E. V. Segatto; Maria J. Pontes. "Long-haul propagation analysis of dark pulses employing an optical recirculating fiber loop technique". *Optics Communications*, v. 495, p. 127070, September, 2021.
- [16] Rui Min; Xuehao Hu; Luis Pereira; M. Simone Soares; Luís C. B. Silva; Guoqing Wang; Luis Martins; Hang Qu; Paulo Antunes; Carlos A. F. Marques, Xiaoli Li, "Polymer optical fiber for monitoring human physiological and body function: A comprehensive review on mechanisms, materials, and applications". *Optics & Laser Technology*, v. 147, p. 107626, November, 2021.

1.6.2 Conference papers

- [1] Luís C. B. Silva, Helder R. O. Rocha, Carlos E. S. Castellani, Marcelo E. V. Segatto, and Maria J. Pontes, "Improving Temperature Resolution of Distributed Temperature Sensor Using Artificial Neural Network", in *International Microwave and Optoelectronics Conference (IMOC)*, Águas de Lindóia, SP/Brazil, August, 2017.
- [2] Luís C. B. Silva, Marcelo E. V. Segatto, and Maria J. Pontes, "Characterization of Raman Distributed Temperature Sensor Receiver," in 18 SBMO - *Simpósio Brasileiro de Microondas e Optoeletrônica* e 13 CBMAG - *Congresso Brasileiro de*

Eletromagnetismo (MOMAG), Santa Rita do Sapucaí, MG/Brazil, August, 2018.

[3] Luís C. B. Silva, Jorge L. A. Samatelo, Marcelo E. V. Segatto, and Maria J. Pontes, “Influence of the Thermal Effect on the DTS Calibration”, in *Optical Sensors and Sensing Congress*, San Jose, California/USA. Optical Society of America, June, 2019.

[4] Luís C. B. Silva, Jorge L. A. Samatelo, Marcelo E. V. Segatto, and Maria J. Pontes, “Adaptive Data Compression Method for Distributed Temperature Sensors”, in *Second Latin American Workshop on Optical Fiber Sensors (LAWOFS)*, Rio de Janeiro, RJ/Brazil, July, 2019.

[5] Luís C. B. Silva, Igor B. V. Costa, Jean C. C. Silva, Jorge L. A. Samatelo, Marcelo E. V. Segatto and Maria J. Pontes, “Distributed Sensor Calibration by Gaussian Approximation”, in *International Microwave and Optoelectronics Conference (IMOC)*, Aveiro, Portugal, November, 2019.

[6] Luís C. B. Silva, Carlos E. S. Castellani, Marcelo E. V. Segatto, and Maria J. Pontes, “High accuracy hot spot size estimation technique for Raman Distributed Temperature Sensors”, in *International Microwave and Optoelectronics Conference (IMOC)*, Aveiro, Portugal, November, 2019.

1.7 Main achievements

In the author’s opinion, the main scientific contributions reported in this thesis within the scope of optical fiber sensors are the following:

- The development of a technique to estimate the hot spot size for RDTs.
- The development of a signal processing technique that allows correcting the temperature reading of RDTs for hot spots smaller than the equipment’s spatial resolution.
- Realization of an analytical study of an RDT receiver that addresses possible directions to improve the sensitivity of this sensor device.

- The development of a linearization technique for interferometric fiber sensors to increase its linearity and operation range.

Throughout the doctorate of the author which originated this thesis, other investigations/studies outside the main scope of this thesis were carried out from the author's interest. These parallel investigations to the central theme of this thesis provided other scientific contributions to fiber laser devices and the fish farming industry as can be seen in the list of publications. Specifically, the main scientific contributions not directly related to the theme of this thesis are:

- The development of a decision-making tool for monitoring recirculation aquaculture systems based on a multivariate statistical analysis.
- The development of a simulation solution for single and cascaded multi - wavelength Brillouin fiber lasers based on an analytical model.
- Experimental study of the use of graphite oxide as a saturable absorber material for the generation of pulses in Q-Switched regime and dark pulses as well.

Chapter 2

Detection of small distributed temperature events

2.1 Overview

Measuring temperature is essential in many industrial applications not only to preserve equipment lifespan but also for security reasons. One solution that has grown exponentially in recent years due to its distributed measurement capability is the RDTSSs that enable the temperature to be mapped at several points along tens of kilometers of fiber optic cables. In spite of being a technology already present in the industry, it shows no sign of abating with progress being achieved in basic interrogation, accuracy improvements, and novel applications. Currently, the scientific literature in the area of distributed temperature sensing exhibits a consistent body of knowledge based on the solutions that allow temperature measurements with high precision and resolution. However, these approaches fail in situations when the temperature event is less than the equipment's spatial resolution, so that it cannot be detected correctly. In this perspective, we propose in this chapter an image processing technique applied to the temperature profile generated by these sensors that will allow circumventing this bottleneck of RTDS technology. As a result, the simultaneous detection and correction of hot spots of sizes ranging from 15 m to 3 cm are achieved experimentally with 98.22% accuracy. These results obtained here place the RDTSS technology at a new level of applicability, in which new industrial applications can be developed.

2.2 Theoretical background

2.2.1 Spontaneous scattering in optical fibers

Light scattering is a secondary electromagnetic wave that originates from the interaction of a light wave with the atoms and molecules that constitute a medium. The

optical fiber is a non-homogeneous medium so that light scattering processes in it are due to small variations in density, random ordering of the molecules, and the presence of dopants in the material that constitutes the fiber. Besides, light scattering processes can occur spontaneously when the scattered light does not significantly alter the property of the medium, and in a stimulated regime, otherwise [59]. In other words, the evolution from spontaneous to stimulated scattering corresponds to a transition of the medium response from a linear to a nonlinear regime.

When high-intensity light interacts with the molecules that make up the optical fiber material, energy exchanges will occur between the photons of the incident light and the molecules of this material (usually fused silica). These energy exchanges generate new electromagnetic fields with different frequencies that propagate in all directions [59]. If the frequency of the scattered light is less than the frequency of incident light (downshifted), the scattering process absorbs energy. This implies that the molecules in the medium absorbed energy from the photons of the incident light, producing scattered photons with less energy. This scattering effect gives rise to spectral components called Stokes [59]. On the other hand, if the scattered light has a higher frequency than that of the incident light (up-shifted), the molecules in the medium will give part of their energy to the photons of the incident light. This causes photons with greater energy to be generated. This scattering effect gives rise to spectral lines called anti-Stokes [59].

In these cases where there are frequency shifts of scattered light, the scattering process is called inelastic, such as Raman and Brillouin scattering. On the other hand, if there is no change in the frequency of the scattered light when compared to that of the light incident on the fiber, the scattering is called elastic, such as Rayleigh scattering. The Raman, Brillouin, and Rayleigh light scattering processes currently have a wide variety of applications in the field of photonics. Particularly in the sensing scenario, the exploration of these effects enabled the development of optical fiber sensor technologies to measure several physical parameters, such as temperature, strain, and vibration. These spectral features of Raman, Brillouin, and Rayleigh scattering are illustrated in Figure 2.1.

Specifically, the Rayleigh scattering is a linear scattering process in that the scattered power is proportional to the incident power. Also, no energy is transferred to the glass in Rayleigh scattering. It is associated with non-propagating density variations [60]. When the probe signal is coherent, the Rayleigh backscatter changes and it becomes sensitive to temperature and strain [59]. A practical demonstration

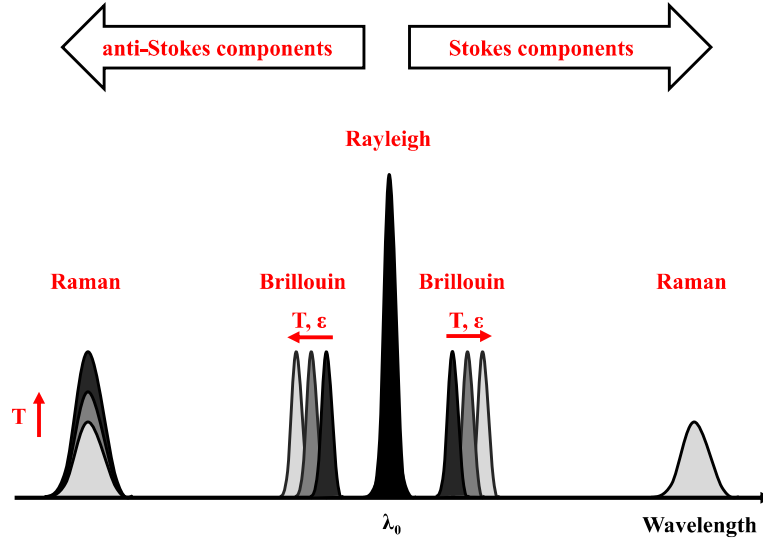


Figure 2.1: Spectral features of Raman, Brillouin and Rayleigh scattering.

of the sensitivity of the backscatter intensity in coherent optical time-domain reflectometry was published in 1994 [61]. Distributed acoustic or vibration sensing based on Rayleigh scattering has seen a rapid increase in research and commercial interest since about 2005, and the technology and its applications are progressing rapidly, with applications in intrusion detection of pipelines [62], seismic monitoring [63], subsea cable condition monitoring [64], among others [65, 66].

Brillouin scattering is a process that emerges from the interaction between an incident wave and thermally driven material-density fluctuations that travel at the speed of sound, i.e. hypersonic acoustic waves. In glasses, the Brillouin scattering is sensitive to strain and temperature in its frequency. Thus, the capability to measure the frequency shift of the Brillouin scattering has enabled distributed sensing technology to provide strain as well as temperature measurements. Some interrogation methods enable the strain and temperature to be determined independently [67]. Also, stimulated Brillouin scattering can be employed in sensing; indeed, the first published Brillouin sensing approaches were based on stimulated Brillouin scattering [68, 69]. The signal obtained in this case is a measure of the gain (or loss) in the interaction of two counter-propagating waves. This has led to some configurations where the signals interact only over very short distances, and, as a result, spatial resolutions in the millimeter range have been demonstrated [70]. Additionally, the very narrow linewidth of the Brillouin process permits optical amplification [71], and heterodyne techniques to be employed for improving the signal quality. This

has enabled Brillouin measurements to be carried out over extremely long distances [72].

In the case of Raman scattering, the light interacts with molecular vibrations, for example, stretching modes between atoms [73] within the molecule, i.e. the molecular vibration causes a fluctuation of the polarisability at the vibrational frequency which is then periodically different from that of other parts of the medium, resulting in scattering. Specifically, the amplitude of the anti-Stokes spectral component of Raman scattering is sensitive to temperature variations. However, variations in intensity in the anti-Stokes component that are not due to changes in temperature may occur, making it impossible to use Raman scattering properly for temperature sensing [7]. To solve this problem, some proposals have been developed. The most traditional one is to use the Stokes component of the Raman scattering as a reference signal to cancel the power losses resulting from the attenuation of the signal in the fiber and take the anti-Stokes/Stokes ratio to obtain the correct temperature information.

As part of this doctoral thesis is focused on the study of temperature sensors based on Raman light scattering on optical fibers, the entire approach from that point forward that will be presented in this chapter 2 and chapter 3 will be dedicated to discussing how this effect can be employed in the development of optical fiber sensors for distributed temperature measurements.

2.2.2 Spontaneous Raman scattering

Initially, it is important to emphasize that Raman scattering is a different process from the fluorescence phenomenon. Despite both processes transforming part of the incident light into a new wavelength band, in the fluorescence process, the photon energy is utilized to move an electron from a low-energy state to a meta-stable, higher-energy state within the electronic structure of an atom or a molecule. In this way, the fluorescence process relies upon the presence of an absorption band that is fixed in the spectrum. On the other hand, in Raman scattering, the emission band tracks the incident light by a fixed frequency shift that is independent of the wavelength of the incident light. Besides, the time scales are considerably different: fluorescence decay times can be very slow in glasses (in the microseconds to milliseconds scale); in contrast, the Raman response is on the order of femtoseconds [7].

It is quite common to confuse these two processes because Raman scattering is sometimes defined by reference to a virtual state to which the molecule transitions from a vibrational state before quickly releasing the energy by going back to another vibrational state. However, this virtual state does not report in general (The exception being resonance Raman scattering [73]) to a real electronic transition of an atom, as would be the case for fluorescence. Raman and fluorescence are therefore very different phenomena.

Another point of great relevance to be discussed here is that although Raman scattering involves some form of nonlinearity due to the frequency shift of scattered light, in most of the temperature sensors based on Raman scattering, the Raman process is linear in the sense that the scattered power is proportional to the incident power. Nonlinear (stimulated) Raman scattering also exists, but it is not commonly employed as a sensing mechanism. The onset of stimulated Raman scattering frequently restricts the amount of power that can be launched as a probe, and this effect limits the performance of RDTs [7].

The Raman process results in a frequency shift, with the resulting wavelengths of the anti-Stokes (λ_{AS}) and Stokes (λ_S) Raman scattered light dependent on the probe wavelength. Their relation to the incident light at wavelength λ_0 is as follows for wavelengths expressed in meters and frequency shift ν_R expressed in cm^{-1} [7]:

$$\lambda_{AS} = \frac{0.01}{\frac{0.01}{\lambda_0} + \nu_R}, \quad (2.1)$$

$$\lambda_S = \frac{0.01}{\frac{0.01}{\lambda_0} - \nu_R}. \quad (2.2)$$

As an example, the wavelength shifts correspond to $\nu_R = 440 \text{ cm}^{-1}$ work out at about 35, 50 and 100 nm for probe wavelengths of 904, 1064 and 1550 nm, respectively.

2.2.3 Raman-based distributed temperature sensors

RDTs belong to the class of distributed measurement fiber optic sensors that exploit spontaneous Raman scattering to obtain temperature information at several points along the entire length of a fiber optic cable [74–76]. Contrasted to other distributed fiber optic sensors [77, 78], RDTs has no cross-sensitivity with strain variations. This unique feature justifies its powerful presence for temperature measurements in different applications such as hydrologic systems [79], hydroelectric

generators stators [80], water leakage in dikes [81], oil depots [82], oil and gas wells [83], energy efficiency of buildings [84], heatsinks [85], nuclear reactors [86], tunnel fire detection [87], detection and fire extinguishing systems in aircraft [88], geological repositories for nuclear wastes [89], gas pipelines [90], power transmission lines [91], power transformers windings [92], solar ponds [93], ice caves [94], sewers [95], air temperature measurements in the atmospheric boundary layer [96], fractured rock aquifers [97], among others.

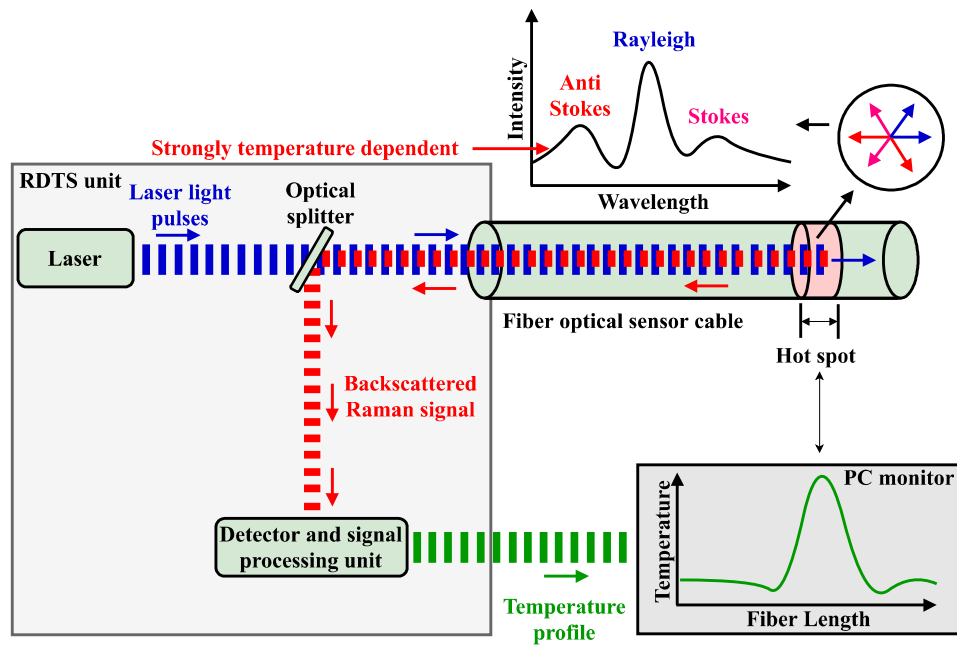


Figure 2.2: Raman distributed temperature sensor scheme.

RDTs employ the optical fiber cable itself as a sensor element, requiring no transducers along the entire optical path. Its basic operating principle is to launch light pulses into the optical fiber to generate the backscattered Raman spectrum [59], as depicted in Figure 2.2. The anti-Stokes and Stokes components contained in this spectrum are collected and processed in separate physical channels (with dedicated optical filters and detectors) to construct the temperature profile along the entire length of the fiber since the anti-Stokes component is considerably more sensitive to temperature variations than the Stokes component [7]. The temperature $T(z)$ along the sensing fiber is obtained by the ratio between the intensity of the

anti-Stokes and Stokes components (I_{AS}/I_S), according to the expression [7]:

$$\frac{1}{T(z)} = \frac{1}{T_{ref}} - \frac{k_B}{h \cdot v_R \cdot c} \ln(R(z)) + \frac{k_B}{h \cdot v_R \cdot c} \int_{z_{ref}}^z (\alpha_{AS}(z') - \alpha_S(z')) dz', \quad (2.3)$$

with:

$$R(z) = \exp\left(\frac{h \cdot v_R \cdot c}{k_B} \left(\frac{1}{T_{ref}} - \frac{1}{T(z)}\right)\right) \times \exp\left(-\int_{z_{ref}}^z (\alpha_{AS}(z') - \alpha_S(z')) dz'\right), \quad (2.4)$$

where h is Planck's constant, c is the speed of light in vacuum, k_B is the Boltzmann's constant, v_R is the Raman shift expressed in cm^{-1} . The coefficients α_{AS} and α_S represent the attenuation at the anti-Stokes and Stokes signals, respectively. z_{ref} is the end of the reference coil, i.e. the start of the sensing fiber. T_{ref} is the reference temperature (either stabilized or simply monitored) that makes it possible to carry out the sensor calibration process. And z is the position vector along the sensing fiber.

The ratiometric approach described by equations 2.3 and 2.4 enables parameters like the pulse energy, the capture fraction, and the attenuation at the probe wavelength to be canceled. However, the differential attenuation is not precisely determined. This parameter arises from the fact that the anti-Stokes and Stokes of Raman scattering have different wavelengths and therefore are attenuated differently along the fiber. Consequently, an inaccurate estimation of this differential loss can bias the temperature measurement of the RDTS equipment, because it is not possible to separate the effect of temperature from that of differential attenuation.

Giesen et al. [98] proposed to access both ends of the optical fiber simultaneously in a double-ended configuration in order to correct the effects caused by the differential attenuation. However, this proposal finds its limitations, since it assumes that the losses in the fiber are uniform and constant along the entire length of the fiber. Where the fiber losses are not uniform (caused by splices, sharp bends, pinching, or differential stress on the fiber), the double-ended measurement is not able to correct the differential loss.

Looking for a solution to the differential loss that takes into account non-uniform losses, Lee et al. [99] used two light sources in which their wavelengths are selected such that the anti-Stokes component of the primary light source coincides in wavelength with the Stokes component of the secondary light source. Such a method

enables a corrected attenuation profile, which results in a correct temperature measurement. Nevertheless, in double-ended configurations the sensor range is reduced by half, and in the approach presented at [99] the cost and complexity of the sensor is higher due to the employment of two laser sources.

The performance of RDTs is determined by the temperature resolution, spatial resolution, range and by the response time (measurement time) to achieve the stated measurement resolution [7]. The spatial resolution denoted by δz can be described as the distance over which the sensor output corresponding to transition estimated between 10% and 90% in the value of the read temperature [7]. It means the ability of the sensor in measure correctly the value of the temperature at closely spaced locations, as shown in Figure 2.3. Note that δz is not the same as sampling resolution. This latter is the fiber distance between two samples of the raw analogue signal. Moreover, δz can be defined mathematically by [7]:

$$\delta z = \frac{c \cdot \tau}{2n_{gr}}. \quad (2.5)$$

In this equation, c is the velocity of light in vacuum, τ is the width of the laser pulse, and n_{gr} is the group refractive index of the fiber core. Commercial RDTs generally employ pulsed lasers with $\tau = 10$ ns, corresponding to $\delta z \simeq 1$ m. On the other hand, the temperature resolution is the capacity of the sensor to detect small changes in the measured temperature value. The range of the sensor is the maximum length of sensing fiber that can be measured, considering the attenuation that the signal will experience as it propagates inside the fiber. Finally, the measurement time is the time taken by the system to acquire the readings for all points to provide the temperature profile along the fiber.

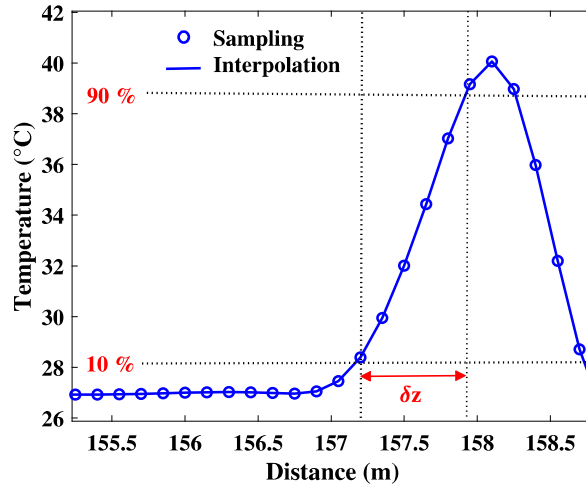


Figure 2.3: Definition of spatial resolution for Raman distributed temperature sensors.

In this outlook, since the first RDTS system was developed in 1985 [74], many approaches have been presented to address the challenges of applying Raman scattering as a temperature sensing mechanism. Most efforts have been put into improving the spatial resolution [100–104], the accuracy [105–110], and the range [111–115] of such sensors. In the sequence, we discuss in more detail some of these approaches.

Initially, we can highlight the study carried out by Bazzo et al. in which a signal processing technique was applied specifically to improve the spatial resolution of RDTS equipment with the objective of identifying temperature variations in regions smaller than 1 m. The algorithm used was based on the principle that signals with excessive and possibly erroneous details have a high total variation. Consequently, the reduction of the total signal variation tends to be a close match of the original signal, as it removes unwanted signal information while preserving important details such as edges. Thus, the regularization by total variation enables preserving edges while smoothing noise in flat regions, even with a low SNR. The main advantage of this proposed method is the ability to correctly reconstruct hot regions on the optical fiber with dimensions up to 15 cm [102].

In the field of temperature safety monitoring, it is very important to quickly locate the position of temperature anomalies and start to alarm. Also, the multimode fiber generally employed in RDTS equipment has a certain temperature hysteresis effect when detecting the surrounding temperature along the sensing fiber, and it deteriorates the warning time of RDTS. Focusing attention on this problem, Li et al.

proposed an RDTS with a heat transfer functional model to perceive the surrounding temperature in advance. The experimental results showed that the temperature change rate of multimode fiber and the surrounding temperature difference holds a linear relationship after fitting. And this fitting relationship was employed to perceive the surrounding temperature anomalies along the multimode fiber for the RDTS system. The experimental results also indicated that the warning-time of RDTS can be optimized from 23.4 s to 1.3 s at the temperature condition with 60°C. Since this heat transfer function model can quickly perceive the environment temperature anomalies, this approach can be a promising tool to be applied in the temperature safety monitoring with high requirements for early-warning time, such as fire monitoring, power cable safety monitoring, and gas pipeline leakage detection [109].

Vo et al demonstrated a sub-centimeter spatial resolution RDTS with enhanced measurement accuracy and reduced acquisition time. When using in this approach a chalcogenide fiber for temperature monitoring, the sensor performance was significantly improved by exploiting the high Raman gain coefficient (4.4×10^{-12} m/W) that is two orders of magnitude higher than that of a silica fiber [116]. A temperature uncertainty of $\pm 0.65^\circ\text{C}$ was achieved for a short measurement time of only 5 seconds; whilst the detection uncertainty was less than $\pm 0.2^\circ\text{C}$ for a longer integration time of 2 minutes. This study also investigated the optimum Stokes and anti-Stokes spectral bands for optimal sensing performance. Besides, theoretical analyzes further showed that a small detuning frequency regime from a pump is more suitable for rapid measurements while a large detuning regime provides higher temperature resolution [105].

In terms of improving the range of these sensors, we can highlight the study carried out by Liu et al. that designed and fabricated a graded-index few-mode fiber with a large effective mode area and low intermodal dispersion for RDTS equipment to simultaneously achieve high spatial and temperature resolution over a long distance [113]. In the experiment, the spatial and temperature resolution of the RDTS was measured using different types of fibers under different launch conditions based on a commercially available RDTS system. By using the graded-index few-mode fiber under the overfilled launch condition, it was achieved at 1°C temperature resolution with a spatial resolution of 1.13 m at the distance of 25 km. The spatial resolution utilizing the standard multi-mode optical fiber degraded to 2.58 m with only 0.3°C higher temperature resolution in comparison. Moreover, the

RDTS using the graded-index few-mode fiber under the quasi-single mode operation condition achieved a temperature resolution of 4.7°C at a distance of 25 km with a 2.2°C improvement and no degradation on spatial resolution compared with that using the standard single-mode optical fiber [113].

A long-range fast-measurement RDTS with a meter spatial resolution exploiting a quasi-periodic pulse-coding technique was introduced by Soto et al. In this study was experimentally demonstrated the feasibility of temperature sensing over 26 km standard single-mode fiber with 1 m spatial resolution reaching 3°C of temperature resolution within 30 s of measurement time. Experimental results employing 1023-bits codewords were also investigated, revealing a range enhancement over 58 km distance with 2 m spatial resolution and 4°C of temperature resolution within 5 min measurement time [112].

In spite of this remarkable progress in the last 10 years, solutions are still lacking to enable these sensors to be employed to monitor small temperature events over regions of a few centimeters with hundreds of meters (or kilometers) of operating range. The main challenge in these cases is not only to detect these small events but also to measure them with reasonable accuracy. To concentrate attention on this problem we propose and experimentally demonstrate in this chapter an image processing technique applied to the temperature profiles generated by the RDTs that will enable achieve reliable temperature measurements over regions of short spatial dimension.

2.3 Developed model

2.3.1 1D to 2D data reconstruction

RDTS systems generate data in only 1 dimension (1D). These data are formed by temperature profiles $T(z_q)$, also known as temperature traces, where $z_q : q = 1, \dots, k$ is the position vector in the fiber optic cable. To best take advantage of signal processing techniques, we initially created a second variable t (time) by considering successive sequential measurements throughout the acquisition of the temperature profiles described in section 2.4. After that, a 2D reconstruction is performed by stacking the temperature profiles in sequence. An image is then created, from which each pair (t, z) of time t and position z is associated with one pixel (x, y) of the image, where x and y are the spatial coordinates of the image. This image can be

represented by a two-variable function $f(x, y) = T(t, z)$ with values referring to a 1D space. With this 2D representation, we can evaluate the temporal behavior of hot spots (looking for persistent hot spots) at the same location.

2.3.2 Thresholding-based image segmentation

The next step is to find the hot spots on the temperature image. To this end, we look for abrupt discontinuities in pixel values, which typically indicate edges. The values of edges delimit regions on the image where there are rapid changes in temperature, thus detecting hot spots. That is, the size of each hot spot is determined by the difference on the spatial axis between the start and the end of the edges detected on the thermal image. To accomplish this, we apply image segmentation [117–121] on 2D temperature maps. Specifically, in thermal images, the intensity levels of pixels belonging to the hot spots are substantially different from the intensity levels of the pixels belonging to the ambient temperature (background). In this way, segmentation using threshold becomes a simple but effective approach to segmenting these images and has therefore been adopted here [122].

Thresholding-based segmentation is an approach widely applied in several cases of image processing, for instance, in medicine to improve the clinical diagnosis of ultrasound images [123], in environmental conservation by detecting oil stains from ships in motion employing radar images [124] and in robotics to detect gesture movements [125]. To segment the thermal image I formed from the temperature profiles, we adopt the thresholding approach, in which the pixel values above the threshold ϵ are considered hot spots and below, the ambient temperature. Initially, each temperature profile that integrates the thermal image was normalized between 0 and 1. This normalization operation is given mathematically by:

$$T(z_k)_{norm} = \frac{T(z_k) - \min(T(z_q))}{\max(T(z_q)) - \min(T(z_q))}. \quad (2.6)$$

After this normalization operation, here denoted by *norm*, the segmentation of the temperature maps is performed by considering:

$$S = 1, \text{ if } I(t, z_k)_{norm} \geq \epsilon, \text{ or } 0, \text{ otherwise.} \quad (2.7)$$

Where S is a binary image resulting from segmentation. For the segmentation to work properly, the ϵ value must satisfy the following requirement:

$$\max \left(\left| \frac{\Delta (T(z_q)_{norm})}{\Delta z} \right| \right) < \epsilon \leq \max (T(z_{k=r})_{norm}). \quad (2.8)$$

The inequality on the left side ensures that the value of ϵ is greater than the noise level in the temperature profile $T(z)$, and the inequality on the right side implies that ϵ must be less than or equal to the maximum temperature in position $z_{k=r}$. This $z_{k=r}$ is the position of the smallest hot spot in the fiber of size d . In this way, the aforementioned last condition ensures that hot spots of sizes up to d are detected. Moreover, the noise level, and therefore the threshold value, will vary depending on the configurations of RDTS equipment used, such as its range. In our study, we have calculated the noise level from the left inequality in equation 2.8. However, other approaches to calculate the noise level could also have been used [126–128]. Furthermore, the threshold value must be measured during the standard sensor calibration routine. After calibration, the threshold value can be used throughout the operation of the sensor equipment. It is important to highlight here that if there is no hot spot identified by the segmentation of images, no action will be taken since the processing is performed only on the detected hot spots.

2.3.3 Measured temperature correction

It is well known that significant errors in temperature measurements can occur if the hot spot in an RDTS is smaller than the equipment's spatial resolution [7]. This is highlighted in Figure 2.4 where the temperature profile obtained from an RDTS with spatial resolution equal to 1 m, for hot spots of 1 m, 50 cm, 30 cm, 15 cm, 10 cm, and 5 cm is shown. It is important to emphasize that these errors persist even after applying the equipment's internal calibration routine, which is a limitation of the equipment itself.

Furthermore, we have measured the temperature error (which we will denote by e_T) of the RDTS equipment as a function of the hot spot (estimated throughout of the temperature map segmentation). These experimental observations are illustrated in Figure 2.5 and show that there is a well-defined relationship between the e_T and the size of the hot spot. In this way, it suggests that knowing the size of the measured hot spot, we can determine what is the associated error e_T and thus

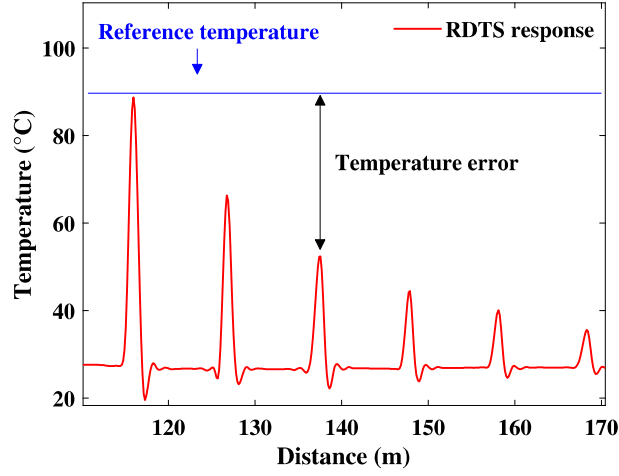


Figure 2.4: The response of an RDTs to square hot spots of varying width. From left to right the hot spots are 1 m, 50 cm, 30 cm, 15 cm, 10 cm, and 5 cm long. The blue horizontal line is the reference temperature.

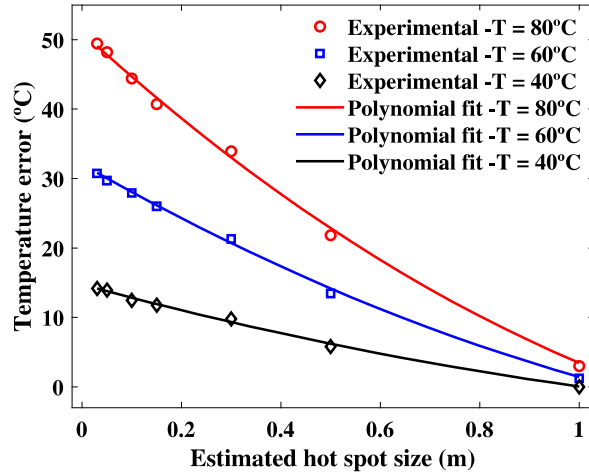


Figure 2.5: Temperature measurement error of the RDTs equipment as a function of the hot spot size for temperatures of the 80°C, 60°C and 40°C. All polynomial fittings were degree 2.

correct it. This can be done through a polynomial function that relates these two quantities as follows:

$$e_T = a_n D^n + a_{n-1} D^{n-1} + \dots + a_0 D^0 = \sum_{j=0}^n a_j D^j, \quad (2.9)$$

in which n is a non-negative integer and the constants $a_0, a_1, \dots, a_{n-1}, a_n$ are the coefficients of the polynomial function. While D is the size of the hot spot. The

value of n is chosen so that D has zero mean and scales it to have unit standard deviation. The D value is obtained by determining the start and the end of each hot spot along with the fiber detected during the temperature map segmentation step. As illustrated in Figure 2.6, the image segmentation allows to determine precisely the size of the hot spots less than a constant of value -1.

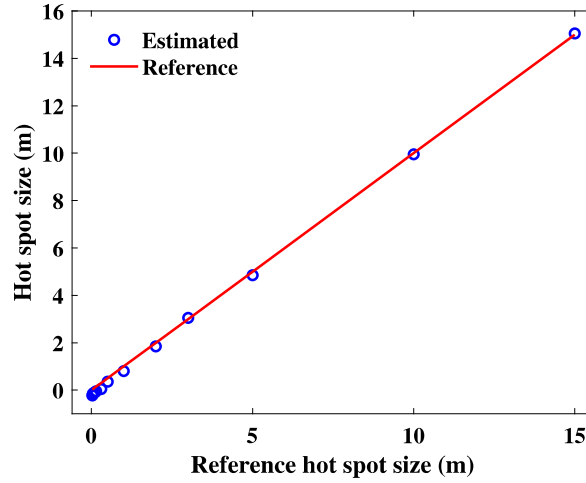


Figure 2.6: Calculation of the hot spot size by thresholding-based image segmentation for an RDTS experimental response to square hot spots of varying width.

Some important considerations need to be made here. Initially, we can see in Figure 2.5 that when the hot spot size is 1 m (equal to the spatial resolution of the equipment used), a single polynomial function (calibration curve) is sufficient to correct the measured temperature. However, when temperature events are less than the spatial resolution of the sensor, more than one calibration curve is required. These calibration curves can be obtained by varying the temperature throughout the equipment calibration step, and each of these will be valid for a specific equipment's operating range. In general, the temperature value measured by the RDTS equipment is always less than or equal to the true temperature value, so that its correction is made by adding to this the error given by equation 2.9. Besides, we stress here that all the considerations addressed in this section are based on the analysis conducted on the experimental data collected (see section 2.4) in this study.

2.4 Temperature data acquisition

To validate our approach, we performed temperature measurements over 200 m of a fiber optic cable using a commercial RDTS model AP Sensing N4385B. A multimode step-index fiber with 50 μm core diameter and 125 μm cladding diameter was used here. The RDTS unit employed in the experiments has been configured to deliver temperature measurements with 1 meter spatial resolution, 1 minute acquisition time, 15 cm spatial sampling interval and temperature resolution of 0.04°C. The experiments were conducted to generate different temperature profiles over fiber length and time simultaneously. Each of these experiments lasted 100 minutes. A special stainless steel cover was designed and fixed over the thermal bath to provide better thermal insulation between the inside of the thermal bath and the external environment. One small aperture in its center allows the optical fiber to pass through the cover. Furthermore, the ambient temperature was controlled at 22°C. Our experimental setup is depicted in Figure 2.7.

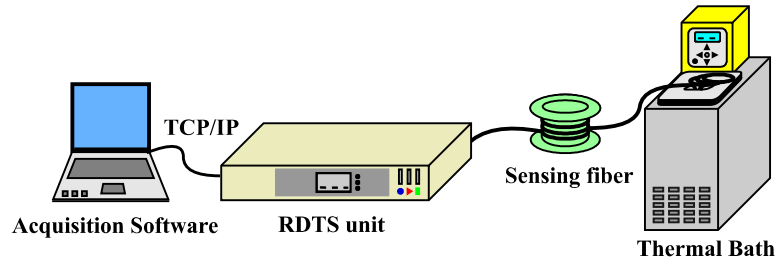


Figure 2.7: Experimental setup for temperature data acquisition.

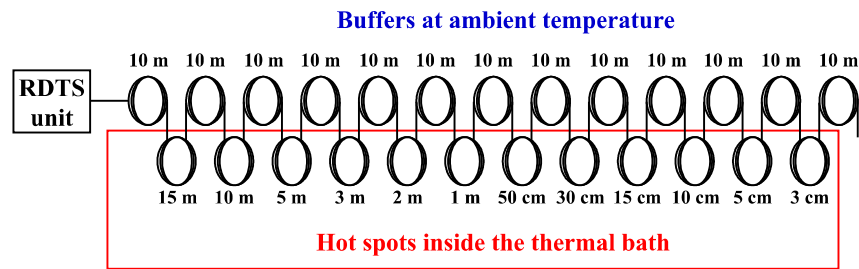


Figure 2.8: Unfolded fiber arrangement inside and outside the thermal bath.

The procedure for generating the temperature profiles was to heat different lengths of fiber by simultaneously putting them inside of a thermal bath model LAUDA ECO RE415G, with an operating temperature range of -25°C to 100°C, stability of $\pm 0.02^\circ\text{C}$, and total volume of 3.3 L. The same fiber cable went in and

out of the thermal bath several times, as illustrated in Figure 2.8. This arrangement allowed the generation of 12 hot spots with sizes of 15 m, 10 m, 5 m, 3 m, 2 m, 1 m, 50 cm, 30 cm, 15 cm, 10 cm, 5 cm, and 3 cm. The temperature throughout the sensing fiber was measured by the RDTS unit and later sent to the acquisition software for visualization.

2.5 Results and discussion

In this section, we present our analysis of the temperature maps built from the temperature profiles measured by the RDTS equipment after applying the processing proposed in section 2.3. For a better presentation of the results, this section is divided into two subsections denominated scenario one and scenario two. Each of them consists of the analysis of different data collected by the RDTS equipment. The distinction between these data is in the temporal evolution of the temperature, which is different in each case. That is, the temperature of the thermal bath was varied as the RDTS equipment collected the data. In scenario 1, the temperature was reduced from 90°C to 25°C, generating a temperature profile over time, as shown in Figure 2.11. And in scenario 2 the temperature was alternated between temperatures of 60°C and 30°C as shown in Figure 2.14.

2.5.1 Scenario one

Figure 2.9 shows the raw thermal image formed from a set of temperature profiles obtained from different temperature and time values. For a better visual perception of the data, a cool scale is chosen where pixels with darker tones represent distance-time pairs having a higher temperature. The lines represent the hot spots along the sensing fiber. Their sizes are of 15 m, 10 m, 5 m, 3 m, 2 m, 1 m, 50 cm, 30 cm, 15 cm, 10 cm, 5 cm, and 3 cm starting from the widest to the narrowest one. The black triangle in Figure 2.9 shows a region of small temperature events. These events are characterized by small temperature variations over regions of a short spatial dimension, where the hot spots are not detectable. This is because the size of the hot spots are much lower than the equipment's resolution.

To make these hot spots detectable, we apply the methodology presented in section 2.3. Initially, we segment the thermal image employing the thresholding method which allows us to locate hot spots and measure their sizes. For each hot

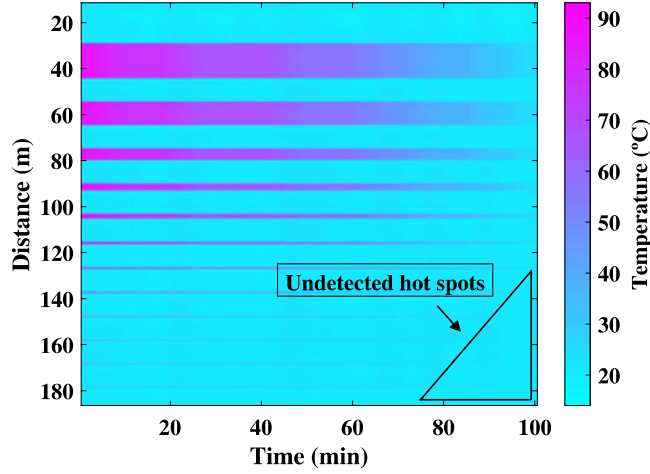


Figure 2.9: Two-dimensional temperature raw map formed from top view of the measured temperature profiles as a function of time and distance.

spot detected by the segmentation, we can associate it with an error value in the temperature measurement given by equation 2.9 that depends on its spatial size. In this way, whenever there is a detected temperature event, we initially estimate its spatial size and with this information, we correct its associated temperature employing the polynomial fitting functions described by equation 2.9. As described in section 2.3, when the temperature event is less than the spatial resolution of the sensor, more than one calibration curve is needed to accurately correct the measured temperature. Here we have generated 10 calibration curves calculated by equation 2.9 in which each one was obtained at a different temperature. In this perspective, the temperature in each region of the temperature map is corrected by dynamically seeking the calibration curve whose calibration temperature is closest to the measured temperature.

Moreover, we have adopted a time window of 100 min merely to demonstrate the viability of the method introduced in this study. However, time windows of varying sizes, as well as the sensor range (which will produce temperature maps of different sizes) can be changed depending on the application. In circumstances that require a rapid response (about few seconds) from the RDTS equipment, time windows of the order of a few minutes can be considered in which a small number of temperature profiles are employed to build the thermal image. It is also important to point out that the size of the time observation window can be larger than the size of the time processing window in order to better visualize the spatial and temporal evolution of

the detected temperature events.

The temperature map after applying the proposed image processing is depicted in Figure 2.10, in which temperature variations of 2.78°C can now be correctly detected over regions smaller than the RDTS equipment's spatial resolution. Moreover, Figure 2.11 shows in greater detail the temperature correction over time for a hot spot whose size is 50 cm located at position 126 m on the sensing fiber (see the seventh horizontal line going from top to bottom of the Figure 2.10). In this case, the solution agrees quite well with the temperature reference value.

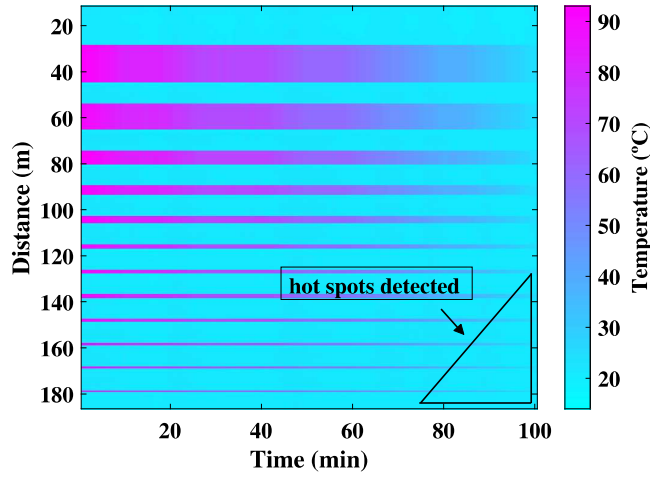


Figure 2.10: Two-dimensional temperature processed map formed from top view of the measured temperature profiles as a function of time and distance.

Furthermore, it is very important to highlight that by applying equation 2.8 for the temperature map we obtained a set of ϵ values, such that $0.15 < \epsilon \leq 0.17$. Here, the value of ϵ inside theses limits was selected by taking the mean value, i.e. $\epsilon = 0.16$. This fixed value of ϵ proved to be adequate to segment all the thermal images evaluated in this study. However, other cases with more complex temperature distributions may require that ϵ be calculated dynamically over time as long as it meets the condition given in 2.8.

2.5.2 Scenario two

To confirm the generic validity of our model, we apply the same calibration functions generated to correct the thermal image in Figure 2.9 to a new thermal image whose temperature profile is different. In this case illustrated in Figure 2.12, when the acquisition of the temperature profiles reaches 40 min and 80 min, the temperature

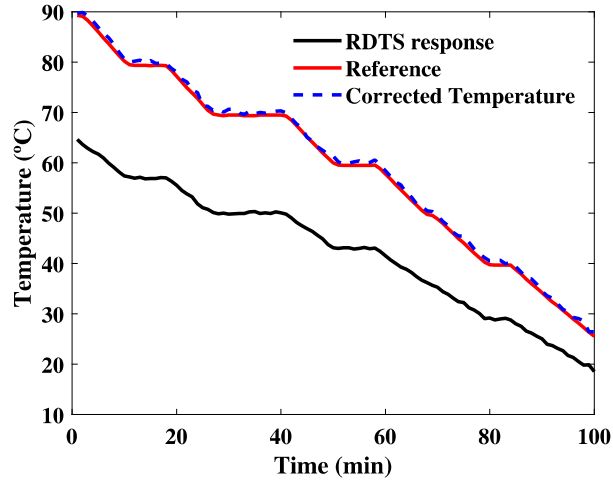


Figure 2.11: Temporal evolution of temperature over the 50 cm hot spot located at position 126 m on the sensing fiber.

is 28.7°C and 30.6°C , respectively. In these two moments, hot spots below 1 m are not detectable because the temperature variation is very small. Figure 2.13 shows that our model once again not only detects these small hot spots but also corrects them simultaneously.

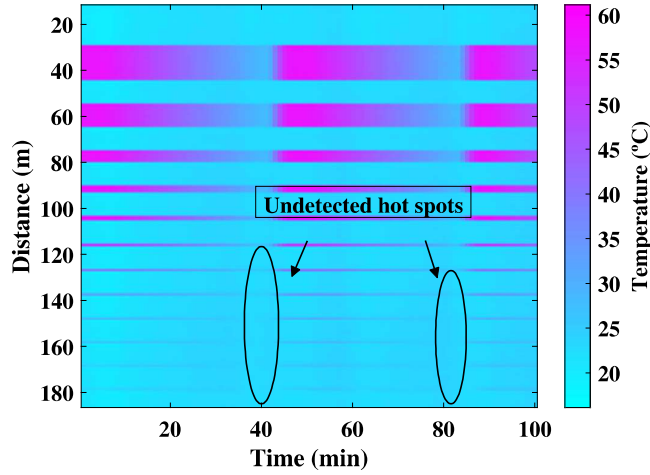


Figure 2.12: Two-dimensional temperature raw map formed from top view of the measured temperature profiles as a function of time and distance.

Figure 2.14 display the same temporal analysis presented in Figure 2.11 now for the temperature map of Figure 2.12 for a hot spot of 50 cm. This result shows more clearly that our approach agrees very well with the reference temperature even for data that was not used throughout the calibration step. To quantify the error

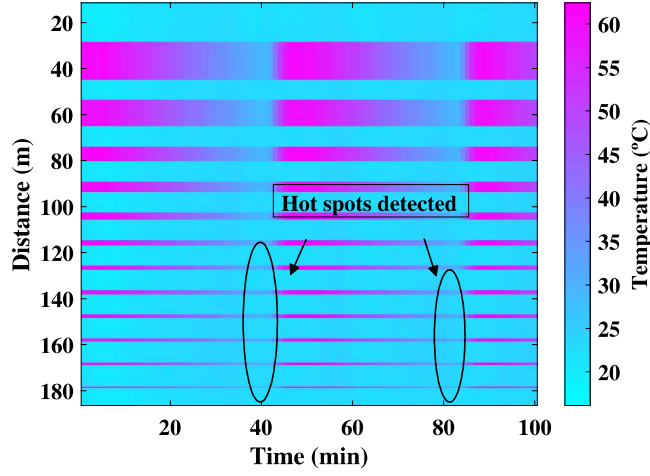


Figure 2.13: Two-dimensional temperature processed map formed from top view of the measured temperature profiles as a function of time and distance.

of our approach, we have calculated the absolute accuracy (uncertainty) taken as the standard deviation of the difference between the reference temperature and the temperature corrected by our model. And we obtain a value of 1.44°C for the hot spot of 50 cm.

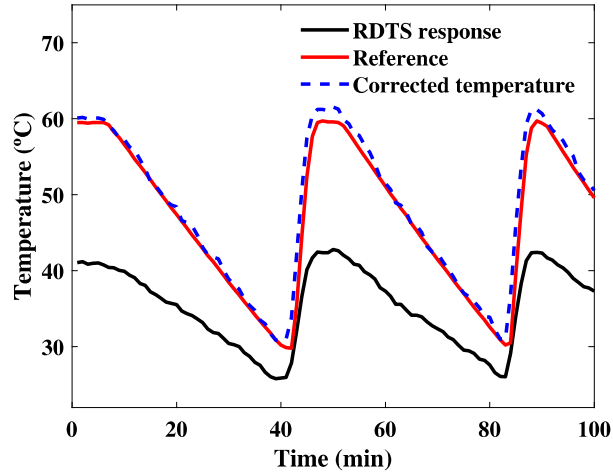


Figure 2.14: Temporal evolution of temperature over the 50 cm hot spot located at position 126 m on the sensing fiber.

To conclude, Figure 2.15 displays the spatial evolution of a single temperature profile along with the fiber, corresponding to the acquisition time of 50 min. We can see here in more detail on how the proposed approach allows us to correct each hot spot. Although all hot spots have the same temperature, a more realistic

situation with a complex temperature distribution in which the hot spots do not have the same temperature, or even change their position, shape and spatial size can also be considered by adopting a multi-level thresholding-based image segmentation [129]. It is already expected to be carried out as future development of this study. Furthermore, a slight fluctuation between the hot spots top can be observed due to errors introduced by the polynomial fitting given by 2.9. Despite this, a significant correction in the temperature measurement is achieved mainly for hot spots smaller than the equipment's spatial resolution.

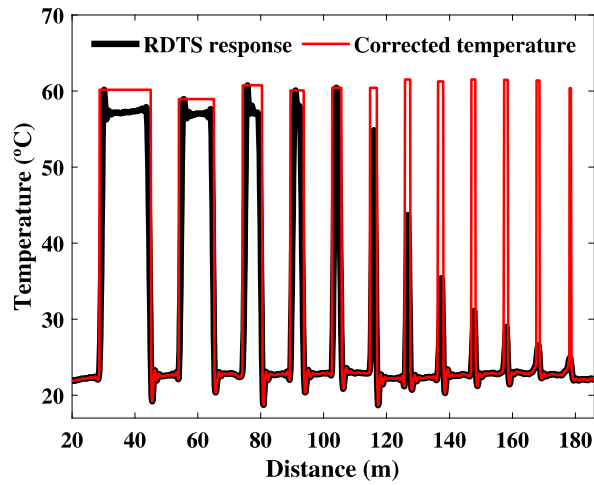


Figure 2.15: Spatial evolution of temperature trace at a specific time of acquisition. The reference temperature at the hot spots tops was 60°C.

Chapter 3

Analytical investigation for RDTS receivers

3.1 Overview

The performance of RDTSs is strongly dependent on the receiver system employed since the signal carrying the temperature information has extremely low intensity. Therefore, a noisy receiver can easily generate noise levels that overlap the signal strength, unable to detect changes in this signal due to temperature variations. The present chapter will address a theoretical analysis based on the sensitivity of the signal of interest with temperature to characterize the receiver under performance requirements. The main contribution of this study is to introduce in the mathematical formalism the term that considers the sensitivity of the signal employed to measure the temperature. This provides a more accurate way of determining how to improve the sensor's accuracy, range, and resolution. Moreover, our analytical model allows us to relate the components specifications of the electronic circuit of the receiver to the detected signal magnitude and the desired performance of the sensor.

3.2 Introduction

Recapitulating briefly the description in chapter 2, the RDTS is an optical fiber sensor technology applied in monitoring large structures such as mining, oil/gas wells, power generation and supply plants, pipelines, power transmission lines, among others [13, 130, 131]. The great differential of these sensors, when compared with point sensors, is that they allow monitoring multiple points along with these structures simultaneously. The RDTS technology employs the optical fiber itself as a sensor element, requiring no transducers along any optical path. Its basic operating principle is to send high-power pulses along the fiber to generate a spread spectrum due to the Raman scattering. The component known as anti-Stokes of this spread spectrum is

temperature-sensitive. Thus, by measuring the amplitude of this signal along with the fiber it is possible to raise the temperature profile throughout the fiber length, of course, respecting a given spatial resolution [13, 130]. A more complete description of RDTS technology can be found in sections 2.2.2 and 2.2.3 of chapter 2 of this thesis.

The main limitation of the temperature interrogation mechanism described above is that the anti-Stokes component presents very low optical intensity, in the order of 100 nW [59]. Therefore, an inadequate receiver can generate comparable or even higher levels of noise that can be added to the signal power level itself, impeding the sensor to properly detect temperature variations. Techniques such as photon counting [132] coherent detection [133], and spread-spectrum techniques [134] have been studied in order to improve the receiver sensitivity.

However, as the receivers present in commercial RDTS equipment, or even those employed in research laboratories, are not ideal to deal with the very low intensity of the anti-Stokes signal that contains the temperature information, the profile (curve or also called a trace) generated by an RDTS is noisy and distorted. In this perspective, the academic research has enabled the progress of RDTS technology through the development and application of signal processing techniques that allow the extraction of temperature information in the best possible way through different approaches. Specifically, most efforts have been put into improving the spatial resolution [100–103, 135], the accuracy [87, 105–110, 136–138], and the range [111–115] of such sensors. In spite of this remarkable progress in the last 10 years, that constitute the current state of the art for this class of distributed optical fiber sensors, such approaches are mostly solutions that do not require any changes at the hardware level, and solutions are still lacking to enable these sensors to have a greater sensitivity. The main challenge in these cases is to properly design a high sensitivity receiver system. In this way, we believe that the development of a dedicated optical receiver to be the most suitable direction to enhance the performance of RDTS technology through hardware investigations.

In this context, this chapter will present an analytical investigation that will direct the design of the RDTS receiving system front end. Such a model is based on the sensitivity of the anti-Stokes signal with the temperature and the desired performance requirements. From this proposed theoretical analysis, it is possible to identify fundamental requirements to improve the sensitivity and performance of the receiver, such as minimum allowable SNR, amplification gain, feedback resistance,

and bandwidth. It is important to emphasize here that the goal of our analytical model is not to provide fixed optimal values of the parameters that make up the front end structure of an RDTS receiver. These values will depend on the requirements of each application. For example, if a particular application requires a distributed temperature sensor with tens of kilometers of range, the spatial resolution is not the main concern in this case. However, for long distances, a high SNR is indispensable. In order to clarify this point, we present in section 3.4.6 of this chapter a case study in which optimal values of the receiver are obtained with our analytical model. This case constitutes a long-distance sensing application in which the requirement is to maximize the range of the RDTS.

3.3 Theoretical background

3.3.1 Basic concepts of optical receivers

The optical receiver is the device that has the greatest importance in RDTS equipment, as it must convert back into electrical form the optical signal generated from the spontaneous Raman scattering that propagated in the sensing fiber, preserving the temperature information contained in the optical signal. Its main component is a photodetector that converts light into electricity through the photoelectric effect. The requirements for a photodetector for RDTSs are similar to those for a photodetector employed in telecommunications systems. That is, it must have high sensitivity, fast response, low noise, and high reliability. Also, its size must be compatible with the size of the fiber core [6].

The underlying mechanism behind the photodetection process is optical absorption. Consider the semiconductor slab displayed schematically in Figure 3.1, each time that a photon is absorbed by the semiconductor an electron-hole pair is generated if the energy of incident photons exceeds the bandgap energy. In this way, under the influence of an electric field set up by an applied voltage, electrons and holes are swept across the semiconductor, resulting in a flow of electric current.

The photocurrent I_p is directly proportional to the incident optical power P_{in} . Therefore, it can be defined as [6]:

$$I_p = \Re P_{in}. \quad (3.1)$$

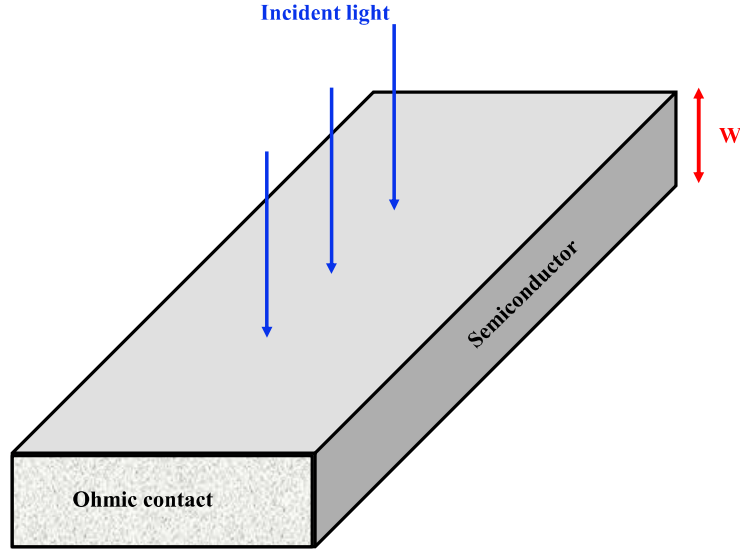


Figure 3.1: Illustration of a semiconductor slab used as a photodetector.

\Re represents the responsivity of the photodetector because more current is produced at a given input power for larger values of \Re . Also, \Re can be defined as [6]:

$$\Re = \frac{\eta q}{hf} \approx \frac{\eta \lambda}{1.24}, \quad (3.2)$$

where η expresses the quantum efficiency defined as [6]:

$$\eta = \frac{I_p/q}{P_{in}/hf}, \quad (3.3)$$

and q , f , and λ are the electron charge ($\sim 1.6 \times 10^{-19} \text{ C}$), the frequency and wavelength of a photon of the incident light, respectively. Also, h is the Planck's constant. The fact that the responsivity of a photodetector increases with the wavelength, as shown in equation 3.2 is because more photons are present for the same optical power. However, this linear relationship with λ is not supposed to continue forever because eventually, the photon energy becomes too small to generate electrons. In semiconductors, this happens for $hf < E_g$, where E_g is the bandgap. The dependence of η on λ enters through the absorption coefficient α . If the facets of the semiconductor slab in Figure 3.1 are assumed to have an antireflection coating, the power transmitted through the slab of width W is [6]:

$$P_{tr} = e^{-\alpha W} P_{in}. \quad (3.4)$$

Also, the absorbed power can be written as:

$$P_{abs} = P_{in} - P_{tr} = [1 - e^{-\alpha W}]P_{in}. \quad (3.5)$$

Since each absorbed photon creates an electron-hole pair, the quantum efficiency η is given by [6]:

$$\eta = \frac{P_{abs}}{P_{in}} = 1 - e^{-\alpha W}. \quad (3.6)$$

In this way, η becomes zero when $\alpha = 0$, and it approaches 1 for $\alpha W > 1$. Another important parameter of a photodetector is its bandwidth B_w determined by the speed with which it responds to variations in the incident optical power. Mathematically, B_w is given by [6]:

$$B_w = [2\pi (\tau_{tr} + \tau_{RC})]^{-1}, \quad (3.7)$$

where τ_{tr} is the transit time and τ_{RC} is the time constant of the circuit. It is important to emphasize here that in equation 3.7, the τ_{tr} is added to τ_{RC} because it takes some time before the carriers are collected after their generation through the absorption of photons. The maximum collection time is just equal to the time an electron takes to traverse the absorption region. On the other hand, τ_{tr} can be reduced by decreasing W . However, according to equation 3.6, the quantum efficiency η starts to decrease significantly for $\alpha W < 3$. In this perspective, there is a trade-off between the bandwidth and the responsivity (speed versus sensitivity) of a photodetector.

In addition to the bandwidth and the responsivity, the dark current of a photodetector is the third major parameter. This dark current is created in a photodetector in the absence of any optical input signal and arises from stray light or from thermally generated electron-hole pairs [6].

3.3.2 Avalanche photodiodes

All detectors demand a certain minimum current to work properly. Also, detectors with a high responsivity are preferred since they require less optical power. When compared to p-i-n photodiodes that have limited responsivity, avalanche photodiodes (APDs) have much larger values of responsivity due to their structure that provides an internal current gain. In this perspective, an APD is the most suitable photodiode

for RDTs given the very low optical power of the anti-Stokes spectral component that holds the temperature information.

The physical phenomenon behind the internal current gain is known as the impact ionization [139]. Under certain conditions, an accelerating electron can acquire sufficient energy to generate a new electron-hole pair. The effect of this impact ionization is that a single primary electron, generated through absorption of a photon creates many secondary electrons and holes, all of which contribute to the photodiode current. Figure 3.2 illustrates an APD structure together with the variation of the electric field in different layers. Under reverse bias, a high electric field exists in the p -type layer sandwiched between i -type and n^+ -type layers. This layer is referred to as the multiplication layer, since secondary electron-hole pairs are produced throughout of impact ionization effect. The i -layer still works as the depletion region in which most of the incident photons are absorbed and primary electron-hole pairs are generated. Electrons produced in the i -region cross the gain region and generate secondary electron-hole pairs responsible for the current gain [6].

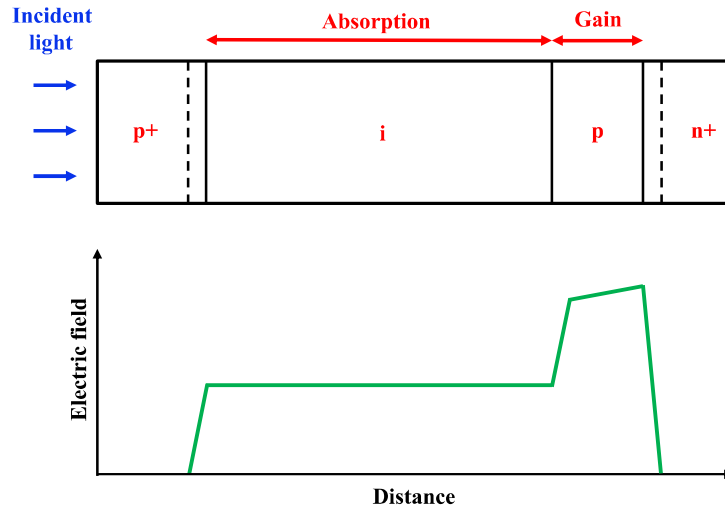


Figure 3.2: Illustration of an APD together with the electric-field distribution inside several layers under reverse bias.

Because of the current gain, the responsivity of an APD is enhanced by the multiplication factor M and is given by [6]:

$$\mathfrak{R}_{APD} = M\mathfrak{R} = M(\eta q/hf). \quad (3.8)$$

It is important to emphasize here that the avalanche process in APDs is intrinsically noisy so that there is a fluctuation in the value of M and therefore its average value is considered in equation 3.8. Besides, in APDs, the transit time t_{tr} increases considerably because the generation and collection of secondary electron-hole pairs take additional time. Consequently, this increase in transit time reduces the gain of APD at high frequencies. This fact gives rise to a trade-off between the APD gain and the bandwidth (speed versus sensitivity).

Silicon APDs provide greater performance in the spectral region around $0.8 \mu\text{m}$. For example, reach-through APDs can provide high gain ($M \sim 100$) with low noise and relatively large bandwidth. On the other hand, for devices operating in the wavelength range $1.3\text{-}1.6 \mu\text{m}$, germanium or indium gallium arsenide APDs must be employed [6]. In this spectral region, APDs have low gain ($M \sim 10$) and reduced bandwidth. This gain-bandwidth limitation of Indium gallium arsenide APDs results primarily from using the indium phosphide material system for the generation of secondary electron-hole pairs [6].

The performance of indium gallium arsenide APDs can be improved through suitable design modifications to the basic APD structure, and several approaches have been developed to address this issue. For example, Nakata et al. developed a separate absorption and multiplication APD with the thinnest reported indium aluminium arsenide multiplication layer of $0.1 \mu\text{m}$ and achieved a gain-bandwidth product of 140 GHz [140]. Also, Watanabe et al. proposed an APD with superlattice planar-structure for 10-Gb/s optical receivers [141].

The thickness of the absorption layer of the APDs affects the transit time considerably. With a thickness of about $1 \mu\text{m}$, most APDs have a quantum efficiency slightly greater than 50%. Focusing on this problem, two approaches have been developed. One consists of a resonant cavity that improves the absorption within a thin layer through multiple round trips. An external quantum efficiency of $\sim 70\%$ and a gain-bandwidth product of 270 GHz were achieved employing a 60-nm -thick absorbing layer with a 200-nm -thick multiplication layer [142]. Another approach, an optical waveguide is used into which the incident light is edge coupled [143].

3.4 Analytical model and simulation analysis

3.4.1 Receiver structure

The analysis performed here is focused on the front end of the receiver, composed of a photodetector and a pre-amplifier. The design of the front end considers a trade-off between the RDTS performance criteria, such as range, spatial resolution, and accuracy. The configuration displayed in Figure 3.3 is a transimpedance, adopted for providing high sensitivity along with wide bandwidth (without equalization) [5]. In this Figure 3.3, I_p is the primary photocurrent generated in the photodiode (here is an avalanche photodiode (APD)), and R_F is the feedback resistance. Besides, C_T is the total capacitance, which includes the contributions of the photodiode and transistor capacitances. The role of C_T is to properly adjust the response time of the circuit, usually described by the time constant equal to $C_T \times R_F/G$. For instance, the correct selection of C_T allows the pre-amplifier to remain stable even under high frequencies where the time constant must be reduced, and the signal transit time from input to output must be kept below the desired impulse response of the receiver.

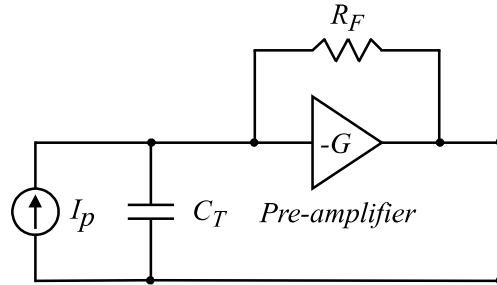


Figure 3.3: Structure for the front end of the optical fiber receiver under analysis. The photodiode is modeled as a current source.

Also, the input voltage to the pre-amplifier can be increased by using a large R_F . Even though R_F is large, the negative feedback reduces the effective input impedance by a factor G . The bandwidth is thus enhanced by a factor of G compared with high-impedance front ends. Specifically, transimpedance front ends are often applied to optical receivers because of their improved characteristics, such as high sensitivity along with wide bandwidth. However, its major design issue is related to the stability of the feedback loop [144, 145].

3.4.2 Characterization of the signal

As described in chapter 2, the characterization of the signal is here denoted by the physical parameter measured (optical intensity of the anti-Stokes signal) that contains the temperature information. The design of the receiver for RDTS should be started by establishing the desired temperature accuracy and spatial resolution values, since noise is added to the signal regardless of the scheme of detection used for this signal. Then, the starting point to this analysis is determining the minimum noise level allowed for a given measured temperature accuracy. The intensity of the anti-Stokes signal can be defined as follows [146]:

$$I_{AS} = P_{p0} n_{AS} \Gamma_{AS} \frac{\exp(-\alpha_{AS} L)}{\alpha_{AS} L} \frac{\sqrt{\sinh^2(\alpha_{AS} L) + \sin^2(\kappa L)}}{\sqrt{1 + (\kappa/\alpha_{AS})^2}}. \quad (3.9)$$

In equation 3.9, P_{p0} refers to the pump signal, κ is the wave number, Γ_{AS} is the capture coefficient, α_{AS} is the attenuation coefficient, and L the total fiber length. The term representing the dependence of the anti-Stokes signal on temperature is given by the distribution of Bose-Einstein [146]:

$$n_{AS} = \frac{\exp(-\Delta E/k_B T(z))}{1 - \exp(-\Delta E/k_B T(z))}. \quad (3.10)$$

Being ΔE the energy difference between a pumping photon and an anti-Stokes photon scattered. k_B is the Boltzmann constant, and $T(z)$ is the temperature along the sensing fiber. In equation 3.10 the temperature must be on the absolute scale. In order to determine the minimum noise level allowed in the system, we started with the sensitivity of the anti-Stokes signal with the temperature, defined as follows [7]:

$$\varepsilon_{AS} = \frac{1}{I_{AS}} \frac{d(I_{AS})}{dT}. \quad (3.11)$$

Figure 3.4 illustrates the sensitivity of the anti-Stokes signal with the temperature from equation 3.11. As an example, by consider $I_{AS} = 100$ nW and $\varepsilon_{AS} = 0.8361$ %/K at room temperature (300 K), the change in the anti-Stokes signal power to a temperature variation of 1 K is $\Delta I_{AS} = 0.836$ nW. This implies that if the noise level is greater than this ΔI_{AS} value, the temperature variation can not be detected, no matter how sensitive the receiving system is. Similarly, the minimum noise level

becomes even lower in applications where it is necessary to detect variations in temperature of tenths of degree, which corresponds to values lower than 8.36 pW for this same intensity of the anti-Stokes signal.

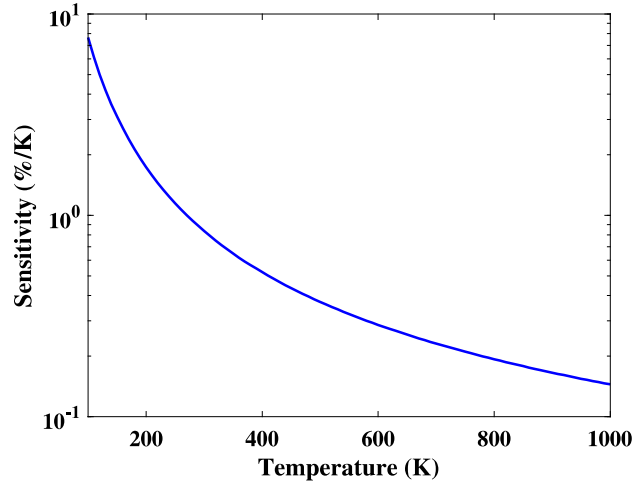


Figure 3.4: Sensitivity of anti-Stokes signal to temperature.

3.4.3 Minimum allowed signal to noise ratio level

The noise levels discussed previously may seem reasonable at a first glance, however, we should not forget that the power level of the signal is also very low. Consequently, the second relevant factor here is SNR. Thus, we can derive from equation 3.11 an expression that provides the minimum SNR allowed to detect a certain temperature variation δT :

$$SNR_{min} = \frac{I_{AS}}{\Delta I_{AS}} = \frac{I_{AS}}{I_{AS} \cdot \varepsilon_{AS} \cdot \delta T} = \frac{1}{\varepsilon_{AS} \cdot \delta T}. \quad (3.12)$$

Figure 3.5 shows therefore from equation 3.12 minimum values of the SNR for the anti-Stokes signal so that a certain accuracy is reached. It is also shown that for values of accuracy lower than 1 K, higher SNR values are required. Nevertheless, according to Figure 3.4 and Figure 3.5, the minimum noise level becomes much lower when high measuring temperatures are involved. Consequently, to monitor regions with high temperatures require a much more sensitive receiver. This is justified since the anti-Stokes signal is generated from the interaction of the photons of the incident light on the fiber and the molecules constituting the medium. Then at high temperatures, the molecular vibrations will be larger, i.e. the molecules will

absorb this thermal energy, moving to higher energy states. Therefore, the term ΔE in equation 3.10 is increased, resulting in a reduction of the sensitivity of the anti-Stokes signal with temperature. Here two considerations are important. First, let's define δT as the accuracy of the sensor. Secondly, generally before tracing the temperature profile, the anti-Stokes signal is normalized by another signal (Stokes). However, the latter is three orders of magnitude higher than the first one and its temperature dependence can be neglected. This makes it unnecessary to consider it in this approach.

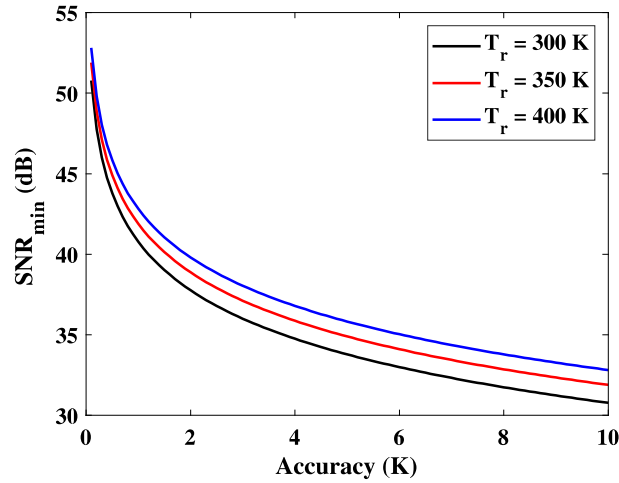


Figure 3.5: Minimum value of signal to noise ratio as a function of accuracy for different room temperatures (T_r) of 300 K, 350 K, and 400 K.

Also, the sensitivity of the receiver is described as the minimum detectable optical power, which is the optical power required to produce a photocurrent of the same magnitude of the noise, i.e. an $\text{SNR} = 1$. Consequently, in the equation 3.12 when the SNR is 1, and $I = 8.36$ pW (equivalent to the minimum level of noise allowed to obtain an accuracy of 0.1 K), provides us that in order to attain such accuracy, the sensitivity of the receiver must be equal to -80.77 dBm.

3.4.4 Amplification gain

To achieve an SNR higher than 40 dB as shown in Figure 3.5, it is necessary to amplify the anti-Stokes signal without adding high noise levels. An APD is adequate in this task because it allows detecting anti-Stokes optical powers as low as tenths

of nW and amplify it by a multiplication gain factor M . The relation between the SNR and the M is defined by [6]:

$$SNR = \frac{I_{AS} \cdot R_F \cdot \mathfrak{R} \cdot M}{\sqrt{[2q(I_{du} + (I_{dm} + I_{AS,r} \cdot R_F)M^2 \cdot F + i_n^2)] B_w}}. \quad (3.13)$$

In equation 3.13, R_F is the feedback resistance, \mathfrak{R} is the responsivity of the detector, q is the electron charge ($\sim 1.6 \times 10^{-19}$ C), I_{du} corresponds the leakage current, I_{dm} is the part of the dark current of the photodiode multiplied with the signal in the APD, $I_{AS,r}$ is the power of the anti-Stokes signal reaching the APD, F is the excess noise factor originated from the gain variability M , i_n^2 is the noise current spectral density, and B_w is the bandwidth of the receiver. Making the term $\sqrt{2q(I_{du} + (I_{dm} + I_{AS,r} \cdot R_F)M^2 \cdot F + i_n^2)}$ which represents the total noise in the receiver equal ΔI_{AS} , $SNR = SNR_{min}$, and rewriting in terms of M we obtain the following expression for the gain by amplification that considers the sensitivity of the anti-Stokes signal with the temperature:

$$M = \frac{SNR_{min} \cdot \varepsilon_{AS} \cdot \delta T \sqrt{B_w}}{R_F \cdot \mathfrak{R}}. \quad (3.14)$$

From the equations 3.9 and 3.14, and considering $L = 20$ km, $B_w = 100$ MHz, $R_F = 100$ k Ω , $\mathfrak{R} = 1$ A/W [147], the behavior of the gain M as a function of the desired accuracy can be obtained, as shown in Figure 3.6. From this figure, the limits to measure the temperature and the accuracy can be discussed. For a $\delta T = 1$ K, the M is required to be 11.19, which is reached by most commercially available APDs. However, a $\delta T = 0.5$ K requires an $M = 22.39$. It seems intuitive to increase the gain by multiplying the APD to obtain a better performance, however, this increases the value of I_{dm} and consequently the total noise. It is important to note that the anti-Stokes signal power drops as it propagates in the fiber, which implies that even high values of M will not be strong enough to overcome the degradation of SNR with the distance, as displayed in Figure 3.7.

Figure 3.7 shows that there is a value of the APD gain that maximizes the SNR in each curve. Consequently, one can determine the gain evolution as shown in Figure 3.8. The optimum values of M must be less than 11.7 for this case analyzed here. Moreover, the value of the B_w may move this optimum value of M (denoted by M_{opt}), further limiting the sensor range. Therefore, is possible to find the optimum

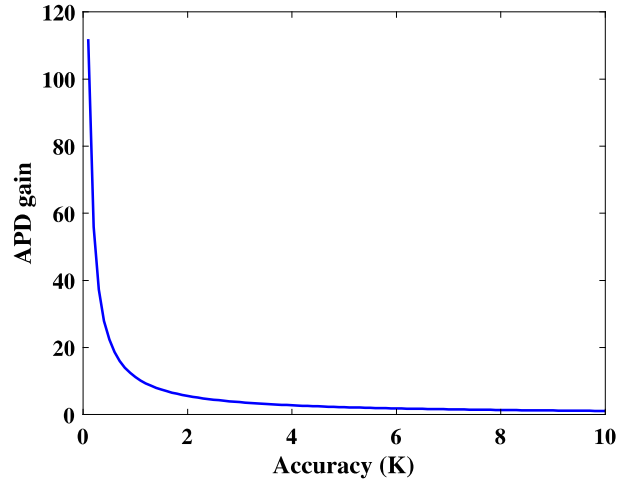


Figure 3.6: Gain of multiplication of the APD as a function of sensor accuracy considering the values of SNR_{min} .

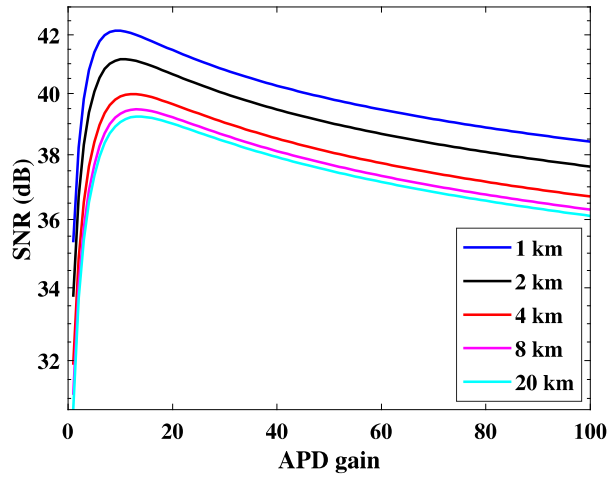


Figure 3.7: SNR versus APD gain for different sensor lengths.

value of B_w , denoted by $B_{w_{opt}}$, that maximizes the range of the sensor, as shown in the equation 3.15:

$$B_{w_{opt}} = M_{opt}(\operatorname{argmax}(L)). \quad (3.15)$$

The expression “arg max” represents the pair (or pairs) $(L, B_{w_{opt}})$ that maximizes the value of the objective function M_{opt} . From Figure 3.9, we conclude that high B_w values (above 24.44 MHz in this case) reduce the sensor range abruptly, this is due to the reduction of the SNR and by the multiplication of the noise along with

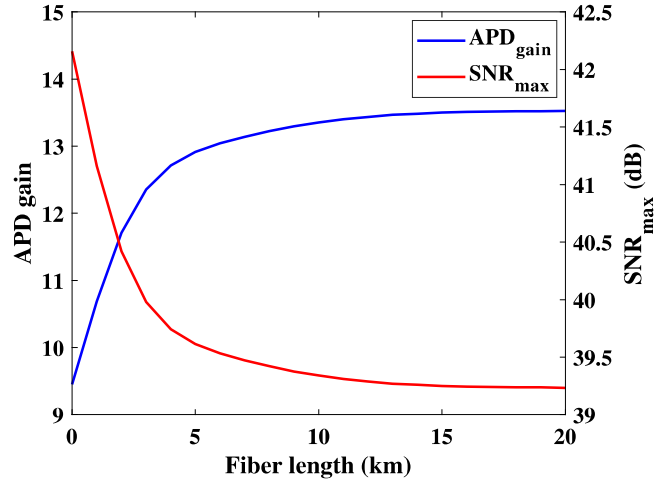


Figure 3.8: To the left: Optimum APD gain as a function of sensor length. On the right: Maximum SNR obtained for a given gain as a function of the sensor length.

the signal in the APD. Table 3.1 summarizes some values of B_w and how they affect the sensor range and the spatial resolution for a given M_{opt} .

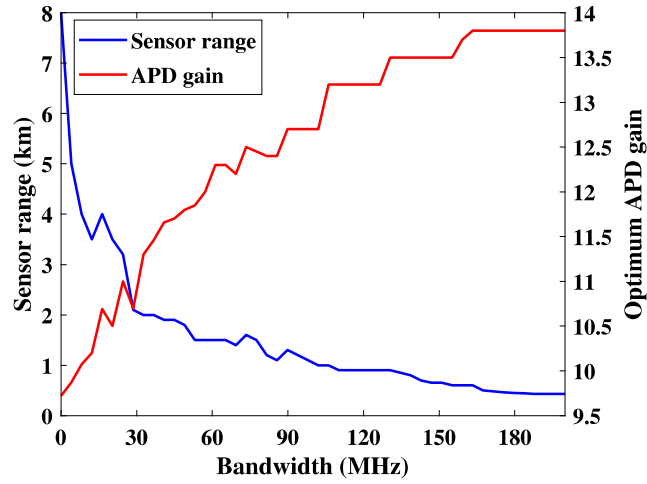


Figure 3.9: To the left: Optimum sensor range as a function of receiver bandwidth for a given optimum gain value. On the right: Optimum APD gain.

At this point, the receiver's design begins to gain more complexity, because trade-offs arise in choosing the parameters. For example, B_w affects not only the sensor's range but also its spatial resolution δz (see equation 2.5 in chapter 2). Given this trade-off, an alternative is to set the value of B_w , thus maintaining acceptable

Table 3.1: Receiver bandwidth trade-off

Bandwidth	APD gain	Sensor range	Spatial resolution
102 MHz	12.7	1.0 km	1.0 m
73.5 MHz	12.5	1.5 km	1.4 m
50.0 MHz	11.7	1.9 km	2.0 m
16.3 MHz	10.6	4.0 km	6.3 m
4.08 MHz	9.87	5.0 km	25.3 m

sensor range values and accuracy in temperature measurement, and to look for other approaches that improve the spatial resolution.

3.4.5 Feedback resistance

Besides, we can obtain an ideal value for R_F from equation 3.14, as shown in Figure 3.10. In this figure, we observe that a large R_F reduces the thermal noise and improves the receiver sensitivity. The main drawback of the high-impedance front end is its low B_w [148, 149]. An equalizer is sometimes employed to improve the bandwidth. The equalizer works as a filter that attenuates low-frequency components of the signal more than the high-frequency components, thereby effectively increasing the front-end bandwidth. Specifically, the range of R_F values that provide better stability is 10 k Ω - 100 k Ω , according to parameter values used in our model. However, this may change slightly depending on the application requirements. Also, this range of values will not only allow the best possible sensitivity to be achieved but will also prevent the sensor from going “blind” during the time it takes for the receiver to come out of saturation caused by an overload [150].

Some important considerations need to be made here. Initially, the strong reflections may saturate the receiver that is designed for very low-intensity signals, as is the case here. Besides, in a transimpedance pre-amplifier, an overload occurs when the input current is greater than the maximum voltage output of the pre-amplifier divided by R_F . When the output voltage of the pre-amplifier reaches its limit and the input current continues to rise, a charge is stored on the input node. After the input current returns to within the normal operating range of the pre-amplifier, the

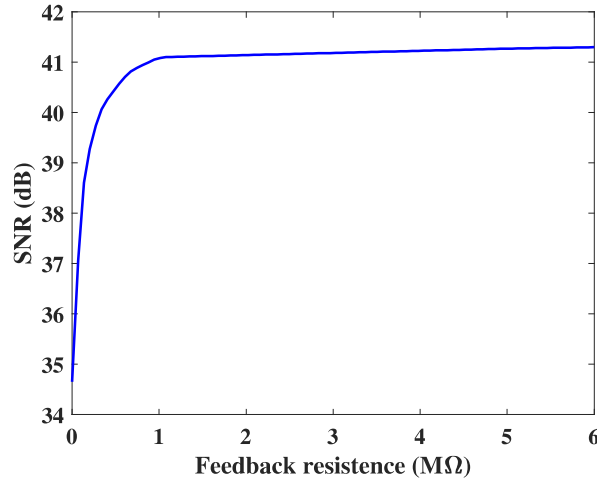


Figure 3.10: Signal to noise ratio as a function of the feedback resistance.

charge is drained away through the feedback resistor. However, for severe overloads, this can take a considerable time. Until the settling time has elapsed, the output of the receiver will be distorted. Avoiding reflections would solve this problem, but this is not always feasible, especially in the event of a fault. Alternatively, we can choose a value of R_F well below that which minimizes the receiver noise, and therefore, balance the ability of the receiver to recover from overload. Modifications to the front end, such as adding a reverse-biased Schottky diode to limit the departure of this node from zero can help accelerate the overload recovery, but they do not eliminate the problem and they add some noise to the receiver. Among the several types of diodes, the Schottky diodes are the most suitable for this purpose since they are significantly faster (rise and fall times of tens of picoseconds with noise equivalent power (NEP) of $\sim 100 \text{ pW Hz}^{-1/2}$ [151]), and their speed is only limited by the junction capacitance. On the other hand, if a great switching speed was not strictly necessary, other diodes could be employed as well.

In full differential and noninverting mode amplifiers, common-mode rejection ratio (CMRR) is of the biggest concern. However, this is not the case here where an inverting voltage transimpedance amplifier is employed. The CMRR can be measured in several ways. In the case of this study, it can be measured as the ratio of the common-mode gain to differential-mode gain. Also, it must be avoided that the amplifier reaches the slew rate limit so that additional delays in the feedback loop do not occur and large signals or spikes at the input generate oscillations in the circuit. Providing an additional negative-feedback path will allow greater control

over the slew rate and consequently better receiver stability [152, 153].

3.4.6 Optimal values for a long-range sensing application

In this section, we present a case study in which optimal values of the receiver are obtained with our analytical model. This case constitutes a long-distance sensing application in which the requirement is to maximize the range of the RDTS. After performing several simulations with our model, we found that a possible configuration of the RDTS receiver parameters that makes it possible to maximize its range is to use $B_w = 10$ MHz, $C_T = 0.1$ pF, $M = 10.7$, $R_F = 100$ k Ω , and $\Re = 1$ A/W [147]. With these values we obtain the following performance of the sensor in terms of its range, as shown in Figure 3.11. Our results reveal that for a 20 km range, an SNR of 43.5 dB can be obtained, with an accuracy as high as 0.6 k and a spatial resolution of 6 m.

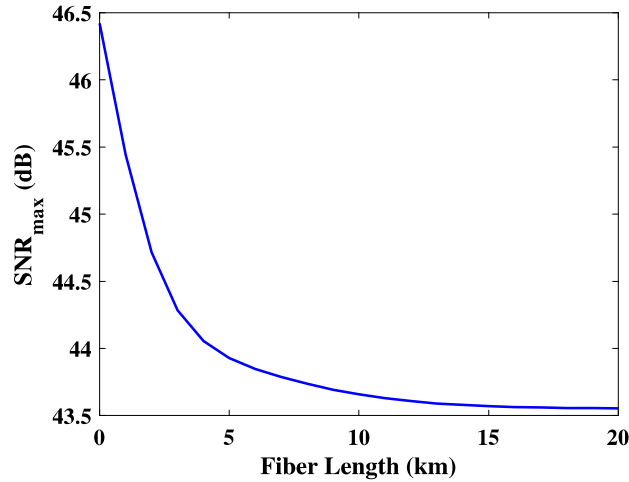


Figure 3.11: Optimal values for a long-range sensing application versus the maximum SNR.

It is important to emphasize here that the goal of our analytical model is not to provide fixed optimal values of the parameters that make up the front end structure of an RDTS receiver. These values will depend on the requirements of each application. Our analytical model allows selecting the specifications of the main components of the electronic circuit of the front end receiver under analysis for different applications that may have distinct operating requirements. Furthermore, a field programmable gate array (FPGA) is a possible alternative for implementing a

robust and reconfigurable computing receiver for an RDTS not only with the high-level computing architecture but also with a low-level hardware integration structure for complex analytics computations. Most importantly, a flexible and easily reconfiguration platform, provides a foundation for similar receivers to be developed for different applications in the sensing industry.

Chapter 4

Linearization technique for interferometric fiber sensors

4.1 Overview

The last two chapters of this thesis were focused on RDTs that are based on the nonlinear Raman scattering effect. Throughout the realization of this Ph.D. research were also studied signal processing techniques for interferometric fiber sensors. These optical sensors are based on the concept of interferometry in which an interference pattern is produced at the sensor output due to the superposition of two or more light waves. Furthermore, the interference spectrum generated by these interferometric sensors has small variations that are not due to a change in the measured physical parameter, but from other sources, which from this point onwards we define as the noise contained in these interference spectra. In this perspective, this chapter describes and experimentally demonstrates a linearization technique for these interferometric fiber sensors with the main objective of reducing this noise to improve the response of these sensors. Specifically, from a 2D reconstruction of the interference spectra and subsequent denoising process, relevant improvements in linearity and range are obtained for both angle and liquid level sensors. This linearization technique can be easily implemented on any graphical interface of different types of interferometric sensors without requiring modification of the physical structure of the sensor. In this regard, this approach finds a wide field of applications since with the appropriate modifications, it can potentially be applied to other non-interferometric sensors that have moderate linearity and operating range.

4.2 Theoretical background

4.2.1 Interferometric fiber sensors

Interferometric fiber sensors are widely employed in the monitoring of various physical parameters such as liquid level [154], temperature [155], vibration [156], acoustic waves [157], gas micro-leakage [158], volatile organic gases detection [159], electric field [160], rotation [161], humidity [162], detection of heavy metal ions [163], pressure [164], magnetic field [165], human vital signs [166], torsion [167], acceleration [168], refractive index [169], among others. These sensors are commonly associated with features, such as low costs, having easy fabrication processes, and being very compact structures in all-fiber setups.

The working principle of an interferometric fiber sensor generally consists of splitting an optical beam into two paths with different phase velocities and then recombining them creating an interference pattern in the output spectrum. This can be achieved in different ways, for instance, by connecting fibers with cores of different diameters [170, 171], using fibers with up-tapers [172], by analyzing the reflected signals from different Bragg gratings [173, 174], producing air cavities within the sensor fiber [175, 176], among other approaches. In this way, the parameters of the environment (e.g. temperature, liquid level, or pressure) can be obtained by analyzing the variations in the interference spectrum.

The interference pattern generated by these interferometric sensors can be mathematically modeled by the superposition of plane electromagnetic waves whose intensity is proportional to the square of the electric field amplitude. Thus, the intensity of interference from a traditional in-fiber Mach-Zehnder interferometer can be given by the equation [177]:

$$I_{MZI} = I_{co} + \sum_m I_{cl,m} + \sum_m 2\sqrt{I_{co}I_{cl,m}} \cos(\phi_m), \quad (4.1)$$

in which I_{co} and $I_{cl,m}$ are the light intensity of the core and cladding modes, respectively. ϕ_m is the relative phase difference between the core and the m th-order cladding modes, that can be given mathematically by the expression [178] (considering air environment after its propagating through the sensor length L):

$$\phi_m = \frac{2\pi}{\lambda_0} \left(n_{eff}^{co} - n_{eff,m}^{cl} \right) L, \quad (4.2)$$

in which n_{eff}^{co} and $n_{eff,m}^{cl}$ are the effective refractive index of the core mode and m th cladding modes, respectively, and λ_0 is the wavelength in vacuum. Therefore, changes over both the sensor length or the environment affect the effective refractive index, leading to the phase modification.

Depending on the type of interrogation mechanism, some problems may arise. For instance, long interferometers whose interrogation is performed by analyzing the wavelength shift of a given peak, usually present smaller free spectral ranges, and for this reason they also present a smaller observation window for analyzing this wavelength variation, which makes the measure unfeasible for larger physical sensors that use this approach [170]. In some cases, for those sensors to achieve high resolution, its operation range has to be significantly reduced so that it can work within its linear response range [179, 180].

Also, interferometric fiber sensors with intensity-based interrogation mechanism are often susceptible to source power variations, fiber loss fluctuations and variations in modal power distribution in fibers which can induce measurement errors [181]. All of these limitations can be minimized if signal processing techniques are applied. Such approaches are inexpensive because they do not require to modify the physical structure of the sensor. And in most cases, easy to implement on any graphical interface.

A number of signal processing-based solutions to improve interferometric fiber sensors performance have already been developed. For example, to compensate source power variations and fiber bending losses, Huang et al. demonstrated a counting signal processing technique for fiber-optic interferometric sensors capable of counting the numbers of the maximum and minimum of the output interferometric signal in a specific time duration, and it can be employed as the foundation to distinguish the sensing phase signal. It can also be applied as a signal detector on applications such as intrusion detection. All sensors are subject to aging of the optical components and bending loss, and therefore the output signal of each sensor may vary with time. These same authors also proposed a counting level normalization technique to compensate for these variations and to obtain the correct counting numbers [182].

For noise suppression Liu et al. demonstrated a novel common-mode noises suppression technique by locking the mean phase value of the sensing interferometer employing a reference interferometer with a 3x2 coupler. Experimental results confirmed that this method can increase the correlation coefficient between the outputs

of sensing and reference interferometers by 6% and reduce its standard deviation by approximately 70% compared to the conventional method. The common-mode noises suppression factor was measured as - 8.49 dB in the frequency range from 300 Hz to 1 kHz, comparing to - 6 dB achieved by the conventional approach of simple subtraction [183].

Reducing and suppressing the random noise and drift error is a critical task in an interferometric fiber-optic gyroscope. Focusing attention on this problem, an enhanced adaptive Kalman filter based on innovation and random-weighting estimation was proposed by Song et al. to denoise interferometric fiber-optic gyroscope signals in both static and dynamic conditions. The covariance matrix of the innovation sequence was determined by applying the random-weighted-average window. The Kalman filter gain was then adaptively updated by the estimated covariance matrix. To minimize the inertia of the Kalman filter response in the dynamic condition, the covariance matrix of process noise was modified when discontinuous signals are detected by the innovation-based chi-square test method. Also, in this investigation, the Allan variance was used to evaluate the denoise performance for static signals. In the dynamic condition, the root-mean-square error was considered as the performance indicator [184].

To improve the sensitivity of the interferometric fiber sensors a signal-processing algorithm based on phase tracking in the frequency domain of optical fiber Fabry-Perot interferometric spectrum was described by Qi et al. This concept was demonstrated with three fiber Fabry-Perot interferometers for relative humidity measurement. Experimental results showed that this approach can yield optical path difference measurement with high resolution, especially in the lower range of absolute humidity under 2000 ppm [185].

Besides, to improve the range of these sensors, Rodríguez et al. introduced a new interrogation technique based on the analysis of the overall spectrum envelope of an in-line Mach-Zehnder interferometer structure with three different fibers. The interference pattern created by a level sensor of 120 mm was evaluated with both the conventional and the proposed interrogation techniques. The experimental results revealed that this technique not only improves the sensitivity of the sensor by more than an order of magnitude, but also allows the length of the in-line Mach-Zehnder interferometer to be extended up to 470 mm while maintaining high linearity and sensitivity [171].

Furthermore, to carry out sophisticated real-time analysis on demodulated signals Griffin et al. developed the digital interferometric sensor interrogation system and its associated software, which enables the user to configure a wide variety of demodulation schemes [186]. A more complete overview of interferometric fiber sensors can be found at [187]. In this outlook, to best take advantage of the signal processing techniques, this chapter proposes an approach based on a 2D reconstruction of the interference pattern generated by this type of optical sensors and their posterior denoising, allowing not only to increase the linearity of its response, but also its region of operation.

4.3 2D denoising linearization

In our proposal, an image is created from the interference pattern, from which each pair (λ, p) of wavelength λ and monitored physical parameter p is then associated with one pixel (x, y) of the image, where x and y are the spatial coordinates of the image. This image can be represented by a two-variable function $f(x, y)$ with values referring to a 1D space. The great advantage of this representation is the possibility of exploring the degree of similitude and redundancy of information between each pair (λ, p) and their respective neighboring pairs in the formed image.

To perform this analysis, the well-known image denoising Non-Local Means (NLM) was employed [188–191]. The choice of this algorithm was based on fact that among many existing noise removal algorithms such as Gauss filtering, total variation, neighborhood filter, Wiener filter (ideal filter), hard translation invariant wavelet thresholding, discrete cosine transform-based filters empirical Wiener filtering, the NLM algorithm is more suitable for removing noise from periodic images and with high redundancy [192], as is the case with our images formed from the stacking of the spectra acquired from the angle and liquid level measures (see e.g. Figure 4.7).

The NLM algorithm is based on the use of sliding neighbourhoods, which correspond to sets of all pixels $j = (x, y)$ that surround a certain pixel at $i = (x', y')$ within a window of a predefined size. In a very general sense inspired by the neighborhood filters, one can define as “neighborhood of a pixel i ” any set of pixels j in the image such that a window around j looks like a window around i . All pixels in that neighborhood can be used for predicting the value at i , as was first shown in

[193] for 2D images. By this, we simply mean that every small window in a natural image has many similar windows in the same image.

The similarity between two pixels i and j is performed by comparing the values $f(i) = f(x', y')$ and $f(j) = f(x, y)$ in the entire neighbourhoods [188, 189]. The degree of similitude and redundancy in the image is evaluated by calculating the Euclidean distance between all values $f(\eta_i)$ and $f(\eta_j)$ within neighbourhoods η_i and η_j . When the Euclidean distance is small, there is a high level of similitude between the η_i and η_j neighborhoods compared, and therefore the highly similar values $f(i)$ and $f(j)$ associated with both pixels i and j can be averaged to reduce noise. To eliminate noise from a pixel i in the image, the value $f(i)$ associated to such a pixel is determined by the following expression [194]:

$$f(i) = \sum_{\forall j \in I} w(i, j) \cdot f(j), \quad (4.3)$$

where I is the entire domain of the image, $f(j)$ corresponds to the value of the image associated to the pixel j and $w(i, j)$ are the weighting factors calculated by:

$$w(i, j) = \frac{1}{Z(i)} e^{\frac{-\|f(\eta_i) - f(\eta_j)\|^2}{\beta^2}}, \quad (4.4)$$

where β is a smoothing control parameter and $Z(i)$ is a normalization factor. Moreover, the weighting factors $w(i, j)$ are independent of the geometry and only depend on the similarity of the data around pixels i and j . The pixels j , with similar surroundings to the pixel i , are associated to a higher weight $w(i, j)$, regardless of the relative (spatial) distance between the two pixels. This feature characterizes this method as non-local.

For the NLM algorithm to work properly, three parameters need to be adjusted. The first one is denominated a smoothing degree. As this value increases, the smoothing in the resulting image increases. This parameter is usually set to ten times the noise standard deviation estimated from the image [192]. The second is the size of the search window. Although the entire image could be used, a sliding temporal window of 3 consecutive measurements is chosen here, so that the search for repeated patterns is only restricted to the area covered by this search window. The last parameter to be defined is the similarity window that must be less than or equal to the size of the search window. The similarity window has been chosen here of size 1x1, corresponding to 1 longitudinal data point.

Concerning the processing time, if we take a similarity window of size P , and a size search window Q , the overall complexity of the NLM algorithm is $N^2 \times P \times Q$, in which N^2 is the number of pixels of the image. For our images formed from the angle and liquid level measurements that have 12000 pixels and 11000 pixels, respectively, the processing time is approximately 25 seconds.

The images to be processed were formed by stacking consecutive interference spectra each corresponding to a single parameter p value measured by a specific sensor, in this case, angle and liquid level. After applying the NLM algorithm on the image formed by the interference spectra, there is a reduction in noise level throughout the image. This type of 2D processing ensures that removing information that will not be used for sensing applies not only to a single spectrum but to a set of them, by correlating them during the denoising, which will later be used to characterize the sensor.

4.4 Experimental data acquisition

4.4.1 Working principle based on interferometry

To evaluate the linearization method proposed here we applied it to a Mach-Zehnder type interferometric fiber sensor that measures angle [195] and to a similar one used to measure liquid level [171]. The working principle of those sensors consists in dividing an optical beam into two paths with different phase velocities and then recombining them creating an interference pattern in the output spectrum. For this, a standard single mode fiber (SMF) is spliced to a reduced core fiber (RCF) with a core axial offset misalignment, allowing part of the initial power to propagate in the cladding of the RCF, as illustrated in Figure 4.1.

A multi-mode fiber (MMF) is then spliced to the RCF with no misalignment in order to collect and recombine both core and cladding modes creating the interference pattern. The RCF is a commercial SMF that has a core diameter of 6 μm , differently from the SMF and MMF used which have a core diameter of 10 μm and 50 μm , respectively. Its dispersion at 1550 nm is $-20.5 \text{ ps.nm}^{-1}.\text{km}^{-1}$, and its core is doped with GeO_2 with mol% which is calculated to be on the region of 12% and the attenuation at 1550 nm is 0.35 dB/km.

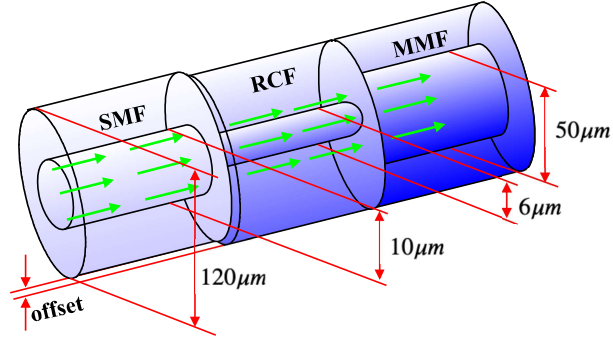


Figure 4.1: Fiber arrangement using an off-setted fiber with reduced core to generate cladding modes. Three different types of optical fibers (SMF, RCF, and MMF) were employed to build the proposed sensors.

4.4.2 Interrogation technique

The interrogation technique applied to the angle and liquid level sensor was based on an analysis of an average measurement of the difference in dB's found between consecutive peaks and troughs obtained by the interference spectrum, that was introduced in [196]. This interrogation technique was chosen mostly because it allows the use of a whole interference spectrum to analyze a sensor, avoiding the intrinsic limits of the operation window associated with long interferometric sensors that are interrogated by analyzing only the wavelength shifts of a single peak.

Specifically, it is a known fact that, for interferometric sensors where part of the beam propagates in a fiber cladding, changes in the external environment, such as liquid level and temperature, result in changes of the effective refractive index of the cladding [197]. Those variations affect not only the central wavelength position of each individual peak found in the interference pattern, but also they affect the amount of light that escape from the cladding to the external medium [198]. As a consequence, if the power of the light traveling in the cladding is reduced, but the power traveling at the fiber core is not, the extinction ratio of the interference pattern obtained when summing both beams tends also to be reduced. This happens as the refractive index of the external medium approaches the index of refraction of the cladding, which occurs, for example, as the level of a liquid in the container is increased. After all, as the liquid level increases, the greater the loss of optical power.

For level sensors we can generally exclude external influences on the light that

propagates in the core. Therefore, the extinction ratio reduction phenomenon observed in the interference spectrum tends to be constant and repeatable over a certain liquid level range, which can be longer than the maximum level permitted by the limitation of the single peak wavelength window interrogation technique [170]. In this way, liquid-level measurements can be achieved for a wider range of sensor sizes with this interrogation technique based on the variations of intensity of the interference pattern.

Similarly, when the bending angle increases, part of the radiation that propagates through the cladding also experiences more scattering reducing its total power at the output. Therefore, this vertical difference can also be used as a stable and simple measurement to sense the angle applied to an optical fiber. However, unlike the liquid level sensor, in the angle sensor, it is not necessary to remove the outer protection layer from the RCF because there is no need of any contact of the cladding with the external medium, which makes the sensor more stable and mechanically robust.

To better understand how the extinction ratio of the interference pattern changes when optical power losses occur in the cladding, simulations of an interferometric fiber sensor were performed based on a two-arm Mach-Zehnder, in which one arm represents the cladding and the other the fiber core, as illustrated in Figure 4.2. In the simulations, was considered for simplicity that the initial electric field E_i that comes from the optical source is split into E_1 and E_2 that propagate in the core and cladding, respectively. Initially, E_1 and E_2 are considered equal, and later E_1 remains constant while E_2 is gradually reduced.

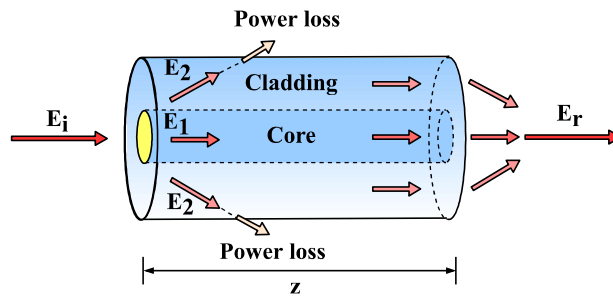


Figure 4.2: Illustrative scheme of the simulations of the changes in the interference pattern when optical losses occur in the cladding of the sensing fiber.

Moreover, the final signal E_r reaching the end of the fiber is the sum of the electric fields in both arms of the interferometer, so that:

$$E_r = E_1 + E_2 = A_1 \sin\left(\omega t - \frac{2\pi}{\lambda_1} z\right) + A_2 \sin\left(\omega t - \frac{2\pi}{\lambda_2} z\right), \quad (4.5)$$

where ω is the light beam angular frequency in rad/s, A_1 and A_2 are the amplitudes of the respective electric fields, z is the length of the waveguide (in this case, the length of the sensor), and λ_1 and λ_2 are the wavelengths related to the refractive indices of the core and the cladding of the sensing fiber, respectively. The result of this analysis is shown in Figure 4.3.

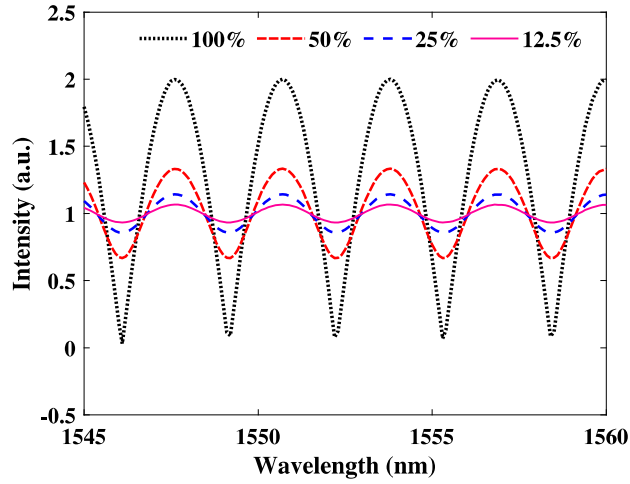


Figure 4.3: Interference pattern as a function of wavelength for the electric field amplitudes in the sensor cladding corresponding to 100%, 50%, 25% and 12.5% of its initial value.

It can be observed in Figure 4.3, that the extinction ratio of the interference pattern is a function of the percentage of the power present in the cladding, since the power of this signal is proportional to the square of the electric field. From these results, it is possible to see that we can directly quantify the loss of optical power in the cladding as a function of the extinction ratio observed in the interference pattern. Based on these considerations, the intensity-based interrogation technique applied in this study consists of measuring the variations of the intensity of the interference pattern $\Delta I_{i,j}$, i. e. the difference between the value of a peak $P_{i,j}$ in the spectrum and the value of a consecutive dip $D_{i,j}$, which is mathematically described as:

$$\Delta I_{i,j} = P_{i,j} - D_{i,j}, \quad (4.6)$$

where the subscript i designates a region of spectrum corresponding to a single peak and its consecutive dip, while the subscript j represents each curve of the interference spectrum corresponding to a single liquid level value, as displayed generically in Figure 4.4, in which the blue curve is a zoom of the experimentally obtained spectrum of the sensor response to the 0 mm liquid level [196].

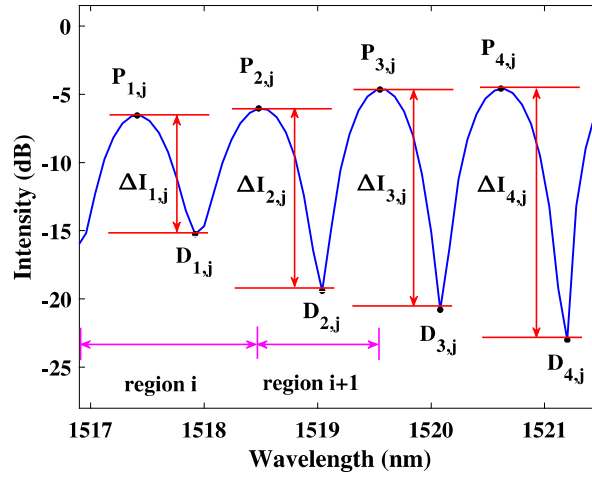


Figure 4.4: Measurement of the intensity variability of the interference pattern (for a single level value) calculated from the difference between peak and dip values.

Since we might have many different modes propagating in the cladding, the resulting spectrum might present fluctuations over different spectral regions, as illustrated in Figure 4.4. Therefore, in order to adapt equation 4.6 to this scenario we take the mean value of $\Delta I_{i,j}$ (denoted by $\overline{\Delta I_j}$) over a set k of spectral regions i , so that:

$$\overline{\Delta I_j} = \frac{1}{k} \sum_{i=1}^k P_{i,j} - D_{i,j}. \quad (4.7)$$

In order to characterize the sensor, the process described in Figure 4.4 and in equation 4.7 must be repeated j times for different spectral curves obtained under different liquid levels. Additionally, this interrogation technique can be performed considering the entire interference pattern (provided there is linearity) or only at specif spectral regions, and consequently, it is totally independent of the size of the observation window. Therefore, this approach eliminates the previously mentioned limitation of sensor size found when the interrogation is made only considering the wavelength shift of a given peak of the obtained interference pattern.

4.4.3 Angle sensor setup

A schematic of the angle sensor experimental setup can be seen in Figure 4.5. A 3 cm radius mandrel made of marble was used as the fiber bending point, where the RCF is placed on a demarcated scale. In this way, we can control the bending angle applied to the fiber. As a pump, we used a -5.5 dBm non-polarized broadband source with a 3 dB bandwidth of 60 nm centered at 1550 nm. Also, the interference pattern created in the sensor was viewed through an optical spectrum analyzer (OSA) model Anritsu MS9740A-009 with a 30 pm resolution. Moreover, 9 cm of RCF is placed precisely with its center at the point where the fiber is banded.

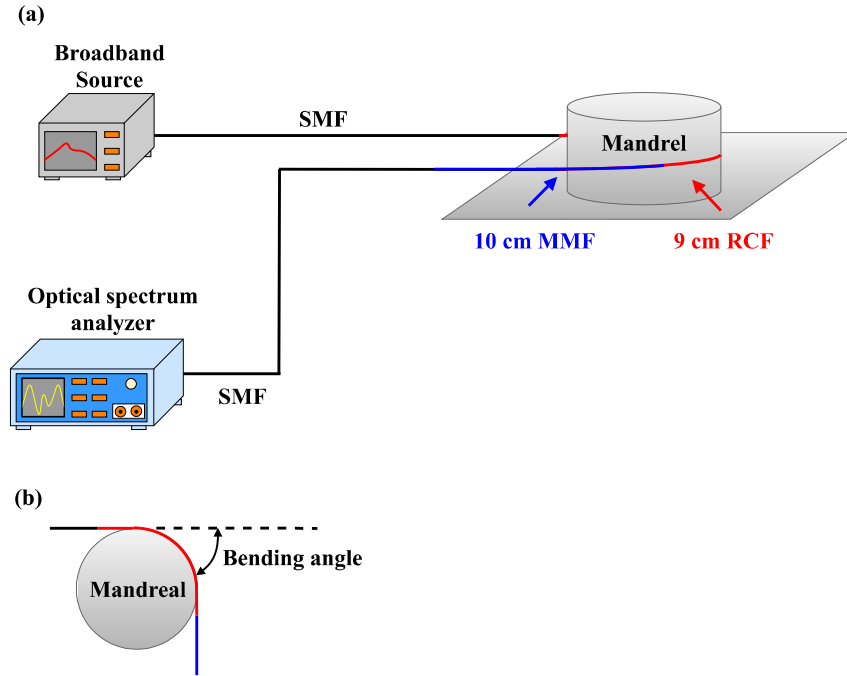


Figure 4.5: Experimental setup of the optical fiber angle sensor. (a) 3D view. (b) Top view.

In this sensor, as illustrated in Figure 4.1, an SMF is spliced to a 9 cm RCF with a core axial offset misalignment of $8\text{ }\mu\text{m}$, allowing part of the initial power to propagate in the cladding of the RCF. The misalignment is easily created by using a default offset splicing function of a commercial fusion splicer (Fujikura 70 S), that allowed to obtain an extinction rate on the interference pattern of about 12 dB. The 9 cm sensor was chosen because it presented better linearity when compared to other sensor lengths that were tested, of 3, 6, and 12 cm. A 10 cm MMF is then

spliced to the RCF with no misalignment in order to collect and recombine both core and cladding modes creating the interference pattern [195].

4.4.4 Liquid level sensor setup

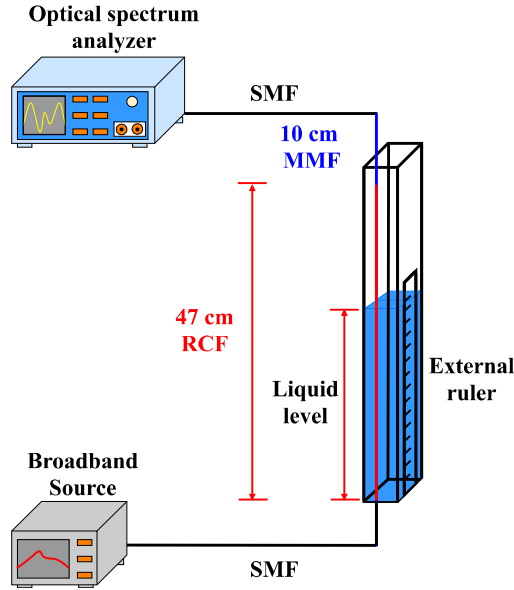


Figure 4.6: Schematic diagram of the experimental setup for the liquid level measurement, where the sensing fiber is placed inside a pipette in which liquids can be readily inserted or removed.

Here, the SMF is spliced to the RCF with a core axial offset misalignment of $4\text{ }\mu\text{m}$. The acrylic protection layer of the RCF is stripped in order to make it sensitive to the external medium, enabling its cladding to be in direct contact with the surrounding environment. Therefore, the effective refractive index, or phase velocity, of the part of the light propagating in the RCF cladding becomes sensitive to the refractive index of the external liquid or gas. The third segment is the MMF that has the role to recombine both the core and cladding modes. Finally, this fiber is spliced to another SMF to connectorize the sensor. The liquid level sensor structure is shown in Figure 4.6. A -2 dBm broadband source with a 3 dB bandwidth centered at 1550 nm is launched into the optical sensor, which is placed inside a 600 mm glass pipe. An external ruler allows measuring the liquid levels while an OSA with 30 pm resolution enables us to observe the interference pattern created at the output of the sensor.

Furthermore, it is important to note that measurement errors can occur if the laser source fluctuates. To avoid this all measurements were performed at a controlled temperature of 24°C. This also ensured that there was no cross-sensitivity with temperature. We also emphasize that the angle and liquid level sensors were well fixed and stretched to assure that mechanical vibrations did not cause measurement errors.

4.5 Results and discussion

Some important considerations are to carry out here to return to the central purpose of this chapter. The interrogation method presented in section 4.4.2 was initially introduced in [196] as an alternative approach to the traditional interrogation technique that measures the wavelength shift of a specific peak in the interference spectrum generated by the sensor. We use this interrogation to avoid this problem of smaller free spectral ranges that long interferometers present. Second, the interference spectra generated experimentally by the interferometric sensor (see sections 4.4.3 and 4.4.4) were grouped sequentially to form a matrix that was later employed to form an image. These images were then processed using the NLM algorithm presented in section 4.3 to remove the noise. Finally, the interference spectra that form the denoised images (processed) were used to characterize the sensor.

4.5.1 Angle sensor

Figure 4.7(a) and Figure 4.7(b) show the raw and denoised images formed from a set of interference spectra obtained from a different angle measurements, respectively. For a better visual perception of the data, a hot scale is chosen in Figure 4.7, where pixels with lighter tones represent wavelength-angle pairs having higher intensity. After noise reduction, the transition between consecutive colors becomes smoother as seen in Figure 4.7(b). This result is reflected in a spectrum with more linear variations when the angle value changes, as shown in Figures 4.8 and 4.9 for the raw and denoised spectra, respectively.

Figure 4.10 shows the non-linearized sensor characterization curve reported in [195] obtained from the interference spectra shown in Figure 4.8, with a determination coefficient $R^2 = 0.959$ for an operating range from 0° to 9°. The limited range of up only to 9° was chosen since the linearity of the sensor rapidly decreased for

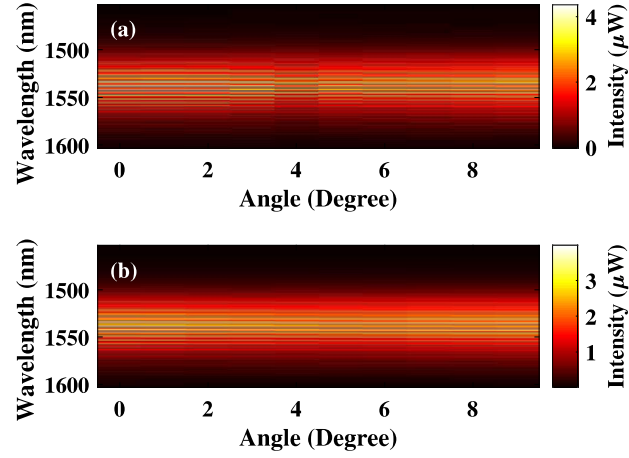


Figure 4.7: Image formed from top view of the measured spectra as a function of angle. (a) Raw image. (b) Denoised image.

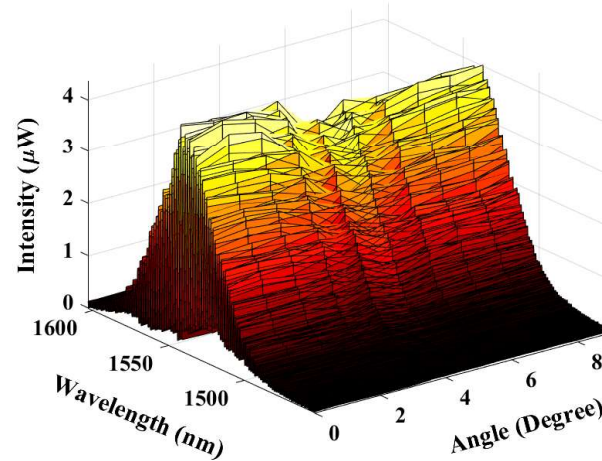


Figure 4.8: Three-dimensional map of the measured raw spectra as a function of angle.

longer angle measurements. For instance, the R^2 was already 0.915 for 11° . After denoising technique, shown in Figure 4.9, significant improvements in experimental angle measurements were obtained, as it can be seen in Figure 4.11. In this case, the sensor linearity is increased to $R^2 = 0.993$ even considering a longer operating range from 0° - 11° .

Also, we perform an investigation that determines which region of the interference spectrum has the highest linearity. This analysis consists in dividing the interference pattern into N parts and individually evaluating each sub-spectrum created by classifying it according to the determination coefficient R^2 , as it was

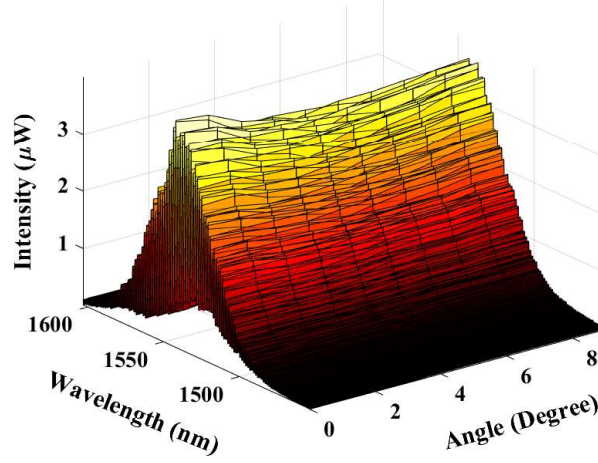


Figure 4.9: Three-dimensional map of the measured denoised spectra as a function of angle.

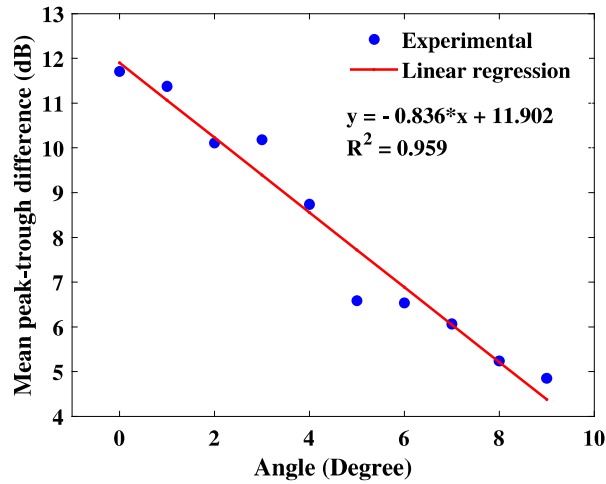


Figure 4.10: Non-linearized sensor characterization curve for angle measurements (after Ref.[195]).

applied in [196]. Figure 4.12 illustrates the degree of linearity for different regions of the interference spectrum generated from the angle experimental data for a range from 0° - 9° . We observe that there are few regions of the spectrum with moderate linearity, where only 16.44% of all analyzed spectra have $R^2 \geq 0.9$. We also point out that there is no region with $R^2 \geq 0.96$. After applying our linearization proposal, 85.97% of all spectra now have an $R^2 \geq 0.9$, as shown in Figure 4.13, even considering angle measurements of up to 11° . Moreover, the highest R^2 obtained is increased to 0.993.

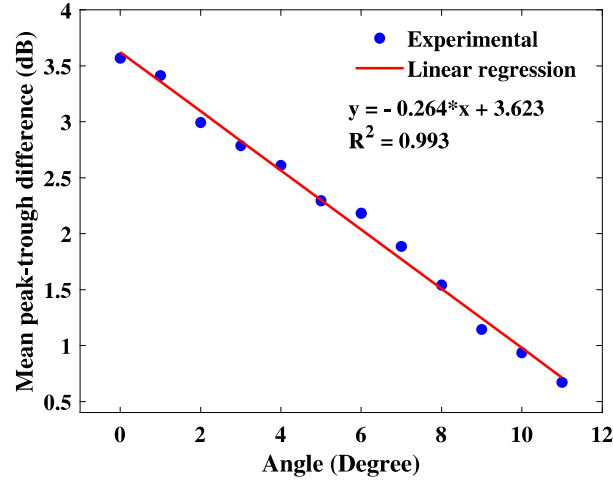


Figure 4.11: Linearized sensor characterization curve for angle measurements.

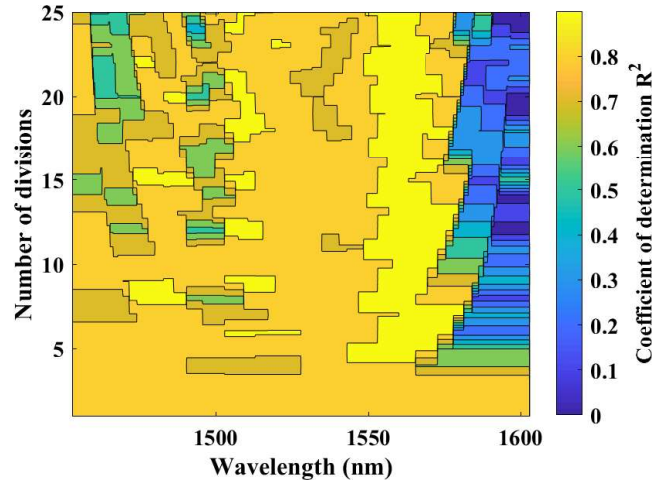


Figure 4.12: Non-linearized linearity map for angle measurement.

4.5.2 Liquid level sensor

The same 2D denoising technique applied for the interferometric fiber sensor of the angle measurement was also performed for a liquid level measurement interferometric fiber sensor. We present in Figure 4.14 only the main result corresponding to the characterization curve of the liquid level sensor without linearization. The data displayed in this figure were acquired from the sensor reported in [171], whose physical size is 50 cm. Nonetheless, the interrogation we used was not the one proposed by [171] which is based on tracking a specific peak found in the interference spectrum

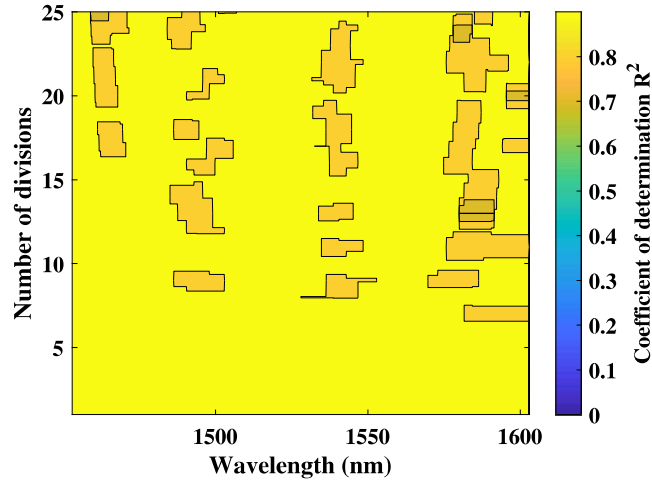


Figure 4.13: Linearized linearity map for angle measurement.

envelope. In spite of being a method of interrogation that enabled the sensor operating range to be extended up to 47 cm (which was the longest operating range in which the sensor worked properly with high linearity while maintaining sensitivity), this is not a universal approach. For instance, there may be cases in which even with envelope analysis the problem of repeating regions of the spectrum within the same observation window still happens. Furthermore, not all interferometric sensors present a favorable envelope that can be used as an interrogation technique based on this approach. For those reasons, we adopt here the interrogation method proposed in [196].

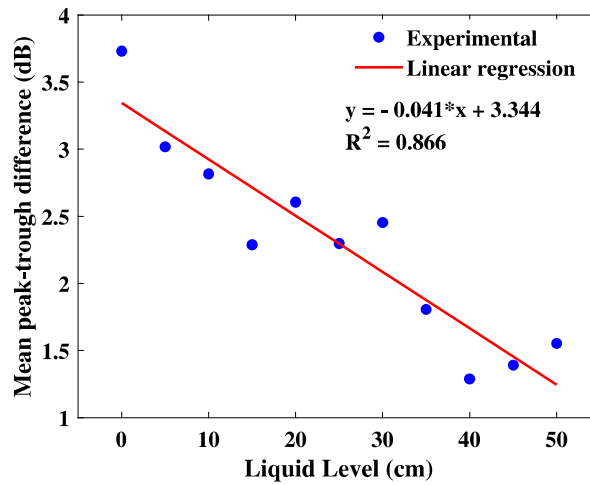


Figure 4.14: Non-linearized sensor characterization curve for liquid level measurements.

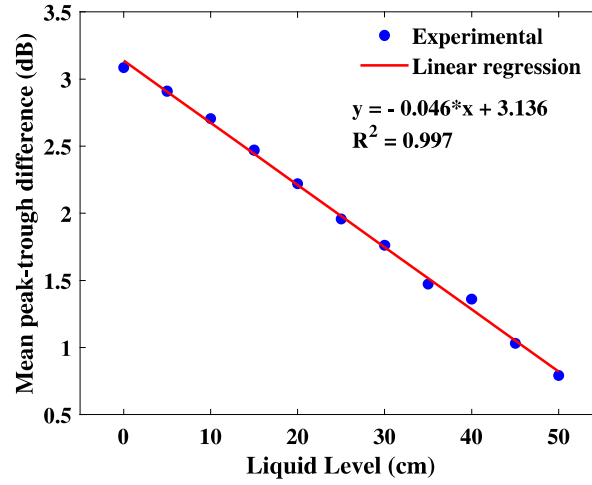


Figure 4.15: Linearized sensor characterization curve for liquid level measurements.

After acquiring the interference spectra corresponding to experimental liquid level measurements from 0 cm to 50 cm, we apply our 2D denoising linearization technique. As a main result, Figure 4.15 presents the characterization curve of this sensor which is now able to perform liquid level measurements up to 50 cm with very high linearity expressed by an R^2 of 0.997. If the linearization is not applied to liquid level measurements up to 50 cm, an $R^2 = 0.866$ is obtained and the sensor would not have sufficient linearity to meet precision requirements for industrial applications where liquid level sensors are required. In this case, we were able to increase the operating range while maintaining a very high linearity.

It is important to note that there is a trade-off between linearity and sensitivity, especially for the angle measurement sensor. Although this effect on sensitivity is more expressive in some cases, this will be inevitable for sensors whose interrogation technique is based on measurements of optical spectral intensity. This may be overcome by improving the resolution of the spectra throughout the data acquisition stage or even changing the interrogation approach. In this regard, to quantify the degree of distortion that our approach introduces in the original spectra, we calculate the mean square error (MSE) between the spectra before and after the application of the denoising. As a result, values of MSE of 2.23×10^{-13} and 4.05×10^{-14} for the liquid level and angle data spectra are obtained. These MSE values clearly show that the NLM algorithm eliminates noise from the spectra, keeping the main structures and details.

Chapter 5

Conclusions, future works and new avenues

This doctoral thesis addressed how signal processing and computational modeling techniques can be employed as effective approaches to significantly improve the performance of optical fiber sensors. Specifically, techniques such as 2D reconstruction, thresholding-based image segmentation, non-local means, and analytical models to improve the performance of RDTs and IFSs were studied.

5.1 Distributed temperature sensing

Detecting small temperature variations over regions of small spatial dimensions is a challenge that RDTS technology still faces and the development of solutions for this is an open problem. In this perspective, the chapter 2 of this thesis presented a solution to this query based on an image processing technique. Specifically, experimental observations presented in this chapter suggest that each hot spot measured by RDTS equipment has an error value for its temperature that depends in a well-defined manner on its spatial size. In this way, it suggests that knowing the size of the measured hot spot, we can determine what is the temperature error associated with each hot spot and thus correct it employing polynomial fitting functions. After applying this approach along with thresholding-based image segmentation, the simultaneous detection and correction of hot spots of sizes ranging from 15 m to 3 cm are achieved experimentally with 98.22% accuracy. This result places RTDS systems on a new level of applicability since it now enables a fiber optical cable to be employed in the temperature monitoring of regions smaller than the RDTS equipment's spatial resolution.

Furthermore, the degree of coverage of this solution is not restricted only to RDTS systems, but with appropriate adaptations, it should be able to be applied to other types of optical fiber sensors for measuring vibration, pressure, liquid level,

among other parameters in which new insights can be obtained. Future work related to signal processing developed during this Ph.D. work for the RDTS technology comprises evaluating the performance of our method over complex temperature distributions data in which the position, number, spatial size, format, and temperature of the hot spots change dynamically over the fiber length and time. This can be accomplished by adopting a multi-level thresholding-based image segmentation. Such a more realistic scenario may provide a more general validation of the approach presented in this thesis.

The main bottleneck of RDTS technology hardware is its receiver system, requiring a detailed analysis of the electronic circuit components. In this perspective, in chapter 3 of this thesis, the receiver of the RDTS was characterized by a new analytical formalism that for the first time takes into account the sensitivity of the signal of interest with temperature. The theoretical analysis is validated with simulations allowing us to precisely identify essential parameters in the receiver design for RDTS operation. Among the parameters characterized are the minimum noise/SNR levels allowed to detect tenths of degree of temperature variations, the optimum value for signal amplification gain, resistance value, and bandwidth. Also, all the analyzed parameters are related to basic criteria in the evaluation of sensor performance, such as accuracy, spatial resolution and range.

The developed analysis allows predicting and directing the design of very low intensity signals reception used in temperature fiber sensors, reducing the complexity in designing such sensors when hardware level changes are required. With these specifications, the development of a prototype of a receiver system with high sensitivity to detect low-intensity signals is the next step to be considered and we leave it as a suggestion for future work to be performed. In summary, despite the significant advance that signal processing techniques have provided to RDTS technology, we strongly believe that for this sensor technology to continue to evolve to meet the current demands of the industry for highly accurate sensors, it will be necessary to develop RDTS devices with new high sensitivity configurations.

5.2 Interferometric fiber sensors

Interferometric fiber sensors are widely employed in the monitoring of several physical parameters and are commonly associated with features like having easy fabrication processes, and being very compact structures in all-fiber setups. However,

depending on the type of interrogation mechanism, some problems may arise. For instance, in some cases, for those sensors to achieve high resolution, its operation range has to be significantly reduced so that it can work within its linear response range. By focusing our attention on this issue, we propose and experimentally demonstrate in chapter 4 a linearization technique for interferometric fiber sensors. From a 2D reconstruction of the interference spectra and subsequent denoising process, relevant improvements in linearity and range are obtained for both angle and liquid level sensors. Such an approach is not only inexpensive because it does not require to modify the physical structure of the sensor, but is also easy to implement on any graphical interface. The results presented here show that our linearization technique can increase the linearity and the operation range of existing interferometric fiber sensors. A significant improvement in R^2 of 8.52 % and 15.12 % was demonstrated for angle and liquid level measurement sensors, respectively. In addition, our proposed 2D denoising linearization technique potentially can be applied to interferometric sensors that use different interrogation approaches and measure physical parameters beyond those evaluated in this study. The evaluation of the linearization technique proposed in this thesis on interferometric sensors capable of measuring liquid level variations greater than 50 cm can be investigated as future work.

5.3 New avenues

Furthermore, for both distributed and interferometric fiber sensors covered in this thesis, we believe that a direction for future investigations will be to conduct field tests of the solutions developed here. In which possible issues can be discovered and solved, as well as new insights can be obtained. The next steps still include the intelligent instrumentation of these sensors, with the sensor itself making decisions and changing its configuration dynamically according to the current monitoring circumstances. This implies that their interfaces are connected to other equipment and therefore will require the development of new architectures.

Finally, it is expected that the research of new signal processing techniques coupled with the continued development of narrow-line high power lasers, faster A/D converters, high-gain amplifiers with low noise insertion, will continue to drive the development of new optical fiber sensing technologies in the coming years.

Bibliography

- [1] E. Gerstner, “Nobel Prize 2009: Kao, & Boyle Smith,” *Nature Physics*, vol. 5, no. 11, pp. 780–780, Oct. 2009.
- [2] E. J. Malecki, “The economic geography of the Internet’s infrastructure,” *Economic geography*, vol. 78, no. 4, pp. 399–424, Oct. 2002.
- [3] A. M. Townsend, “The Internet and the rise of the new network cities, 1969–1999,” *Environment and planning B: Planning and Design*, vol. 28, no. 1, pp. 39–58, Feb. 2001.
- [4] X. Yi, F. Liu, J. Liu, and H. Jin, “Building a network highway for big data: Architecture and challenges,” *IEEE Network*, vol. 28, no. 4, pp. 5–13, Jul. 2014.
- [5] J. M. Senior and M. Y. Jamro, *Optical fiber communications: principles and practice*. Pearson Education, 2009.
- [6] G. P. Agrawal, *Fiber-optic communication systems*. John Wiley & Sons, 2012, vol. 222.
- [7] A. Hartog, *An Introduction to Distributed Optical Fibre Sensors. Series in Fiber Optic Sensors*. CRC Press: Boca Raton, FL, USA, 2017.
- [8] S. Yin, P. B. Ruffin, and T. Francis, *Fiber optic sensors*. CRC press, 2017.
- [9] Y. Qian, Y. Zhao, Q.-l. Wu, and Y. Yang, “Review of salinity measurement technology based on optical fiber sensor,” *Sensors and Actuators B: Chemical*, vol. 260, pp. 86–105, May 2018.
- [10] H.-E. Joe, H. Yun, S.-H. Jo, M. B. Jun, and B.-K. Min, “A review on optical fiber sensors for environmental monitoring,” *International journal of precision engineering and manufacturing-green technology*, vol. 5, no. 1, pp. 173–191, May 2018.
- [11] Y. Zhao, R.-j. Tong, F. Xia, and Y. Peng, “Current status of optical fiber biosensor based on surface plasmon resonance,” *Biosensors and Bioelectronics*, vol. 142, pp. 1–12, Oct. 2019.

- [12] H. Nazemi, A. Joseph, J. Park, and A. Emadi, “Advanced micro-and nano-gas sensor technology: A review,” *Sensors*, vol. 19, no. 6, pp. 1–23, Mar. 2019.
- [13] P. Lu, N. Lalam, M. Badar, B. Liu, B. T. Chorpeneing, M. P. Buric, and P. R. Ohodnicki, “Distributed optical fiber sensing: Review and perspective,” *Applied Physics Reviews*, vol. 6, no. 4, pp. 1–35, Oct. 2019.
- [14] A. G. Leal-Junior, C. A. Diaz, L. M. Avellar, M. J. Pontes, C. Marques, and A. Frizera, “Polymer optical fiber sensors in healthcare applications: A comprehensive review,” *Sensors*, vol. 19, no. 14, pp. 1–30, Jul. 2019.
- [15] D. Gloge, “Weakly guiding fibers,” *Applied Optics*, vol. 10, no. 10, pp. 2252–2258, Oct. 1971.
- [16] D. Gloge and E. Marcatili, “Multimode theory of graded-core fibers,” *Bell System Technical Journal*, vol. 52, no. 9, pp. 1563–1578, Nov. 1973.
- [17] M. J. Adams, “An introduction to optical waveguides,” 1981.
- [18] A. W. Snyder and J. Love, *Optical waveguide theory*. Springer Science & Business Media, 2012.
- [19] L. B. Jeunhomme, *Single-mode fiber optics: principles and applications*. Routledge, 2019.
- [20] H. O. Pierson, *Handbook of chemical vapor deposition: principles, technology and applications*. William Andrew, 1999.
- [21] M. Kawachi, M. Yasu, and T. Eda Hiro, “Fabrication of SiO₂-TiO₂ glass planar optical waveguides by flame hydrolysis deposition,” *Electronics Letters*, vol. 19, no. 15, pp. 583–584, Jun. 1983.
- [22] P. Geittner, D. Küppers, and H. Lydtin, “Low-loss optical fibers prepared by plasma-activated chemical vapor deposition (CVD),” *Applied Physics Letters*, vol. 28, no. 11, pp. 645–646, Aug. 1976.
- [23] T. Miya, Y. Terunuma, T. Hosaka, and T. Miyashita, “Ultimate low-loss single-mode fibre at 1.55 μm ,” *Electronics Letters*, vol. 15, no. 4, pp. 106–108, Feb. 1979.
- [24] S. Ten, “Ultra low-loss optical fiber technology,” in *Optical Fiber Communications Conference and Exhibition*, Aug. 2016, pp. 1–3.

- [25] D. Keck, R. Maurer, and P. Schultz, "On the ultimate lower limit of attenuation in glass optical waveguides," *Applied Physics Letters*, vol. 22, no. 7, pp. 307–309, Oct. 1973.
- [26] I. Hayashi, M. Panish, P. Foy, and S. Sumski, "Junction lasers which operate continuously at room temperature," *Applied Physics Letters*, vol. 17, no. 3, pp. 109–111, Oct. 1970.
- [27] V. Vali and R. Shorthill, "Fiber ring interferometer," *Applied Optics*, vol. 15, no. 5, pp. 1099–1100, Feb. 1976.
- [28] J. Cole, R. Johnson, and P. Bhuta, "Fiber-optic detection of sound," *The Journal of the Acoustical Society of America*, vol. 62, no. 5, pp. 1136–1138, Aug. 1977.
- [29] J. A. Bucaro, H. D. Dardy, and E. F. Carome, "Optical fiber acoustic sensor," *Applied Optics*, vol. 16, no. 7, pp. 1761–1762, Apr. 1977.
- [30] M. Johnson and R. Ulrich, "Fibre-optical strain gauge," *Electronics Letters*, vol. 14, no. 14, pp. 432–433, Jul. 1978.
- [31] J. O. Norris, "Current status and prospects for the use of optical fibres in chemical analysis. a review," *The Analyst*, vol. 114, no. 11, pp. 1359–1372, Nov. 1989.
- [32] K. A. Wickersheim, *Optical temperature measurement technique utilizing phosphors*, US Patent 4075493, Feb. 1978.
- [33] A. M. Smith, "Polarization and magneto-optic properties of single-mode optical fiber," *Applied Optics*, vol. 17, no. 1, pp. 52–56, Jan. 1978.
- [34] B. Budiansky, D. C. Drucker, G. S. Kino, and J. R. Rice, "Pressure sensitivity of a clad optical fiber," *Applied Optics*, vol. 18, no. 24, pp. 4085–4088, Dec. 1979.
- [35] W. H. Quick, K. A. James, and V. H. Strahan, *Means for sensing and color multiplexing optical data over a compact fiber optic transmission system*, US Patent 4223216, Sep. 1980.
- [36] T. Bosselmann and R. Ulrich, "High-accuracy position-sensing with fiber-coupled white-light interferometers," in *2nd International Conference on Optical Fibre Sensors, Stuttgart, Germany*, vol. 514, International Society for Optics and Photonics, Nov. 1984, pp. 361–364.

- [37] A. D. Kersey, "Optical fiber sensors for permanent downwell monitoring applications in the oil and gas industry," *IEICE Transactions on Electronics*, vol. 83, no. 3, pp. 400–404, Mar. 2000.
- [38] R. Moghe, A. R. Iyer, F. C. Lambert, and D. M. Divan, "A low-cost wireless voltage sensor for monitoring MV/HV utility assets," *IEEE Transactions on Smart Grid*, vol. 5, no. 4, pp. 2002–2009, Jul. 2014.
- [39] A. Raghavan, P. Kiesel, M. Teepe, F. Cheng, Q. Chen, T. Karin, D. Jung, S. Mostafavi, M. Smith, R. Stinson, *et al.*, "Low-cost embedded optical sensing systems for distribution transformer monitoring," *IEEE Transactions on Power Delivery*, vol. 36, no. 2, pp. 1007–1014, Jun. 2020.
- [40] F. S. Delgado, J. P. Carvalho, T. V. Coelho, and A. B. Dos Santos, "An optical fiber sensor and its application in UAVs for current measurements," *Sensors*, vol. 16, no. 11, pp. 1–8, Oct. 2016.
- [41] L. Palmieri, D. Sarchi, and A. Galtarossa, "Distributed measurement of high electric current by means of polarimetric optical fiber sensor," *Optics Express*, vol. 23, no. 9, pp. 11 073–11 079, Apr. 2015.
- [42] P. Wang, Y. Semenova, Q. Wu, and G. Farrell, "A fiber-optic voltage sensor based on macrobending structure," *Optics & Laser Technology*, vol. 43, no. 5, pp. 922–925, Jul. 2011.
- [43] J. M. Lukens, N. Lagakos, V. Kaybulkin, C. J. Vizas, and D. J. King, "Equalization of Intensity-Modulated Fiber-Optic Voltage Sensors for Power Distribution Systems," *IEEE Photonics Technology Letters*, vol. 33, no. 16, pp. 880–883, Jan. 2021.
- [44] C. E. Campanella, A. Cuccovillo, C. Campanella, A. Yurt, and V. Passaro, "Fibre Bragg grating based strain sensors: Review of technology and applications," *Sensors*, vol. 18, no. 9, pp. 1–27, Sep. 2018.
- [45] W. Li, Y. Yuan, J. Yang, and L. Yuan, "Review of Optical Fiber Sensor Network Technology Based on White Light Interferometry," *Photonic Sensors*, vol. 11, no. 1, pp. 31–44, Jan. 2021.
- [46] Y. Bao, Y. Huang, M. S. Hoehler, and G. Chen, "Review of fiber optic sensors for structural fire engineering," *Sensors*, vol. 19, no. 4, pp. 1–23, Feb. 2019.
- [47] B. Lee, "Review of the present status of optical fiber sensors," *Optical fiber technology*, vol. 9, no. 2, pp. 57–79, Apr. 2003.

- [48] J. Brooks, R. Wentworth, R. Youngquist, M. Tur, B. Kim, and H. Shaw, "Coherence multiplexing of fiber-optic interferometric sensors," *Journal of Lightwave Technology*, vol. 3, no. 5, pp. 1062–1072, Oct. 1985.
- [49] J. Brooks, B. Moslehi, B. Kim, and H. Shaw, "Time-domain addressing of remote fiber-optic interferometric sensor arrays," *Journal of Lightwave Technology*, vol. 5, no. 7, pp. 1014–1023, Jul. 1987.
- [50] I. Sakai, R. Youngquist, and G. Parry, "Multiplexing of optical fiber sensors using a frequency-modulated source and gated output," *Journal of Lightwave Technology*, vol. 5, no. 7, pp. 932–940, Jul. 1987.
- [51] J. Mlodzianowski, D. Uttamchandani, and B. Culshaw, "A simple frequency domain multiplexing system for optical point sensors," *Journal of Lightwave Technology*, vol. 5, no. 7, pp. 1002–1007, Jul. 1987.
- [52] G. Yilmaz and S. E. Karlik, "A distributed optical fiber sensor for temperature detection in power cables," *Sensors and Actuators A: Physical*, vol. 125, no. 2, pp. 148–155, Jan. 2006.
- [53] R. Andrades, H. C. Guabiroba, M. S. Hora, R. F. Martins, V. L. Rodrigues, C. C. Vilar, T. Giarrizzo, and J.-C. Joyeux, "Early evidences of niche shifts in estuarine fishes following one of the world's largest mining dam disasters," *Marine Pollution Bulletin*, vol. 154, pp. 1–5, May 2020.
- [54] C. dos Santos Vergilio, D. Lacerda, B. C. V. de Oliveira, E. Sartori, G. M. Campos, A. L. de Souza Pereira, D. B. de Aguiar, T. da Silva Souza, M. G. de Almeida, F. Thompson, *et al.*, "Metal concentrations and biological effects from one of the largest mining disasters in the world (Brumadinho, Minas Gerais, Brazil)," *Scientific Reports*, vol. 10, no. 1, pp. 1–12, Apr. 2020.
- [55] X. Wang, J. Lai, J. Qiu, W. Xu, L. Wang, and Y. Luo, "Geohazards, reflection and challenges in Mountain tunnel construction of China: A data collection from 2002 to 2018," *Geomatics, Natural Hazards and Risk*, vol. 11, no. 1, pp. 766–784, Apr. 2020.
- [56] M. Biezma, M. Andrés, D. Agudo, and E. Briz, "Most fatal oil & gas pipeline accidents through history: A lessons learned approach," *Engineering Failure Analysis*, vol. 110, pp. 1–14, Feb. 2020.
- [57] J.-E. Vinnem and W. Røed, "Lessons from Major Accidents," in *Offshore Risk Assessment Vol. 1*, Springer, 2020, pp. 103–184.

- [58] E. Tetzlaff, T. Eger, A. Pegoraro, S. Dorman, and V. Pakalnis, “Analysis of Recommendations from Mining Incident Investigative Reports: A 50-Year Review,” *Safety*, vol. 6, no. 1, pp. 1–15, Jan. 2020.
- [59] X. Bao and L. Chen, “Recent progress in distributed fiber optic sensors,” *Sensors*, vol. 12, no. 7, pp. 8601–8639, Jun. 2012.
- [60] P. Debye, “Molecular-weight determination by light scattering,” *The Journal of Physical Chemistry*, vol. 51, no. 1, pp. 18–32, Aug. 1947.
- [61] R. Juškaitis, A. M. Mamedov, V. T. Potapov, and S. V. Shatalin, “Interferometry with Rayleigh backscattering in a single-mode optical fiber,” *Optics Letters*, vol. 19, no. 3, pp. 225–227, Feb. 1994.
- [62] F. Peng, H. Wu, X.-H. Jia, Y.-J. Rao, Z.-N. Wang, and Z.-P. Peng, “Ultra-long high-sensitivity Φ -OTDR for high spatial resolution intrusion detection of pipelines,” *Optics Express*, vol. 22, no. 11, pp. 13 804–13 810, Jun. 2014.
- [63] S. Dou, N. Lindsey, A. M. Wagner, T. M. Daley, B. Freifeld, M. Robertson, J. Peterson, C. Ulrich, E. R. Martin, and J. B. Ajo-Franklin, “Distributed acoustic sensing for seismic monitoring of the near surface: A traffic-noise interferometry case study,” *Scientific Reports*, vol. 7, no. 1, pp. 1–12, Sep. 2017.
- [64] A. Masoudi, J. A. Pilgrim, T. P. Newson, and G. Brambilla, “Subsea Cable Condition Monitoring With Distributed Optical Fiber Vibration sensor,” *Journal of Lightwave Technology*, vol. 37, no. 4, pp. 1352–1358, Jan. 2019.
- [65] Z. Wang, B. Lu, Q. Ye, and H. Cai, “Recent Progress in Distributed Fiber Acoustic Sensing with Φ -OTDR,” *Sensors*, vol. 20, no. 22, pp. 1–26, Nov. 2020.
- [66] K. Miah and D. K. Potter, “A review of hybrid fiber-optic distributed simultaneous vibration and temperature sensing technology and its geophysical applications,” *Sensors*, vol. 17, no. 11, pp. 1–125, Nov. 2017.
- [67] S. M. Maughan, H. H. Kee, and T. P. Newson, “Simultaneous distributed fibre temperature and strain sensor using microwave coherent detection of spontaneous Brillouin backscatter,” *Measurement Science and Technology*, vol. 12, no. 7, pp. 1–9, Feb. 2001.

- [68] T. Horiguchi and M. Tateda, "BOTDA-nondestructive measurement of single-mode optical fiber attenuation characteristics using Brillouin interaction: Theory," *Journal of Lightwave Technology*, vol. 7, no. 8, pp. 1170–1176, Aug. 1989.
- [69] T. Kurashima, T. Horiguchi, and M. Tateda, "Distributed-temperature sensing using stimulated Brillouin scattering in optical silica fibers," *Optics Letters*, vol. 15, no. 18, pp. 1038–1040, Sep. 1990.
- [70] K. Y. Song, Z. He, and K. Hotate, "Distributed strain measurement with millimeter-order spatial resolution based on Brillouin optical correlation domain analysis," *Optics Letters*, vol. 31, no. 17, pp. 2526–2528, Sep. 2006.
- [71] Y. Cho, G. Lees, G. Hilton, X. Shu, K. Sugden, A. Strong, A. Hartog, and T. Newson, "100 km Distributed Fiber Optic Sensor Based on the Coherent Detection of Brillouin Backscatter, with a Spatial Resolution of 10 m, Enhanced Using Two Stages of Remotely Pumped Erbium-Doped Fiber Combined with Raman Amplification," in *Optical Fiber Sensors*, Optical Society of America, Oct. 2006, pp. 1–4.
- [72] M. N. Alahbabi, Y. T. Cho, and T. P. Newson, "150-km-range distributed temperature sensor based on coherent detection of spontaneous Brillouin backscatter and in-line Raman amplification," *Journal of the Optical Society of America B*, vol. 22, no. 6, pp. 1321–1324, Jun. 2005.
- [73] D. A. Long, "The Raman effect: A unified treatment of the theory of Raman scattering by molecules," Apr. 2002.
- [74] J. P. Dakin, D. J. Pratt, G. W. Bibby, and J. N. Rose, "Distributed antistokes ratio thermometry," in *Optical Fiber Sensors*, Optical Society of America, Jan. 1985, pp. 1–4.
- [75] J. P. Dakin, D. J. Pratt, G. W. Bibby, and J. N. Ross, "Distributed optical fibre Raman temperature sensor using a semiconductor light source and detector," *Electronics Letters*, vol. 21, no. 13, pp. 569–570, Jun. 1985.
- [76] A. H. Hartog, A. P. Leach, and M. P. Gold, "Distributed temperature sensing in solid-core fibres," *Electronics Letters*, vol. 21, no. 23, pp. 1061–1062, Nov. 1985.

- [77] R. Rathod, R. D. Pechstedt, D. A. Jackson, and D. J. Webb, "Distributed temperature-change sensor based on Rayleigh backscattering in an optical fiber," *Optics Letters*, vol. 19, no. 8, pp. 593–595, Apr. 1994.
- [78] T. Horiguchi, K. Shimizu, T. Kurashima, M. Tateda, and Y. Koyamada, "Development of a distributed sensing technique using Brillouin scattering," *Journal of Lightwave Technology*, vol. 13, no. 7, pp. 1296–1302, Jul. 1995.
- [79] S. W. Tyler, J. S. Selker, M. B. Hausner, C. E. Hatch, T. Torgersen, C. E. Thodal, and S. G. Schladow, "Environmental temperature sensing using Raman spectra DTS fiber-optic methods," *Water Resources Research*, vol. 45, no. 4, pp. 1–11, Jan. 2009.
- [80] J. P. Bazzo, F. Mezzadri, E. V. da Silva, D. R. Pipa, C. Martelli, and J. C. C. da Silva, "Thermal Imaging of Hydroelectric Generator Stator Using a DTS system," *IEEE Sensors Journal*, vol. 15, no. 11, pp. 6689–6696, Nov. 2015.
- [81] A. A. Khan, V. Vrabie, J. I. Mars, A. Girard, and G. D'Urso, "A Source Separation Technique for Processing of Thermometric Data From Fiber-Optic DTS Measurements for Water Leakage Identification in Dikes," *IEEE Sensors Journal*, vol. 8, no. 7, pp. 1118–1129, Jul. 2008.
- [82] Z. Sha-lu, G. Hui, P. Jian-yu, Z. Hui-hui, and W. Jian-feng, "Application research of distributed optical fiber Raman temperature sensor in the security of oil depot," in *Optoelectronics Global Conference*, Oct. 2015, pp. 1–4.
- [83] G. R. Williams, G. Brown, W. Hawthorne, A. H. Hartog, and P. C. Waite, "Distributed temperature sensing (DTS) to characterize the performance of producing oil wells," in *Industrial Sensing Systems*, A. Wang and E. Udd, Eds., vol. 4202, SPIE, Nov. 2000, pp. 39–54.
- [84] P. Ferdinand, M. Giuseffi, N. Roussel, S. Rougeault, O. Fléchon, and V. Barentin, "Monitoring the energy efficiency of buildings with Raman DTS and embedded optical fiber cables," in *23rd International Conference on Optical Fibre Sensors*, SPIE, Jun. 2014, pp. 1398–1401.
- [85] J. Zhang, P. Wei, and Q. Liu, "Monitoring a Heatsink Temperature Field Using Raman-Based Distributed Temperature Sensor in a Vacuum and -173 °C Environment," *Sensors*, vol. 19, no. 19, pp. 1–14, Sep. 2019.

- [86] A. Kimura, E. Takada, K. Fujita, M. Nakazawa, H. Takahashi, and S. Ichige, "Application of a Raman distributed temperature sensor to the experimental fast reactor JOYO with correction techniques," *Measurement Science and Technology*, vol. 12, no. 7, pp. 966–973, May 2001.
- [87] B. Yan, J. Li, M. Zhang, J. Zhang, L. Qiao, and T. Wang, "Raman Distributed Temperature Sensor with Optical Dynamic Difference Compensation and Visual Localization Technology for Tunnel Fire Detection," *Sensors*, vol. 19, no. 10, pp. 1–12, May 2019.
- [88] R. M. Odic, R. I. Jones, and R. P. Tatam, "Distributed temperature sensor for aeronautic applications," in *15th Optical Fiber Sensors Conference Technical Digest*, vol. 1, May 2002, pp. 459–462.
- [89] C. Cangialosi, Y. Ouerdane, S. Girard, A. Boukenter, S. Delepine-Lesoille, J. Bertrand, C. Marcandella, P. Paillet, and M. Cannas, "Development of a Temperature Distributed Monitoring System Based On Raman Scattering in Harsh Environment," *IEEE Transactions on Nuclear Science*, vol. 61, no. 6, pp. 3315–3322, Dec. 2014.
- [90] C. E. Campanella, G. Ai, and A. Ukil, "Distributed fiber optics techniques for gas network monitoring," in *IEEE International Conference on Industrial Technology*, Mar. 2016, pp. 646–651.
- [91] S. Nakamura, S. Morooka, and K. Kawasaki, "Conductor temperature monitoring system in underground power transmission XLPE cable joints," *IEEE Transactions on Power Delivery*, vol. 7, no. 4, pp. 1688–1697, Oct. 1992.
- [92] Y. Liu, J. Yin, Y. Tian, and X. Fan, "Design and Performance Test of Transformer Winding Optical Fibre Composite Wire Based on Raman Scattering," *Sensors*, vol. 19, no. 9, May 2019.
- [93] F. Suárez, J. E. Aravena, M. B. Hausner, A. E. Childress, and S. W. Tyler, "Assessment of a vertical high-resolution distributed-temperature-sensing system in a shallow thermohaline environment," *Hydrology and Earth System Sciences*, vol. 15, no. 3, pp. 1081–1093, Mar. 2011.
- [94] A. Curtis and P. Kyle, "Geothermal point sources identified in a fumarolic ice cave on erebus volcano, Antarctica using fiber optic distributed temperature sensing," *Geophysical Research Letters*, vol. 38, no. 16, pp. 1–7, Aug. 2011.

- [95] O. Hoes, R. Schilperoort, W. Luxemburg, F. Clemens, and N. van de Giesen, "Locating illicit connections in storm water sewers using fiber-optic distributed temperature sensing," *Water Research*, vol. 43, no. 20, pp. 5187–5197, Aug. 2009.
- [96] C. A. Keller, H. Huwald, M. K. Vollmer, A. Wenger, M. Hill, M. B. Parlange, and S. Reimann, "Fiber optic distributed temperature sensing for the determination of the nocturnal atmospheric boundary layer height," *Atmospheric Measurement Techniques*, vol. 4, no. 2, pp. 143–149, Feb. 2011.
- [97] T. Read, O. Bour, V. Bense, T. Le Borgne, P. Goderniaux, M. Klepikova, R. Hochreutener, N. Lavenant, and V. Boschero, "Characterizing groundwater flow and heat transport in fractured rock using fiber-optic distributed temperature sensing," *Geophysical Research Letters*, vol. 40, no. 10, pp. 2055–2059, May 2013.
- [98] N. Van De Giesen, S. C. Steele-Dunne, J. Jansen, O. Hoes, M. B. Hausner, S. Tyler, and J. Selker, "Double-ended calibration of fiber-optic Raman spectra distributed temperature sensing data," *Sensors*, vol. 12, no. 5, pp. 5471–5485, Apr. 2012.
- [99] C. Lee, K. Suh, and T. Landry, "The implementation of self calibration techniques in Raman backscatter based fiber optic distributed temperature system (DTS) technology," in *Transmission and Distribution Conference and Exposition*., IEEE, Apr. 2008, pp. 1–6.
- [100] S. D. Dyer, B. Baek, S. W. Nam, M. G. Tanner, and R. H. Hadfield, "High spatial resolution distributed fiber sensor using Raman scattering in single-mode fiber," in *Laser Science to Photonic Applications*, May 2010, pp. 1–2.
- [101] Z. L. Wang, J. Chang, S. S. Zhang, G. P. Lv, W. J. Wang, S. Jiang, X. Z. Liu, X. H. Liu, S. Luo, B. N. Sun, and Y. N. Liu, "Spatial Resolution Improvement of Distributed Raman Temperature Measurement System," *IEEE Sensors Journal*, vol. 13, no. 11, pp. 4271–4278, Nov. 2013.
- [102] J. P. Bazzo, D. R. Pipa, C. Martelli, E. Vagner Silva, and J. C. Cardozo Silva, "Improving Spatial Resolution of Raman DTS Using Total Variation Deconvolution," *IEEE Sensors Journal*, vol. 16, no. 11, pp. 4425–4430, Jun. 2016.

- [103] L. C. B. Silva, J. L. A. Samatelo, M. E. V. Segatto, J. P. Bazzo, J. C. C. Silva, C. Martelli, and M. J. Pontes, “NARX neural network model for strong resolution improvement in a distributed temperature sensor,” *Applied Optics*, vol. 57, no. 20, pp. 5859–5864, Jul. 2018.
- [104] J. Jiang, J. Sheng, Q. Wu, Z. Li, L. Zhong, M. Song, Z. Hong, and Z. Jin, “Spatial and Temporal Resolution Optimization on Raman Distributed Temperature Sensor System for Quench Detection in a No-Insulated Coil,” *IEEE Transactions on Applied Superconductivity*, vol. 29, no. 5, pp. 1–5, Aug. 2019.
- [105] T. D. Vo, J. He, E. Magi, M. J. Collins, A. S. Clark, B. G. Ferguson, C. Xiong, and B. J. Eggleton, “Chalcogenide fiber-based distributed temperature sensor with sub-centimeter spatial resolution and enhanced accuracy,” *Optics Express*, vol. 22, no. 2, pp. 1560–1568, Jan. 2014.
- [106] I. Laarossi, R. Ruiz-Lombera, M. Quintela, J. Mirapeix, D. Lima, D. Solana, and J. Lopez-Higuera, “Ultra-high temperature distributed sensor based on Raman and multimode gold-coated fiber,” in *Advanced Photonics*, Optical Society of America, Jun. 2016, pp. 1–3.
- [107] L. Pan, K. Liu, J. Jiang, C. Ma, M. Tian, and T. Liu, “A De-Noising Algorithm Based on EEMD in Raman-Based Distributed Temperature Sensor,” *IEEE Sensors Journal*, vol. 17, no. 1, pp. 134–138, Jan. 2017.
- [108] J. Li, Q. Zhang, Y. Xu, M. Zhang, J. Zhang, L. Qiao, M. M. Promi, and T. Wang, “High-accuracy distributed temperature measurement using difference sensitive - temperature compensation for Raman-based optical fiber sensing,” *Optics Express*, vol. 27, no. 25, pp. 36 183–36 196, Dec. 2019.
- [109] J. Li, Q. Zhang, T. Yu, M. Zhang, J. Zhang, L. Qiao, and T. Wang, “R-DTS with Heat Transfer Functional Model for Perceiving the Surrounding Temperature,” *IEEE Sensors Journal*, vol. 20, no. 2, pp. 816–822, Sep. 2020.
- [110] Y. Xu, J. Li, M. Zhang, T. Yu, B. Yan, X. Zhou, F. Yu, J. Zhang, L. Qiao, T. Wang, and S. Gao, “Pipeline Leak Detection Using Raman Distributed Fiber Sensor With Dynamic Threshold Identification Method,” *IEEE Sensors Journal*, vol. 20, no. 14, pp. 7870–7877, Jul. 2020.

- [111] A. Signorini, S. Faralli, M. A. Soto, G. Sacchi, F. Baronti, R. Barsacchi, A. Lazzeri, R. Roncella, G. Bolognini, and F. Di Pasquale, “40 km long-range Raman-based distributed temperature sensor with meter-scale spatial resolution,” in *Conference on Optical Fiber Communication*, Mar. 2010, pp. 1–3.
- [112] M. A. Soto, T. Nannipieri, A. Signorini, G. Bolognini, F. Di Pasquale, A. Lazzeri, F. Baronti, and R. Roncella, “Advanced cyclic coding technique for long-range Raman DTS systems with meter-scale spatial resolution over standard SMF,” in *Sensors, IEEE*, Oct. 2011, pp. 878–881.
- [113] Y. Liu, L. Ma, C. Yang, W. Tong, and Z. He, “Long-range Raman distributed temperature sensor with high spatial and temperature resolution using graded-index few-mode fiber,” *Optics Express*, vol. 26, no. 16, pp. 20 562–20 571, Aug. 2018.
- [114] G. Dai, X. Fan, and Z. He, “A Long-range Fiber-optic Raman Distributed Temperature Sensor Based on Dual-source Scheme and RZ Simplex Coding,” in *Asia Communications and Photonics Conference*, Oct. 2018, pp. 1–3.
- [115] B. Yan, J. Li, M. Zhang, Y. Xu, T. Yu, J. Zhang, L. Qiao, and T. Wang, “Temperature accuracy and resolution improvement for a Raman distributed fiber-optics sensor by using the Rayleigh noise suppression method,” *Applied Optics*, vol. 59, no. 1, pp. 22–27, Jan. 2020.
- [116] M. Asobe, T. Kanamori, K. Naganuma, H. Itoh, and T. Kaino, “Third-order nonlinear spectroscopy in As₂S₃ chalcogenide glass fibers,” *Journal of applied physics*, vol. 77, no. 11, pp. 5518–5523, Feb. 1995.
- [117] F. Kulwa, C. Li, X. Zhao, B. Cai, N. Xu, S. Qi, S. Chen, and Y. Teng, “A State-of-the-Art Survey for Microorganism Image Segmentation Methods and Future Potential,” *IEEE Access*, vol. 7, pp. 100 243–100 269, Jul. 2019.
- [118] J. A. Noble and D. Boukerroui, “Ultrasound image segmentation: A survey,” *IEEE Transactions on Medical Imaging*, vol. 25, no. 8, pp. 987–1010, Aug. 2006.
- [119] F. Xing and L. Yang, “Robust Nucleus/Cell Detection and Segmentation in Digital Pathology and Microscopy Images: A Comprehensive Review,” *IEEE Reviews in Biomedical Engineering*, vol. 9, pp. 234–263, Jan. 2016.

- [120] M. Q. Li, L. P. Xu, S. Gao, N. Xu, and B. Yan, "Remote sensing image segmentation based on a robust fuzzy C-means algorithm improved by a parallel Lévy grey wolf algorithm," *Applied Optics*, vol. 58, no. 17, pp. 4812–4822, Jun. 2019.
- [121] C. Kharmyssov, M. W. L. Ko, and J. R. Kim, "Automated segmentation of optical coherence tomography images," *Chinese Optics Letters*, vol. 17, no. 1, pp. 1–6, Jan. 2019.
- [122] M. Sezgin and B. Sankur, "Survey over image thresholding techniques and quantitative performance evaluation," *Journal of Electronic Imaging*, vol. 13, no. 1, pp. 146–165, Jan. 2004.
- [123] D. Shao, C. Xu, Y. Xiang, P. Gui, X. Zhu, C. Zhang, and Z. Yu, "Ultrasound image segmentation with multilevel threshold based on differential search algorithm," *IET Image Processing*, vol. 13, no. 6, pp. 998–1005, May 2019.
- [124] L. W. Mdakane and W. Kleynhans, "An Image-Segmentation-Based Framework to Detect Oil Slicks From Moving Vessels in the Southern African Oceans Using SAR Imagery," *IEEE Journal of Selected Topics in Applied Earth Observations and Remote Sensing*, vol. 10, no. 6, pp. 2810–2818, Jun. 2017.
- [125] M. A. Simão, P. Neto, and O. Gibaru, "Unsupervised Gesture Segmentation by Motion Detection of a Real-Time Data Stream," *IEEE Transactions on Industrial Informatics*, vol. 13, no. 2, pp. 473–481, Apr. 2017.
- [126] A. Bosco, A. Bruna, G. Messina, and G. Spampinato, "Fast method for noise level estimation and integrated noise reduction," *IEEE transactions on Consumer Electronics*, vol. 51, no. 3, pp. 1028–1033, Sep. 2005.
- [127] W. Liu and W. Lin, "Additive white Gaussian noise level estimation in SVD domain for images," *IEEE Transactions on Image processing*, vol. 22, no. 3, pp. 872–883, Sep. 2012.
- [128] P. Jiang, Q. Wang, and J. Wu, "Efficient noise-level estimation based on principal image texture," *IEEE Transactions on Circuits and Systems for Video Technology*, vol. 30, no. 7, pp. 1987–1999, Apr. 2019.
- [129] Z. Zhang and J. Yin, "Bee Foraging Algorithm Based Multi-Level Thresholding For Image Segmentation," *IEEE Access*, vol. 8, pp. 16 269–16 280, Jan. 2020.

- [130] Z. Ding, C. Wang, K. Liu, J. Jiang, D. Yang, G. Pan, Z. Pu, and T. Liu, "Distributed optical fiber sensors based on optical frequency domain reflectometry: A review," *Sensors*, vol. 18, no. 4, pp. 1–31, Apr. 2018.
- [131] A. Ukil, H. Braendle, and P. Krippner, "Distributed Temperature Sensing: Review of Technology and Applications," *IEEE Sensors Journal*, vol. 12, no. 5, pp. 885–892, May 2012.
- [132] R. Feced, M. Farhadiroushan, V. Handerek, and A. Rogers, "Advances in high resolution distributed temperature sensing using the time-correlated single photon counting technique," *IEE Proceedings-Optoelectronics*, vol. 144, no. 3, pp. 183–188, Jun. 1997.
- [133] J. King, D. Smith, K. Richards, P. Timson, R. Epworth, and S. Wright, "Development of a coherent OTDR instrument," *Journal of Lightwave Technology*, vol. 5, no. 4, pp. 616–624, Apr. 1987.
- [134] R. I. MacDonald, "Frequency domain optical reflectometer," *Applied Optics*, vol. 20, no. 10, pp. 1840–1844, May 1981.
- [135] J. Jiang, J. Sheng, Q. Wu, Z. Li, L. Zhong, M. Song, Z. Hong, and Z. Jin, "Spatial and temporal resolution optimization on Raman distributed temperature sensor system for quench detection in a no-insulated coil," *IEEE Transactions on Applied Superconductivity*, vol. 29, no. 5, pp. 1–5, Aug. 2019.
- [136] X. Sun, Z. Yang, X. Hong, S. Zaslawski, S. Wang, M. A. Soto, X. Gao, J. Wu, and L. Thévenaz, "Genetic-optimised aperiodic code for distributed optical fibre sensors," *Nature Communications*, vol. 11, no. 1, pp. 1–11, Nov. 2020.
- [137] Z. Zhang, H. Wu, C. Zhao, and M. Tang, "High-Performance Raman Distributed Temperature Sensing Powered by Deep Learning," *Journal of Lightwave Technology*, vol. 39, no. 2, pp. 654–659, Jan. 2021.
- [138] L. C. B. Silva, P. M. Ciarelli, J. C. C. Silva, I. B. V. Costa, M. E. V. Segatto, M. J. Pontes, and C. E. S. Castellani, "Detection of Multiple Small Temperature Events Simultaneously on a Distributed Temperature Map," *IEEE Sensors Journal*, vol. 21, no. 4, pp. 4582–4589, Feb. 2021.
- [139] R. K. Willardson and A. C. Beer, *Semiconductors and semimetals*. Academic press, 1977, pp. 291–393.

- [140] T. Nakata, I. Watanabe, K. Makita, and T. Torikai, "InAlAs avalanche photodiodes with very thin multiplication layer of 0.1 μm for high-speed and low - voltage - operation optical receiver," *Electronics Letters*, vol. 36, no. 21, pp. 1807–1809, Sep. 2000.
- [141] I. Watanabe, T. Nakata, M. Tsuji, K. Makita, T. Torikai, and K. Taguchi, "High-speed, high-reliability planar-structure superlattice avalanche photodiodes for 10-Gb/s optical receivers," *Journal of Lightwave Technology*, vol. 18, no. 12, pp. 2200–2207, Dec. 2000.
- [142] C. Lenox, H. Nie, P. Yuan, G. Kinsey, A. Homles, B. Streetman, and J. Campbell, "Resonant-cavity InGaAs-InAlAs avalanche photodiodes with gain - bandwidth product of 290 GHz," *IEEE Photonics Technology Letters*, vol. 11, no. 9, pp. 1162–1164, Sep. 1999.
- [143] T. Nakata, T. Takeuchi, I. Watanabe, K. Makita, and T. Torikai, "10 Gbit/s high sensitivity, low-voltage-operation avalanche photodiodes with thin In-AlAs multiplication layer and waveguide structure," *Electronics Letters*, vol. 36, no. 24, pp. 2033–2034, Oct. 2000.
- [144] M. Mathew, B. Hart, and K. Hayatleh, "Design of a low-current shunt-feedback transimpedance amplifier with inherent loop-stability," *Analog Integrated Circuits and Signal Processing*, vol. 99, no. 3, pp. 539–545, Oct. 2019.
- [145] J.-h. Noh, "A Capacitive Feedback Transimpedance Amplifier with a DC Feedback Loop Using a Transistor for High DC Dynamic Range," *Sensors*, vol. 20, no. 17, pp. 1–11, Aug. 2020.
- [146] M. A. Farahani and T. Gogolla, "Spontaneous Raman Scattering in Optical Fibers with Modulated Probe Light for Distributed Temperature Raman Remote Sensing," *Journal of Lightwave Technology*, vol. 17, no. 8, pp. 1379–1391, Aug. 1999.
- [147] H. S. Pradhan and P. K. Sahu, "Characterisation of Raman distributed temperature sensor using deconvolution algorithms," *IET Optoelectronics*, vol. 9, no. 2, pp. 101–107, Apr. 2015.
- [148] R. Green, M. Higgins, H. Joshi, and M. Leeson, "Bandwidth extension for optical wireless receiver-amplifiers," in *10th Anniversary International Conference on Transparent Optical Networks*, vol. 4, IEEE, Aug. 2008, pp. 201–204.

- [149] M. Abdullah and R. Green, "Receiver Front-End Bandwidth Enhancement Design," *Journal of Telecommunication, Electronic and Computer Engineering*, vol. 3, no. 1, pp. 69–78, Jun. 2011.
- [150] B. Zhang, C. Malouin, and T. J. Schmidt, "Towards full band colorless reception with coherent balanced receivers," *Optics Express*, vol. 20, no. 9, pp. 10 339–10 352, Apr. 2012.
- [151] N. Daghestani, K. Parow-Souchon, D. Pardo, H. Liu, N. Brewster, M. Frogley, G. Cinque, B. Alderman, and P. G. Huggard, "Room temperature ultrafast InGaAs Schottky diode based detectors for terahertz spectroscopy," *Infrared Physics & Technology*, vol. 99, pp. 240–247, Jun. 2019.
- [152] H. Zumbahlen *et al.*, *Linear circuit design handbook*. Newnes, 2011.
- [153] R. Mancini, *Op amps for everyone: design reference*. Newnes, 2003.
- [154] N. S. Fabián, A. B. Socorro-Leránóz, I. D. Villar, S. Díaz, and I. R. Matías, "Multimode-Coreless-Multimode Fiber-Based Sensors: Theoretical and Experimental Study," *Journal of Lightwave Technology*, vol. 37, no. 15, pp. 3844–3850, Aug. 2019.
- [155] J. Amorebieta, G. Durana, A. Ortega-Gomez, R. Fernández, J. Velasco, I. S. de Ocáriz, J. Zubia, J. E. Antonio-López, A. Schülzgen, R. Amezcua-Correa, and J. Villatoro, "Packaged Multi-Core Fiber Interferometer for High-Temperature Sensing," *Journal of Lightwave Technology*, vol. 37, no. 10, pp. 2328–2334, May 2019.
- [156] Y. Liu, B. Qi, and D. E. Winder, "All-Fiber Phase-Shifted Demodulation System for Fabry-Perot Interferometric Sensors," in *Conference on Lasers and Electro-Optics*, Optical Society of America, 2019.
- [157] C. Han, C. Zhao, H. Ding, and C. Chen, "Spherical microcavity-based membrane - free Fizeau interferometric acoustic sensor," *Optics Letters*, vol. 44, no. 15, pp. 3677–3680, Aug. 2019.
- [158] K. Chen, M. Guo, S. Liu, B. Zhang, H. Deng, Y. Zheng, Y. Chen, C. Luo, L. Tao, M. Lou, and Q. Yu, "Fiber-optic photoacoustic sensor for remote monitoring of gas micro-leakage," *Optics Express*, vol. 27, no. 4, pp. 4648–4659, Feb. 2019.

- [159] R. Kanawade, A. Kumar, D. Pawar, K. Vairagi, D. Late, S. Sarkar, R. K. Sinha, and S. Mondal, “Negative axicon tip-based fiber optic interferometer cavity sensor for volatile gas sensing,” *Optics Express*, vol. 27, no. 5, pp. 7277–7290, Mar. 2019.
- [160] S. Kim, Y.-P. Hong, and D.-J. Lee, “Polarization insensitive electro-optic probe using birefringence-free interferometric modulation,” *Optics Letters*, vol. 44, no. 11, pp. 2895–2898, Jun. 2019.
- [161] P. Li, Y. Li, F. Chen, C. Peng, and Z. Li, “Two-Port Noise Suppression in Dual-Polarization Interferometric Fiber-Optic Gyroscope,” *IEEE Photonics Journal*, vol. 11, no. 2, pp. 1–9, Apr. 2019.
- [162] E. Maciak, “Low-Coherence Interferometric Fiber Optic Sensor for Humidity Monitoring Based on Nafion Thin Film,” *Sensors*, vol. 19, no. 3, pp. 1–20, Feb. 2019.
- [163] R. Ravikumar, L. H. Chen, M. M. Xin Hui, and C. C. Chan, “Ion-Imprinted Chitosan-Based Interferometric Sensor for Selective Detection of Heavy Metal Ions,” *Journal of Lightwave Technology*, vol. 37, no. 11, pp. 2778–2783, Jun. 2019.
- [164] S. Ghildiyal, P. Ranjan, S. Mishra, R. Balasubramaniam, and J. John, “Fabry – Perot Interferometer-Based Absolute Pressure Sensor With Stainless Steel Diaphragm,” *IEEE Sensors Journal*, vol. 19, no. 15, pp. 6093–6101, Aug. 2019.
- [165] W. Wu, Y. Cao, H. Zhang, B. Liu, X. Zhang, S. Duan, and Y. Liu, “Compact Magnetic Field Sensor Based on a Magnetic-Fluid-Integrated Fiber Interferometer,” *IEEE Magnetism Letters*, vol. 10, no. 8103605, pp. 1–5, May 2019.
- [166] S. Wang, L. Li, J. Wang, Z. Yan, D. Liu, and Q. Sun, “Smart Mattress System Based on Interferometric Fiber Optics for Vital Signs Monitoring,” in *Conference on Lasers and Electro-Optics (CLEO)*, May 2019, pp. 1–2.
- [167] T. Liu, H. Zhang, L. Xue, B. Liu, H. Liu, B. Huang, J. Sun, and D. Wang, “Highly Sensitive Torsion Sensor Based on Side-Hole-Fiber Sagnac Interferometer,” *IEEE Sensors Journal*, vol. 19, no. 17, pp. 7378–7382, Sep. 2019.

- [168] Y. Yang, Z. Wang, T. Chang, L. Cheng, M. Yu, and H. Cui, "Performance Optimization of Fiber Optic Interferometric Accelerometer Based on Phase Noise Analysis," *IEEE Sensors Journal*, vol. 19, no. 22, pp. 10 498–10 505, Nov. 2019.
- [169] L. Xie, L. V. Nguyen, H. Ebendorff-Heidepriem, and S. C. Warren-Smith, "Multiplexed Optical Fiber Biochemical Sensing Using Cascaded C-shaped Fabry-Perot Interferometers," *IEEE Sensors Journal*, vol. 19, no. 22, pp. 10 425–10 431, Nov. 2019.
- [170] C. E. S. Castellani, H. C. B. Ximenes, R. L. Silva, A. Frizera-Neto, M. R. N. Ribeiro, and M. J. Pontes, "Multi-Parameter Interferometric Sensor Based on a Reduced Diameter Core Axial Offseted Fiber," *IEEE Photonics Technology Letters*, vol. 29, no. 2, pp. 239–242, Jan. 2017.
- [171] C. A. Rodríguez, M. R. N. Ribeiro, A. Frizera-Neto, C. E. S. Castellani, and M. J. Pontes, "Envelope-based technique for liquid level sensors using an in-line fiber Mach-Zehnder interferometer," *Applied Optics*, vol. 55, no. 34, pp. 9803–9809, Dec. 2016.
- [172] X. Wen, T. Ning, C. Li, Z. Kang, J. Li, H. You, T. Feng, J. Zheng, and W. Jian, "Liquid level measurement by applying the Mach-Zehnder interferometer based on up-tapers," *Applied Optics*, vol. 53, no. 1, pp. 71–75, Jan. 2014.
- [173] P. Jiang, L. Ma, Z. Hu, and Y. Hu, "Low-Crosstalk and Polarization - Independent In-line Interferometric Fiber Sensor Array Based on Fiber Bragg Gratings," *Journal of Lightwave Technology*, vol. 34, no. 18, pp. 4232–4239, Sep. 2016.
- [174] C. Zhou, Y. Pang, L. Qian, X. Chen, Q. Xu, C. Zhao, H. Zhang, Z. Tu, J. Huang, H. Gu, and D. Fan, "Demodulation of a Hydroacoustic Sensor Array of Fiber Interferometers Based on Ultra-Weak Fiber Bragg Grating Reflectors Using a Self-Referencing Signal," *Journal of Lightwave Technology*, vol. 37, no. 11, pp. 2568–2576, Jun. 2019.
- [175] J. Liu, D. N. Wang, and L. Zhang, "Slightly Tapered Optical Fiber With Dual Inner Air-Cavities for Simultaneous Refractive Index and Temperature Measurement," *Journal of Lightwave Technology*, vol. 34, no. 21, pp. 4872–4876, Nov. 2016.

-
- [176] Y. Ouyang, H. Guo, X. Ouyang, Y. Zhao, Z. Zheng, C. Zhou, and A. Zhou, "An In-Fiber Dual Air-Cavity Fabry – Perot Interferometer for Simultaneous Measurement of Strain and Directional Bend," *IEEE Sensors Journal*, vol. 17, no. 11, pp. 3362–3366, Jun. 2017.
- [177] Q. Rong, X. Qiao, Y. Du, H. Sun, D. Feng, R. Wang, M. Hu, and Z. Feng, "In-fiber quasi-Michelson interferometer for liquid level measurement with a core-cladding-modes fiber end-face mirror," *Optics and Lasers in Engineering*, vol. 57, pp. 53–57, Jun. 2014.
- [178] C. A. Rodríguez, A. Leal-Junior, C. Marques, A. Frizera, M. J. Pontes, P. F. Antunes, P. S. André, and M. R. Ribeiro, "Optical fiber sensing for sub-millimeter liquid-level monitoring: A review," *IEEE Sensors Journal*, vol. 19, no. 17, pp. 7179–7191, Sep. 2019.
- [179] H. Fu, X. Shu, A. Zhang, W. Liu, L. Zhang, S. He, and I. Bennion, "Implementation and Characterization of Liquid-Level Sensor Based on a Long-Period Fiber Grating Mach–Zehnder Interferometer," *IEEE Sensors Journal*, vol. 11, no. 11, pp. 2878–2882, Nov. 2011.
- [180] J. Hsu, C. Lee, H. Chang, W. C. Shih, and C. Li, "Highly Sensitive Tapered Fiber Mach–Zehnder Interferometer for Liquid Level Sensing," *IEEE Photonics Technology Letters*, vol. 25, no. 14, pp. 1354–1357, Jul. 2013.
- [181] A. Wang, H. Xiao, J. Wang, Z. Wang, W. Zhao, and R. G. May, "Self-calibrated interferometric-intensity-based optical fiber sensors," *Journal of Lightwave Technology*, vol. 19, no. 10, pp. 1495–1501, Oct. 2001.
- [182] S.-C. Huang and H. Lin, "Counting signal processing and counting level normalization techniques of polarization-insensitive fiber-optic Michelson interferometric sensors," *Applied Optics*, vol. 45, no. 35, pp. 8832–8838, Dec. 2006.
- [183] F. Liu, S. Xie, L. Gu, X. He, D. Yi, Z. Chen, M. Zhang, and Q. Tao, "Common-Mode Noise Suppression Technique in Interferometric Fiber-Optic Sensors," *Journal of Lightwave Technology*, vol. 37, no. 21, pp. 5619–5627, Nov. 2019.
- [184] N. Song, Z. Yuan, and X. Pan, "Adaptive Kalman filter based on random-weighting estimation for denoising the fiber-optic gyroscope drift signal," *Applied Optics*, vol. 58, no. 35, pp. 9505–9513, Dec. 2019.

- [185] C. Qi, M. Yang, D. Lee, W. Xie, and J. Dai, "Improved Sensitivity of Fiber Fabry-Perot Interferometer Based on Phase-Tracking Algorithm," *IEEE Sensors Journal*, vol. 15, no. 10, pp. 5834–5838, Oct. 2015.
- [186] B. Griffin and M. J. Connelly, "Digital signal processing of interferometric fiber optic sensors," in *Proceedings of the Lightwave Technologies in Instrumentation and Measurement Conference*, Oct. 2004, pp. 153–156.
- [187] B. H. Lee, Y. H. Kim, K. S. Park, J. B. Eom, M. J. Kim, B. S. Rho, and H. Y. Choi, "Interferometric fiber optic sensors," *Sensors*, vol. 12, no. 3, pp. 2467–2486, Jul. 2012.
- [188] A. Buades, B. Coll, and J. .-. Morel, "A non-local algorithm for image denoising," in *IEEE Computer Society Conference on Computer Vision and Pattern Recognition*, vol. 2, Jun. 2005, pp. 60–65.
- [189] J. Immerkær, "Fast Noise Variance Estimation," *Computer Vision and Image Understanding*, vol. 64, no. 2, pp. 300–302, Sep. 1996.
- [190] C. Cuartas-Vélez, R. Restrepo, B. E. Bouma, and N. Uribe-Patarroyo, "Volumetric non-local-means based speckle reduction for optical coherence tomography," *Biomedical Optics Express*, vol. 9, no. 7, pp. 3354–3372, Jul. 2018.
- [191] P. Meza, I. Ortiz, E. Vera, and J. Martinez, "Compressive hyperspectral imaging recovery by spatial-spectral non-local means regularization," *Optics Express*, vol. 26, no. 6, pp. 7043–7055, Mar. 2018.
- [192] A. Buades, B. Coll, and J.-M. Morel, "A review of image denoising algorithms, with a new one," *Multiscale Modeling & Simulation*, vol. 4, no. 2, pp. 490–530, 2005.
- [193] A. A. Efros and T. K. Leung, "Texture synthesis by non-parametric sampling," in *Proceedings of the seventh IEEE international conference on computer vision*, vol. 2, IEEE, Sep. 1999, pp. 1033–1038.
- [194] A. Buades, B. Coll, and J.-M. Morel, "Nonlocal Image and Movie Denoising," *International Journal of Computer Vision*, vol. 76, no. 2, pp. 123–139, Feb. 2008.

-
- [195] R. L. Silva, H. C. B. Ximenes, M. J. Pontes, and C. E. S. Castellani, "Fiber Optic Bend Sensor and a Novel Interrogation Technique Based on a Mach-Zehnder Interferometer," in *18th Brazilian Symposium on Microwave and Optoelectronics and 13th Brazilian Congress of Electromagnetism (MOMAG)*, Santa Rita do Sapucaí-MG/Brazil., Aug. 2018, pp. 1–4.
- [196] L. C. B. Silva, L. B. Scandian, M. E. V. Segatto, and C. E. S. Castellani, "Optical spectral intensity-based interrogation technique for liquid-level interferometric fiber sensors," *Applied Optics*, vol. 58, no. 35, pp. 9712–9717, Dec. 2019.
- [197] L. B. Scandian, M. E. Segatto, and C. E. Castellani, "Analytical Analysis and Experimental Validation of a Multi-parameter Mach-Zehnder Fiber Optic Interferometric Sensor," *Journal of Microwaves, Optoelectronics and Electromagnetic Applications*, vol. 17, no. 4, pp. 528–538, Dec. 2018.
- [198] B. Gu, W. Qi, Y. Zhou, Z. Wu, P. P. Shum, and F. Luan, "Reflective liquid level sensor based on modes conversion in thin-core fiber incorporating tilted fiber Bragg grating," *Optics Express*, vol. 22, no. 10, pp. 11 834–11 839, May 2014.